PNAS

Supporting Information for

Coupling During Collective Cell Migration is Controlled by a Vinculin Mechanochemical Switch.

T. Curtis Shoyer[1,*], Evan M. Gates[1,*], Jolene I. Cabe[2], Aarti N. Urs[3], Daniel E. Conway[4], Brenton D. Hoffman[1,3]

[1]Biomedical Engineering, Duke University, Durham NC, USA.
[2]Biomedical Engineering, Virginia Commonwealth University, Richmond, VA, USA.
[3]Cell Biology, Duke University, Durham, NC, USA.
[4]Biomedical Engineering, The Ohio State University, Columbus, OH, USA.
[*]These authors contributed equally.

Brenton D. Hoffman
Email: brenton.hoffman@duke.edu

This PDF file includes:

Figures S1 to S13
Legends for Movies S1 to S4
Supplementary Note 1, containing Figures S14 to S21 and Tables S1 to S3
Supplementary Note 2, containing Figures S22 to S24 and Tables S4 to S10
Extended Methods, containing Tables S11 and S12
SI References

Other supporting materials for this manuscript include the following:

Movies S1 to S4

Supplementary Figures S1 to S13

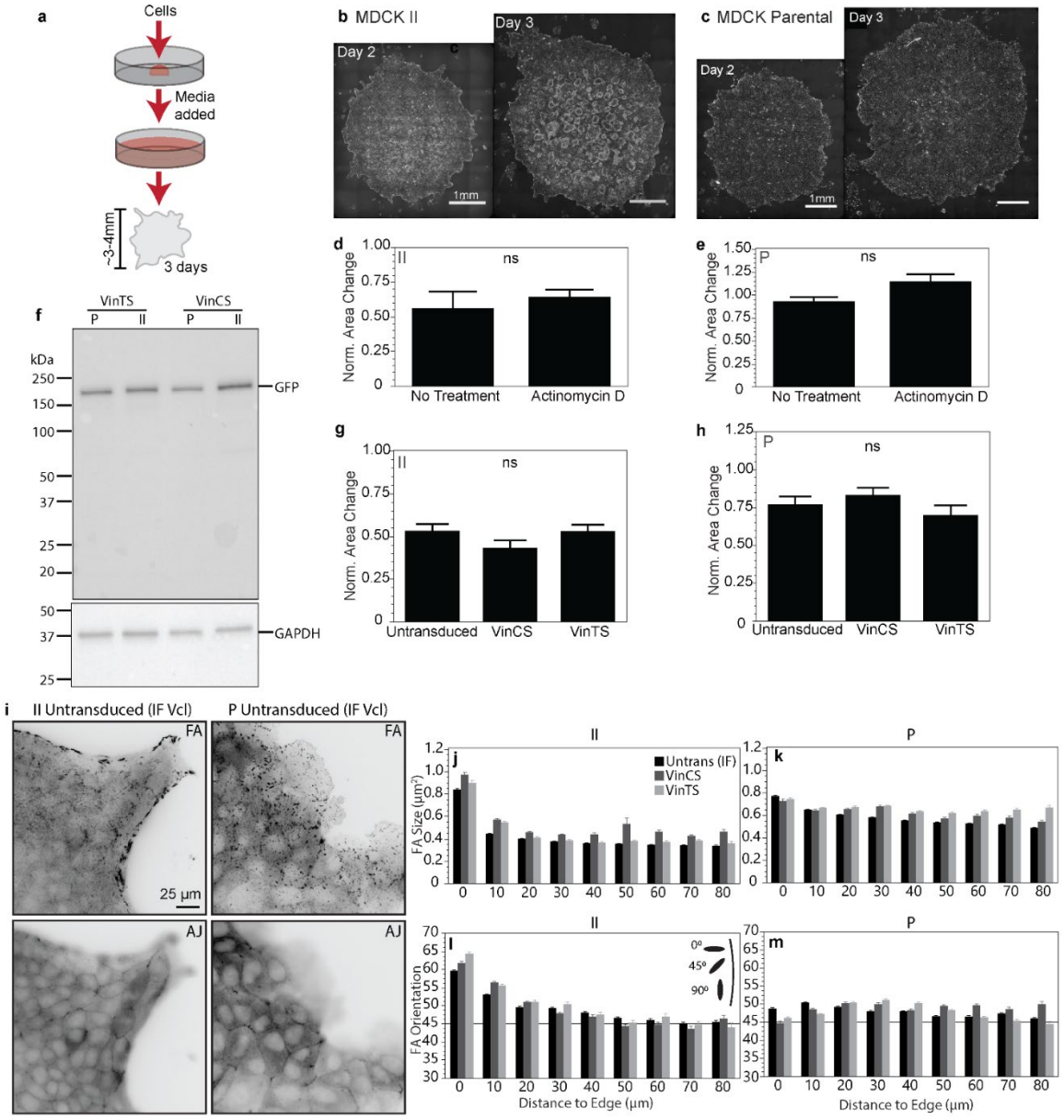

Fig. S1 Controls for droplet island assay and expression of VinTS and VinCS in MDCK cells. (a) Schematic depiction of droplet island assay. (b-c) Representative phase contrast images of migrating MDCK II or MDCK Parental islands at 2 and 3 days after droplet seeding. (d) Bar plot (mean +/- SEM) of normalized area change of droplet island assay between days 2 and 3 with or without treatment with Actinomycin D for MDCK II cells (n=3 or 4 islands, respectively, over at least 3 independent experiments). (e) Same for MDCK Parental cells (n=3 or 4 islands, respectively, over at least 3 independent experiments). (f) Western blot with GFP primary antibody showing that VinTS and VinCS are produced as stable proteins with the expected molecular weight when expressed in MDCK Parental and MDCK II cells. (g) Bar plot (mean +/- SEM) of normalized area change of droplet island assay between days 2 and 3 for MDCK II cells expressing no sensor (untransduced), VinCS, or VinTS (n=12, 4, or 7 islands, respectively, over at least 3 independent experiments). (h) Same for MDCK Parental cells (n=11, 5, or 4 islands, respectively, over at least 3 independent experiments). (i) Representative images of vinculin immunolabeling at the edge of (untransduced) migrating MDCK II or MDCK Parental monolayers

in the basal (FAs) or apical (AJs) plane. (j-m) Plots of FA size or FA orientation versus distance from edge for migrating MDCK II or MDCK Parental cells expressing no sensor (untransduced), VinCS, or VinTS. Differences between pairs in (d-e) were assessed using t-tests and differences between groups in (g-h) were assessed using ANOVAs (ns: not significant).

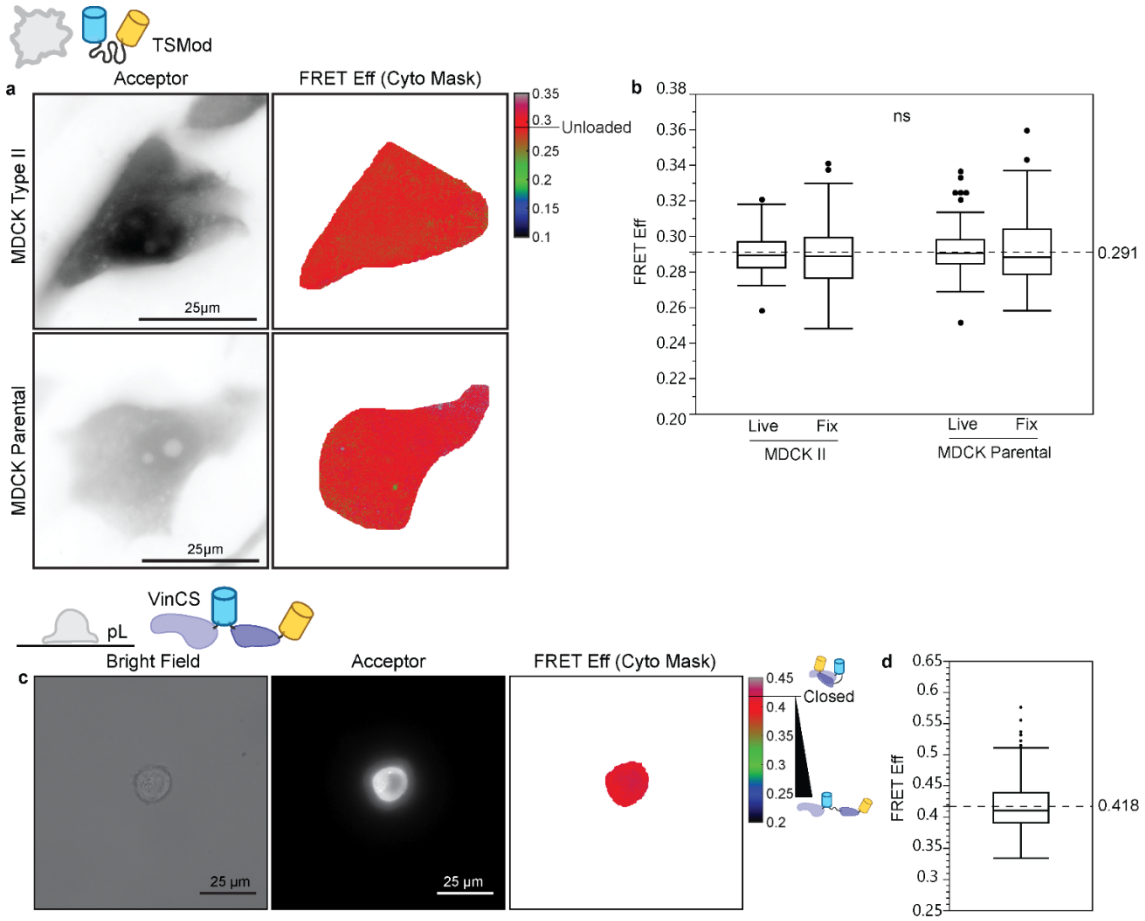

Fig. S2 Reference Conditions for VinTS (TSMod) and VinCS (pL). (a) Representative acceptor and cell-masked FRET efficiency images of migrating MDCK II and MDCK Parental cell monolayers expressing TSMod. (b) Box-whisker plot showing FRET efficiency for TSMod in MDCK II cells in live or fixed condition or MDCK Parental cells in live or fixed condition (n=117, 102, 119, and 120 cells, respectively, over 4 independent experiments). Differences between groups were tested for using Welch's ANOVA (ns: not significant). (c) Representative bright-field, acceptor, and cell-masked FRET efficiency images of a single MDCK Parental cell expressing VinCS adhered to poly-L-lysine (pL) surface in the live condition. (d) Box plot shows FRET efficiency for VinCS in single MDCK Parental cells adhered to pL surfaces in the live condition, with mean indicated by the dashed line (n=244 cells over 3 independent experiments). Comparisons to other experimental groups for VinCS are shown in Supplementary Note 2 Table S5.

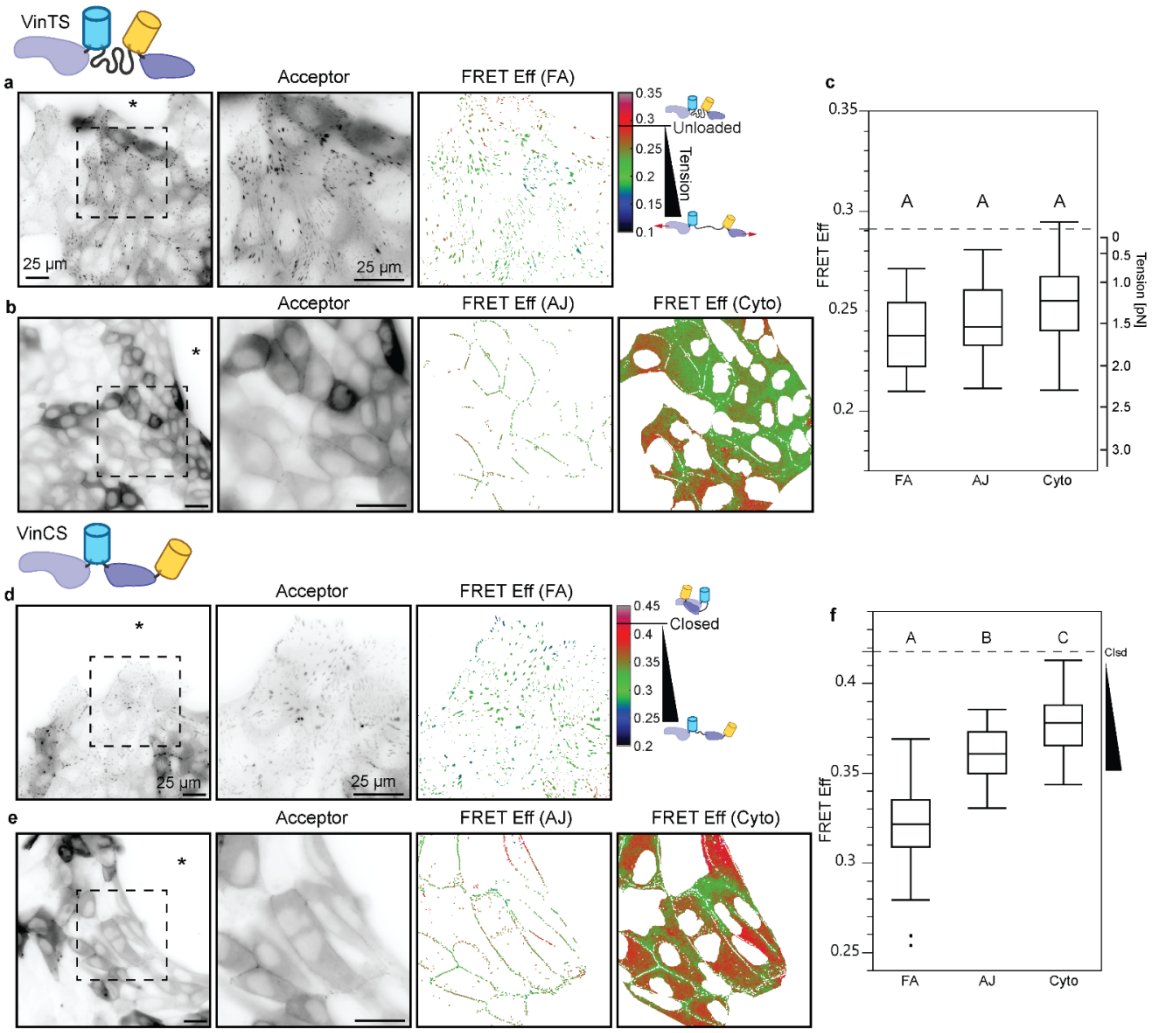

Fig. S3 VinTS and VinCS at the edge of collectively migrating MDCK Parental cells. Representative images of migrating MDCK Parental cell monolayers expressing VinTS (a,b) or VinCS (d,e) taken in the basal (a,d) or apical (b,e) plane at the monolayer edge with acceptor channel indicating sensor localization followed by zoom-ins of the indicated region for acceptor channel and FRET efficiency in the FA mask (a,d) or AJ and cytoplasm masks (b,e). Asterisk indicates free space adjacent to monolayer edge. Box plot of FRET efficiency for VinTS (c) at FAs, AJs, and cytoplasm (n=67, 48, and 48 images completed over at least 3 independent experiments) with unloaded reference level indicated (dotted line). Box plot of FRET efficiency for VinCS (f) at FAs, AJs, and cytoplasm (n=103, 51, and 53 images completed over at least 3 independent experiments) with closed reference level indicated (dotted line). Differences between groups were detected using the Steel-Dwass test. Levels not connected by the same letter are significantly different at $p<0.05$. Comparisons to other experimental groups are shown in Supplementary Note 2 Table S6 for VinTS and Supplementary Note 2 Table S5 for VinCS.

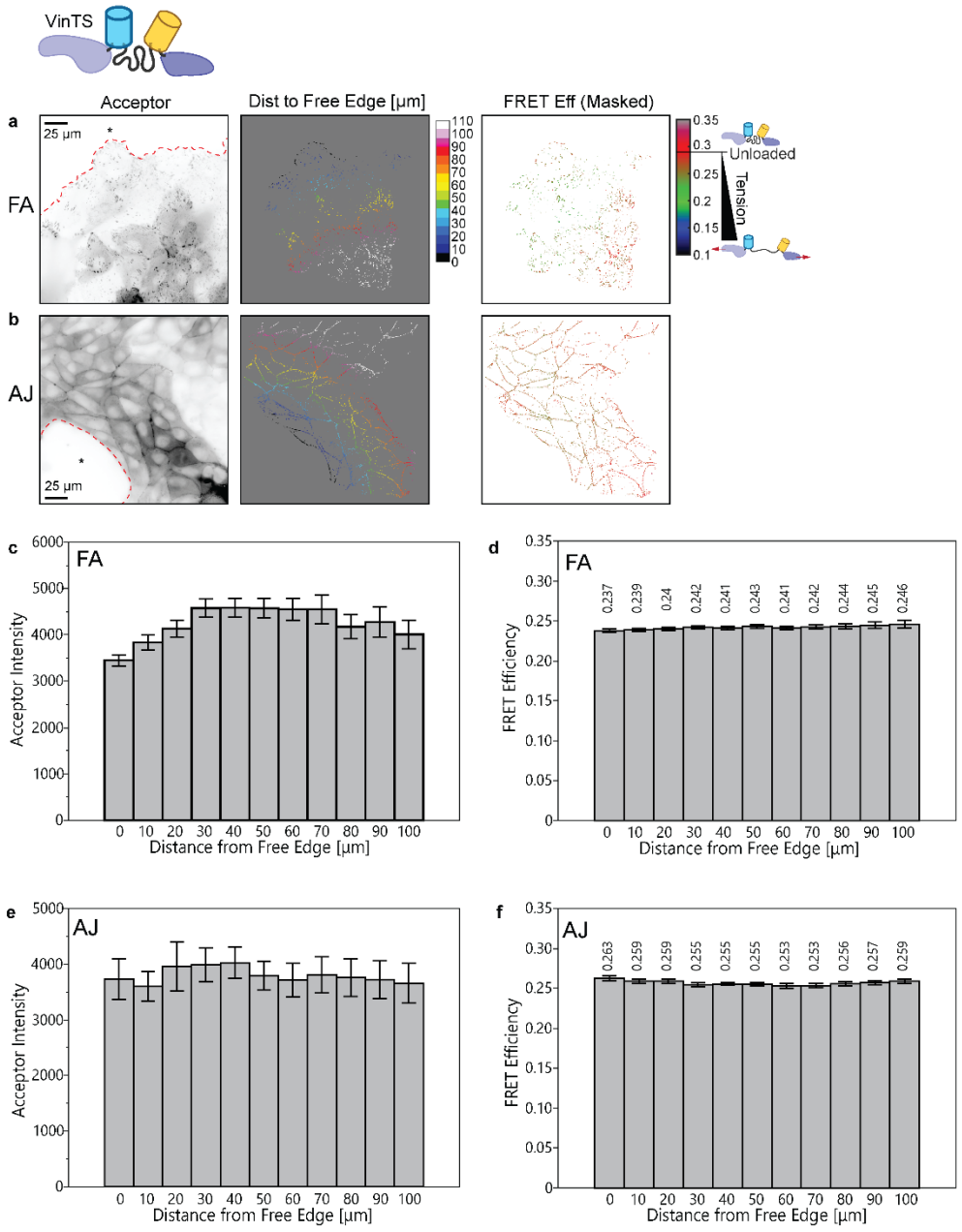

Fig. S4 Spatial profiles of VinTS FRET efficiency versus distance from free edge. Representative image of migrating MDCK Parental cell monolayers expressing VinTS taken in the basal (a) or apical (b) plane. Image of acceptor channel indicates sensor localization and the free edge (red line), followed by images showing the distance from the free edge (in um) and the FRET efficiency inside FA (a) or AJ (b) mask. Asterisk indicates free space adjacent to monolayer edge. Bar plots of acceptor intensity (c,e) and FRET efficiency (d,f) indicating mean +/- SEM binned by distance from free edge for FAs (c-d; n=28 images at 100 um) or AJs (e-f; n=23 images at 100 um). This supplemental figure is a re-analysis of the images of MDCK Parental VinTS that are part of the dataset analyzed in Figs 2 and S8.

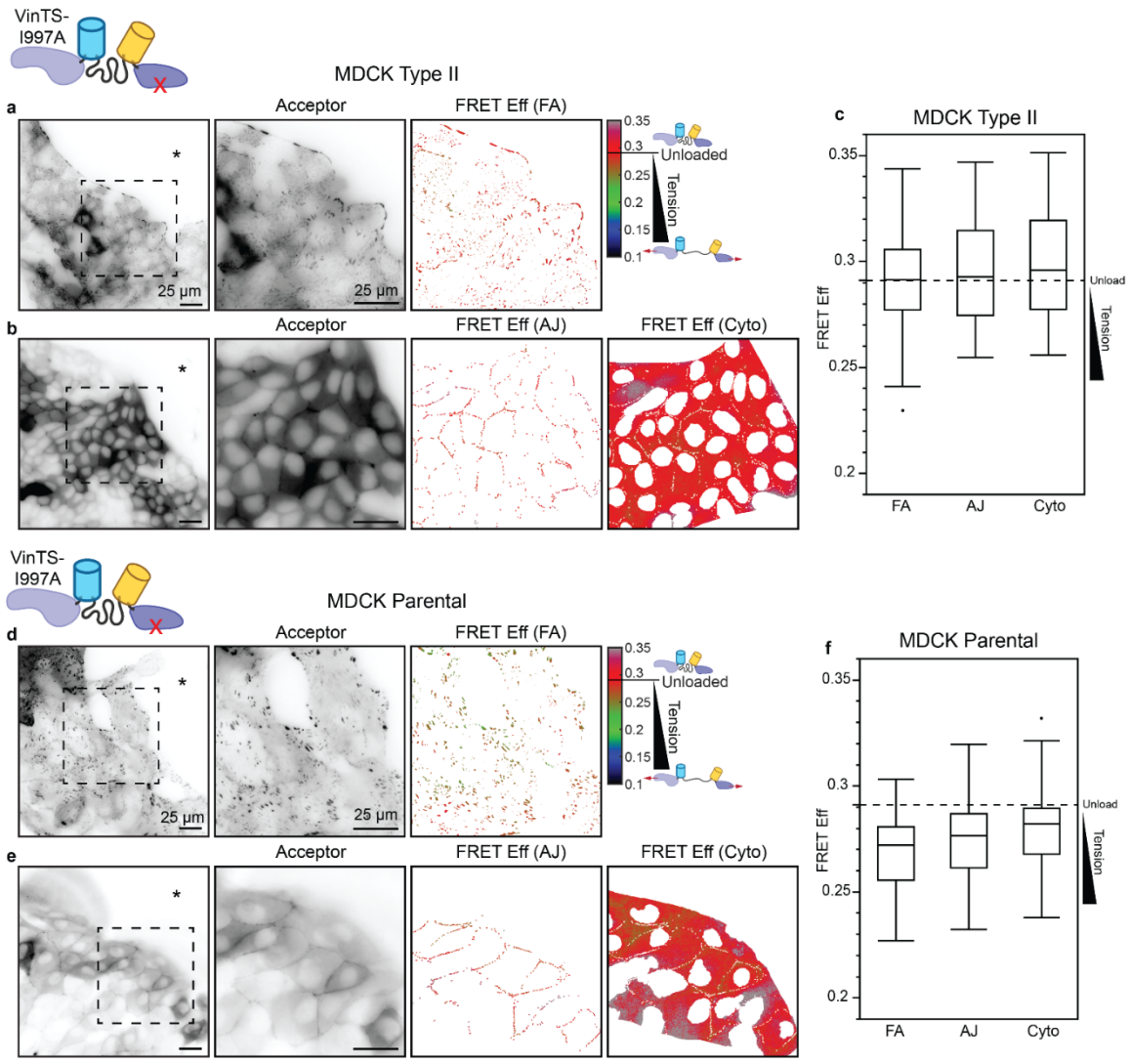

Fig. S5 VinTS-I997A at the edge of collectively migrating MDCK II and MDCK Parental cells. (a) Representative images of migrating MDCK II cell monolayers expressing VinTS-I997A taken in the basal plane with acceptor channel indicating sensor localization followed by zoom-in views of acceptor channel and FRET efficiency in the FA mask for the indicated region. (b) Representative images of VinTS-I997A in the apical plane with acceptor channel followed by zoom-in views of acceptor channel and FRET efficiency in AJ and cytoplasm masks for the indicated region. (c) Box-whisker plot showing FRET efficiency for VinTS-I997A at FAs, AJs, and cytoplasm (n=52, 31, and 31 images respectively over at least 3 independent experiments) with unloaded reference level indicated (dotted line). (d-f) Analogous representative images and plot for migrating MDCK Parental cell monolayers expressing VinTS-I997A (n=36, 24, and 25 images for FAs, AJs, and cytoplasm, respectively, over at least 3 independent experiments). Comparisons to other experimental groups are shown in Supplementary Note 2 Table S4 for MDCK II and Supplementary Note 2 Table S6 for MDCK Parental.

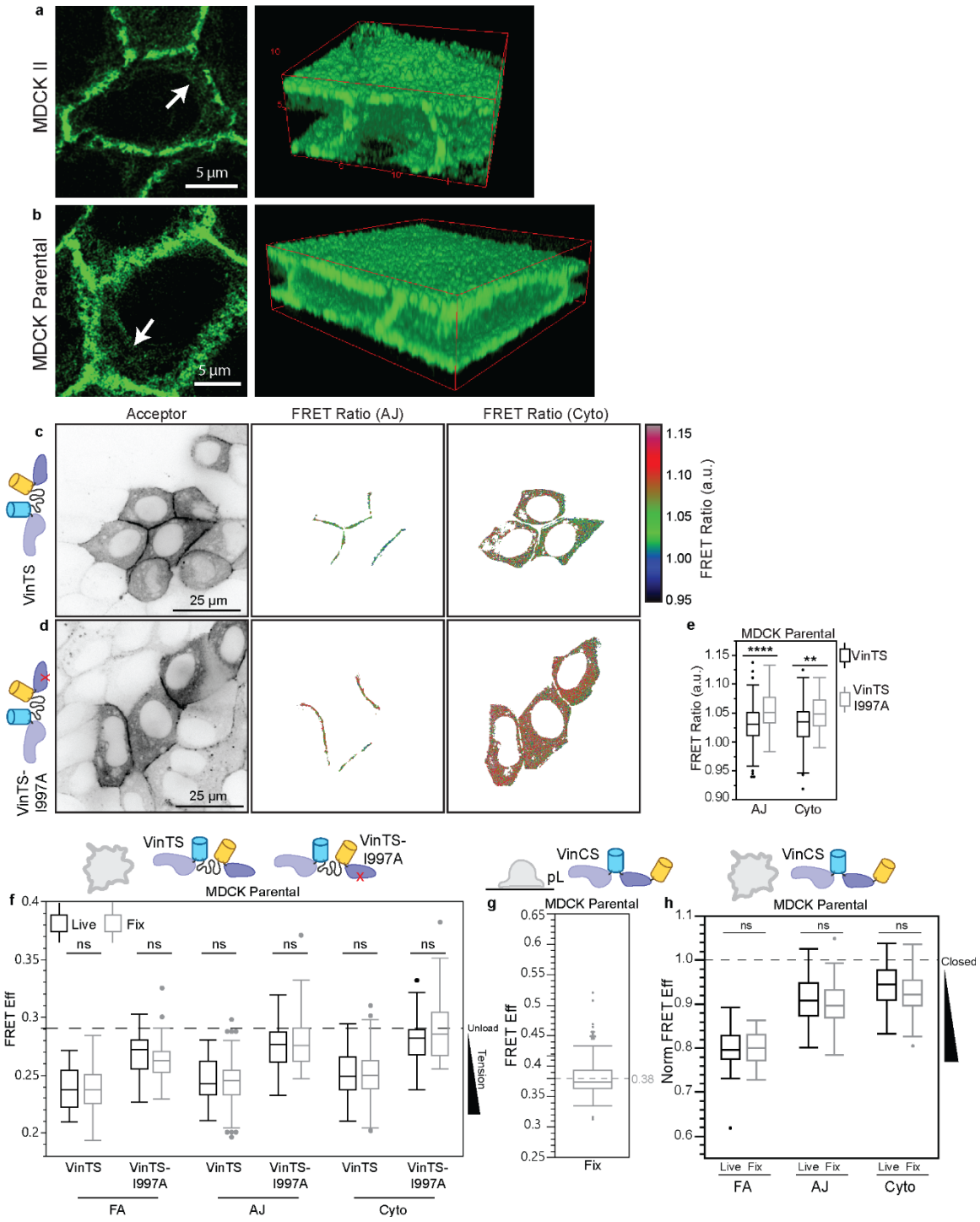

Fig. S6 Super-resolution imaging of actin, confocal imaging of VinTS, controls for the fixation of VinTS, and normalization of VinCS. (a-b) Stimulated emission depletion (STED) super-resolution imaging of phalloidin-labeled actin in collectively migrating MDCK II and MDCK Parental cells. White arrows indicate regions exhibiting a diffuse, cytoplasmic actin network. (c-d) Representative images for confocal imaging of migrating MDCK Parental cell monolayers expressing VinTS or VinTS-I997A taken in the apical plane at the monolayer edge with acceptor channel indicating sensor localization followed by FRET ratio in AJ and Cytoplasm masks. (e) Box plot showing FRET ratio in AJs and Cytoplasm for confocal imaging of VinTS and VinTS-

I997A in MDCK Parental cells (n = 207 and 160 junctions for VinTS and VinTS-I997A AJs, respectively, and 63 and 44 cells for VinTS and VinTS-I997A Cytoplasm, respectively, over 3 independent experiments). (f) Box plot showing FRET efficiency at the FAs, AJs, and cytoplasm for VinTS (n=152, 146, and 146 images respectively over at least 3 independent experiments) and VinTS-I997A (n=61, 76, and 76 images respectively over at least 3 independent experiments) at the edge of migrating MDCK Parental cell monolayers in the fixed condition with unloaded reference level indicated (dotted line). Data for the same constructs, structures, and cell type in the live condition repeated from Fig. S3 and Fig. S5 to show comparison. Differences between groups were detected using the Steel-Dwass test (ns: not significant). Comparisons to other experimental groups are shown in Supplementary Note 2 Table S6. (g) Box plot of FRET efficiency for single MDCK Parental cells expressing VinCS adhered to poly-L-lysine (pL) surface in the fixed condition, with mean indicated by the dashed line (n=164 cells over 3 independent experiments). (h) Box plot of normalized FRET efficiency for VinCS at the edge of MDCK Parental cell monolayers at the FAs, AJs, and cytoplasm in the live condition (n=40, 23, and 23 respectively over 2 independent experiments) with closed reference level indicated (dotted line). Data for VinCS in the same structures and cell type in the fixed condition repeated from Fig. 2 and Fig. S8 to show comparison. Differences between groups were detected using the Steel-Dwass test (ns: not significant). Comparisons to other experimental groups are shown in Supplementary Note 2 Table S8.

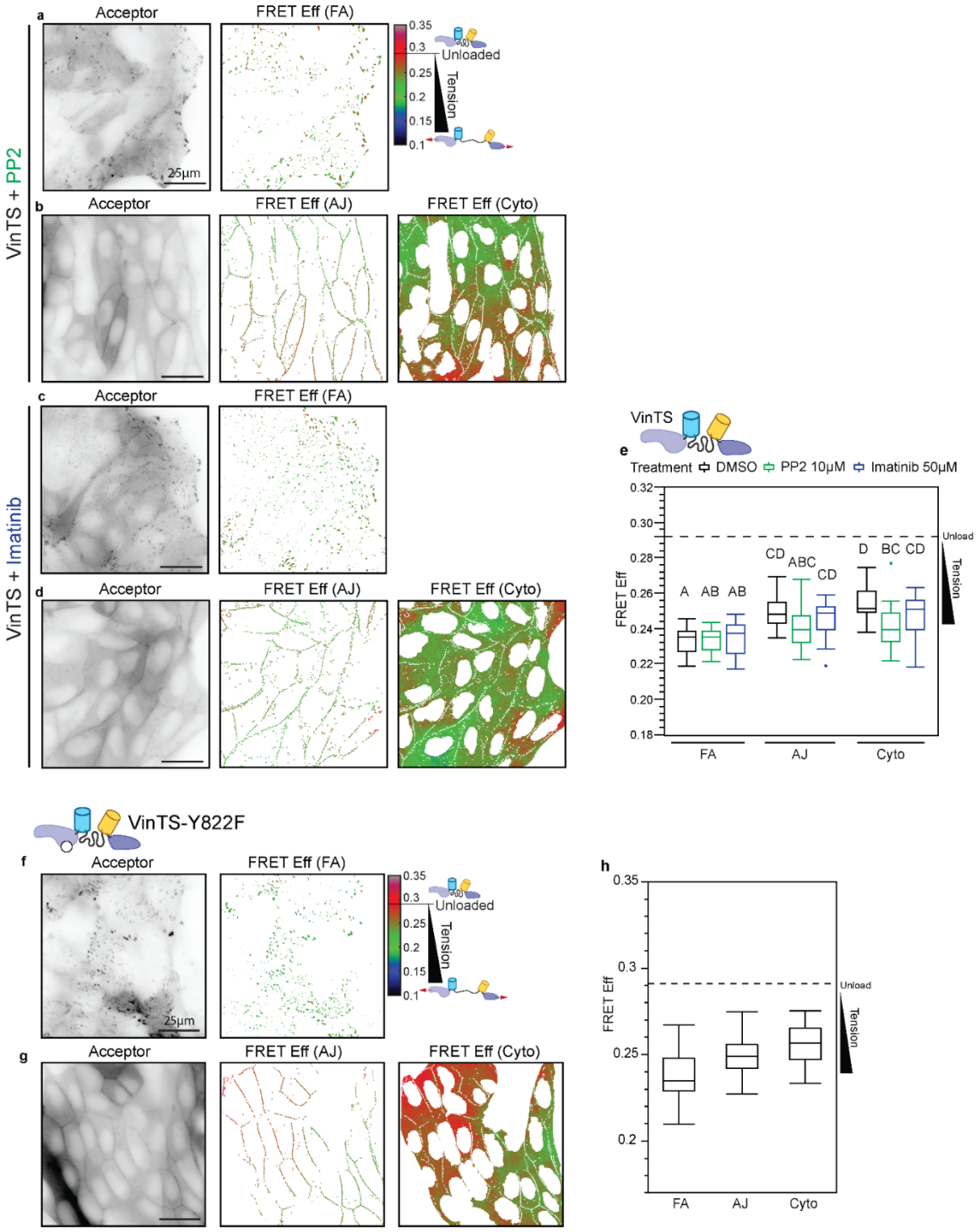

Fig. S7 Effect of inhibiting Src kinases (PP2) or inhibiting Abl kinase (Imatinib) or Y822F point mutation on vinculin loading at the edge of collectively migrating cells.
Representative images of PP2-treated MDCK Parental cells expressing VinTS taken in (a) the basal plane at the monolayer edge with acceptor channel and FRET efficiency in the FA mask or (b) in the apical plane at the monolayer edge with acceptor channel and FRET efficiency in AJ and cytoplasm masks. (c-d) Analogous representative images for Imatinib-treated MDCK Parental cells expressing VinTS. (e) Box-whisker plot showing FRET efficiency of VinTS at FAs,

AJs, and the cytoplasm of untreated (n=25, 23, and 23 images respectively over 2 independent experiments), PP2-treated (n=25, 21, and 21 images respectively over 2 independent experiments), and Imatinib-treated (n=23, 26, and 26 images respectively over 2 independent experiments) cells with unloaded reference level indicated (dotted line). Differences between groups were detected using the Tukey HSD test. Levels not connected by the same letter are significantly different at $p<0.05$. Representative images of MDCK Parental cells expressing VinTS-Y822F taken in (f) the basal plane at the monolayer edge with acceptor channel and FRET efficiency in the FA mask or (g) in the apical plane at the monolayer edge with acceptor channel and FRET efficiency in AJ and cytoplasm masks. (h) Box-whisker plot showing FRET efficiency of VinTS-Y822F at FAs, AJs, and the cytoplasm (n=44, 42, and 42 images respectively over at least 3 independent experiments) with unloaded reference level indicated (dotted line). Comparisons to other experimental groups are shown in Supplementary Note 2 Table S6.

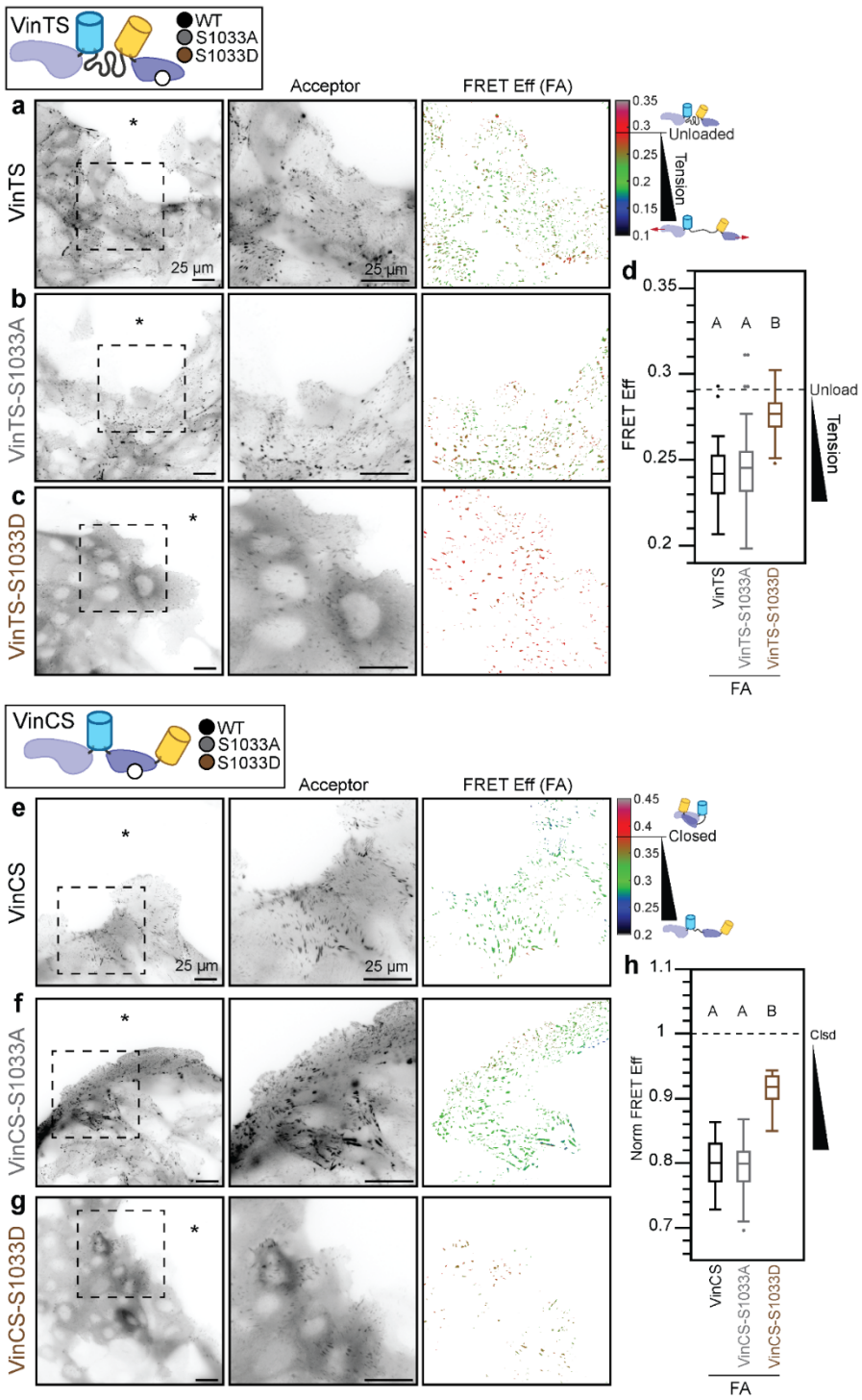

Fig. S8 Effect of vinculin S1033 mutants on vinculin load and conformation in FAs at the leading edge of collectively migrating cells. Representative images of migrating MDCK Parental cell monolayers expressing VinTS (a), VinTS-S1033A (b), VinTS-S1033D (c), VinCS (e), VinCS-S1033A (f), or VinCS-S1033D (g) taken in the basal plane at the monolayer edge with acceptor channel indicating sensor localization followed by zoom-ins of the indicated region for acceptor channel and FRET efficiency in FA masks. Asterisk indicates free space adjacent to monolayer edge. (d) Box-whisker plot showing FRET efficiency for VinTS, VinTS-S1033A, and VinTS-S1033D in FAs (n=85, 55, and 49 images respectively over at least 3 independent

experiments) with unloaded reference level indicated (dotted line). (h) Box-whisker plot showing FRET efficiency for VinCS, VinCS-S1033A, and VinCS-S1033D in FAs (n=67, 35, and 30 images respectively over at least 3 independent experiments) with closed reference level indicated (dotted line). Differences between groups were detected using the Steel-Dwass test. Levels not connected by the same letter are significantly different at $p<0.05$. Comparisons to other experimental groups are shown in Supplementary Note 2 Tables S7-8.

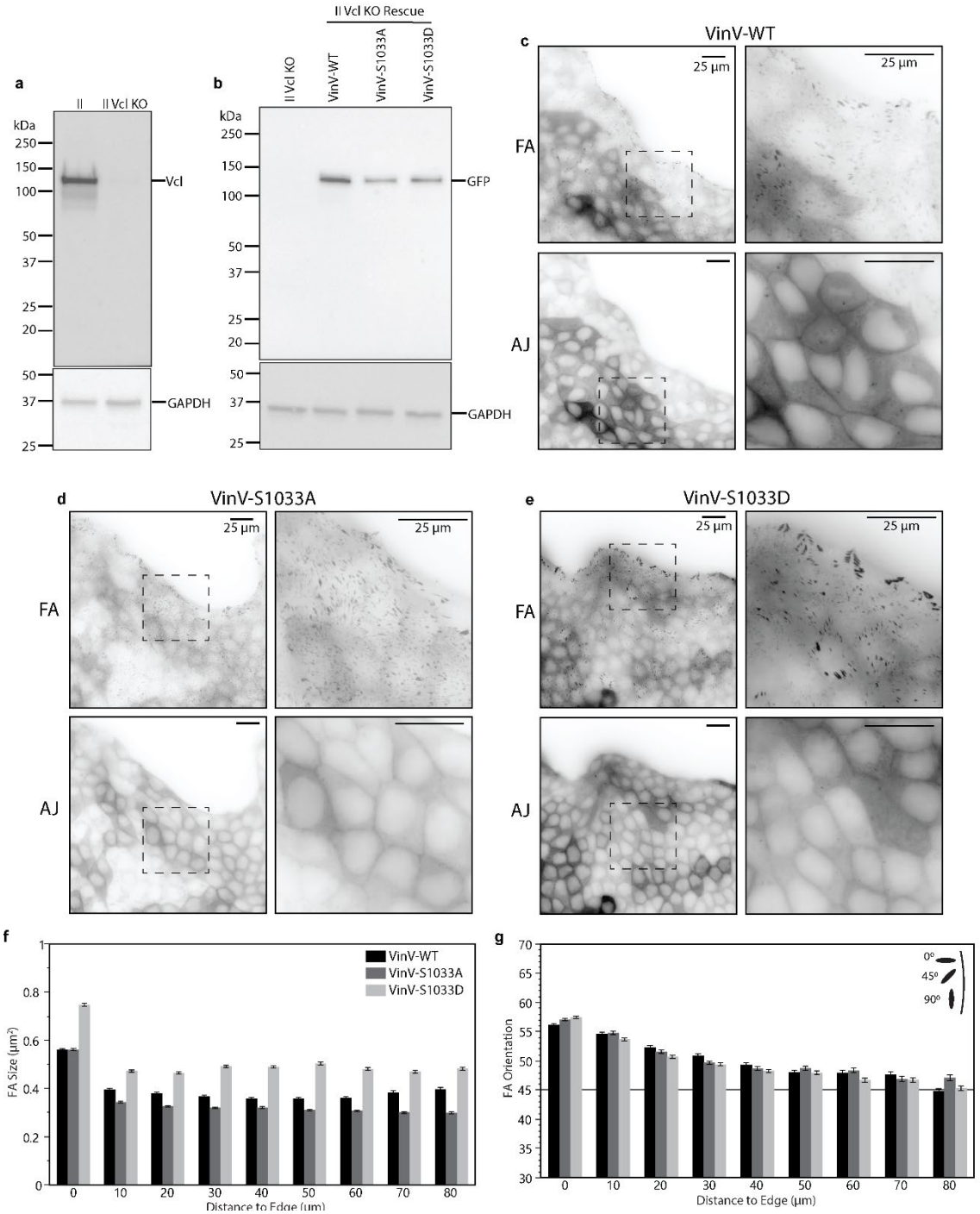

Fig. S9 Rescue of MDCK II Vcl KO cells with Vinculin-mVenus and S1033 mutants. (a) Western blot with vinculin antibody confirming CRISPR/Cas9-mediated knockout of vinculin in MDCK II cells. (b) Western blot with GFP primary antibody showing production of stable proteins with the expected molecular weight for rescue of MDCK II Vcl KO cells with Vinculin-mVenus (VinV-WT), Vinculin-mVenus-S1033A (VinV-S1033A), or Vinculin-mVenus-S1033D (VinV-S1033D). (c-e) Representative images of MDCK II Vcl KO cells rescued with VinV, VinV-S1033A, or VinV-S1033D at the edge of migrating monolayers in the basal (FAs) and apical (AJs) plane,

with zoom-in views (at right). (f-g) Plots of FA size and FA orientation versus distance from edge for VinV, VinV-S1033A, or VinV-S1033D.

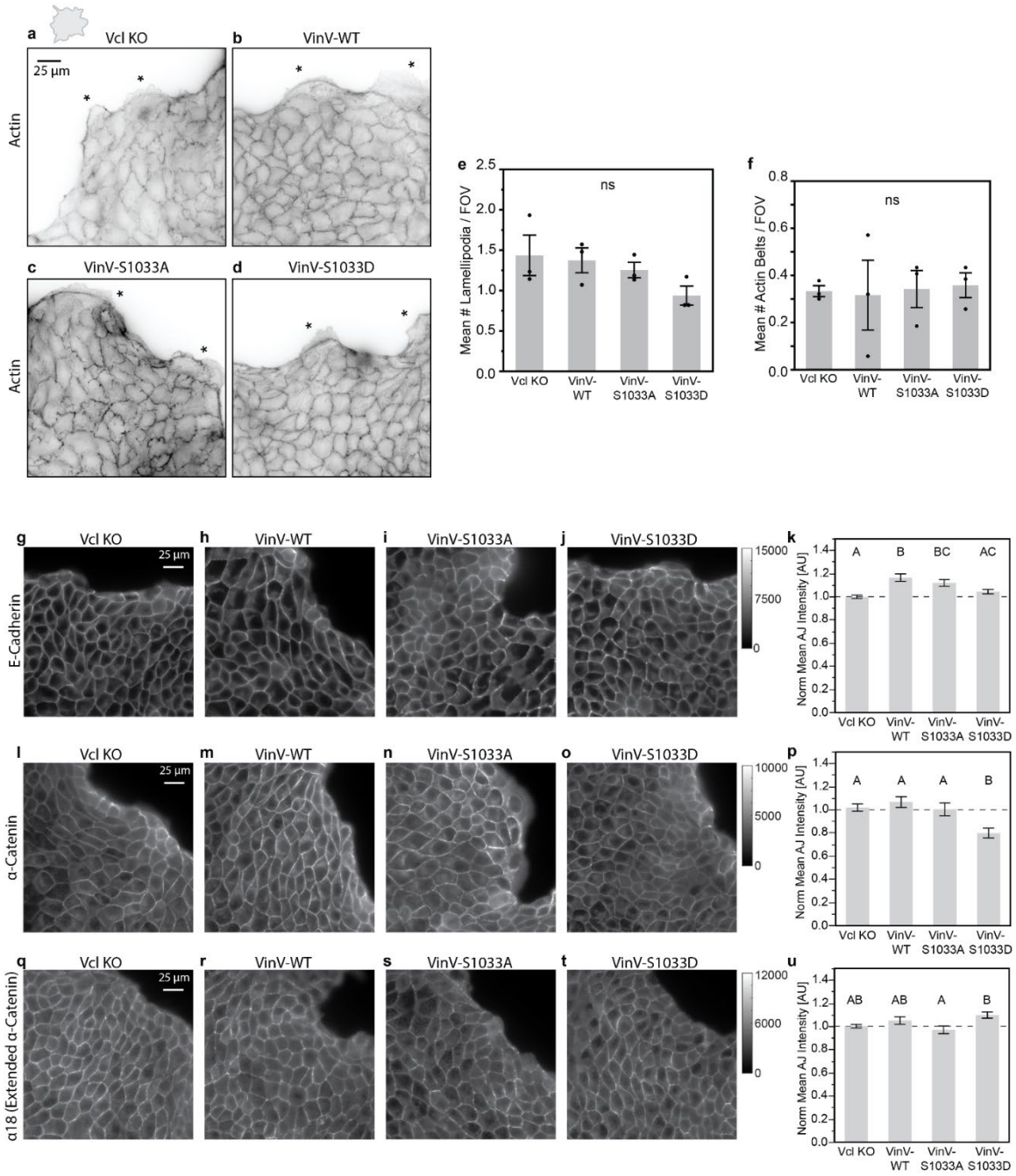

Fig. S10 Effect of expressing VinV or S1033 mutants in MDCK II Vcl KO cells on actin structures and abundance of E-cadherin, α-catenin, and extended α-catenin at AJs. (a-d) Representative images of phalloidin labeling at the edge of migrating MDCK II Vcl KO, VinV, VinV-S1033A, or VinV-S1033D cell monolayers. Stars indicate manually identified lamellipodia. (e-f) Bar plots showing number of lamellipodia per image or number of actin belts per image for MDCK II Vcl KO, VinV, VinV-S1033A, or VinV-S1033D cells (n=3 droplet island assays per cell line over 3 independent experiments). (g-j) Representative images of E-cadherin immunolabeling at the edge of migrating MDCK II Vcl KO, VinV, VinV-S1033A, or VinV-S1033D cell monolayers. (k) Bar plot showing normalized mean E-cadherin stain intensity in AJ masks for MDCK II Vcl KO, VinV, VinV-S1033A, and VinV-S1033D cells (n=48, 44, 41, and 41 images over 3 independent experiments). (i-o) Representative images of α-catenin immunolabeling at the edge of migrating

MDCK II Vcl KO, VinV, VinV-S1033A, or VinV-S1033D cell monolayers. (p) Bar plot showing normalized mean α-catenin stain intensity in AJ masks for MDCK II Vcl KO, VinV, VinV-S1033A, and VinV-S1033D cells (n=37, 39, 36, and 37 images over 3 independent experiments). (q-t) Representative images of α-catenin extended conformation-sensitive antibody (α18) immunolabeling at the edge of migrating MDCK II Vcl KO, VinV, VinV-S1033A, or VinV-S1033D cell monolayers. (u) Bar plot showing normalized mean α-catenin extended conformation-sensitive antibody (α18) stain intensity in AJ masks for MDCK II Vcl KO, VinV, VinV-S1033A, and VinV-S1033D cells (n=36, 37, 35, and 36 images over 3 independent experiments). Bar plots indicate mean +/- SEM. Differences between groups in (e-f) were tested for using ANOVA (ns: not significant). Differences between groups in (k), (p), and (u) were detected using the Steel-Dwass test. Levels not connected by the same letter are significantly different at $p<0.05$.

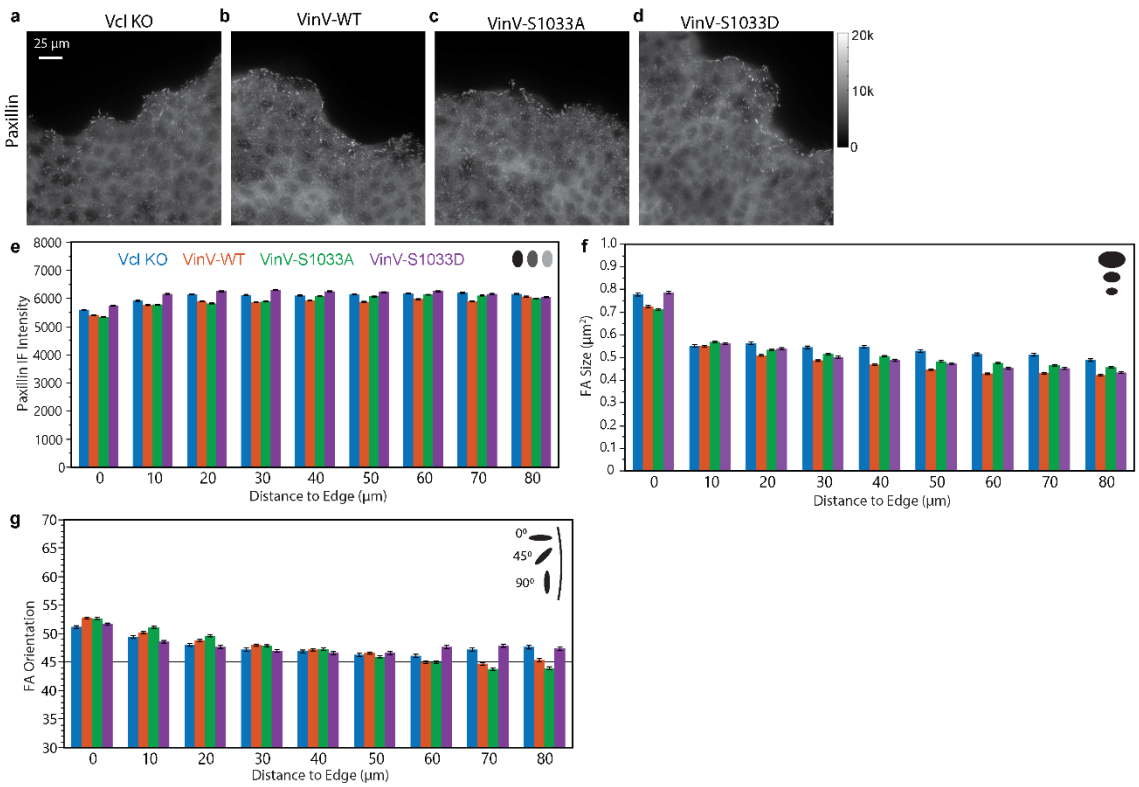

Fig. S11 Effect of expressing VinV or S1033 mutants in MDCK II Vcl KO cells on the intensity, size, and orientation of paxillin-labeled FAs. (a-d) Representative images of paxillin immunolabeling at the edge of migrating MDCK II Vcl KO, VinV, VinV-S1033A, or VinV-S1033D cell monolayers. Plots of paxillin intensity (e), focal adhesion size (f), and focal adhesion edge orientation (g) versus distance from free edge of the monolayer. Bar plots indicate mean +/- SEM.

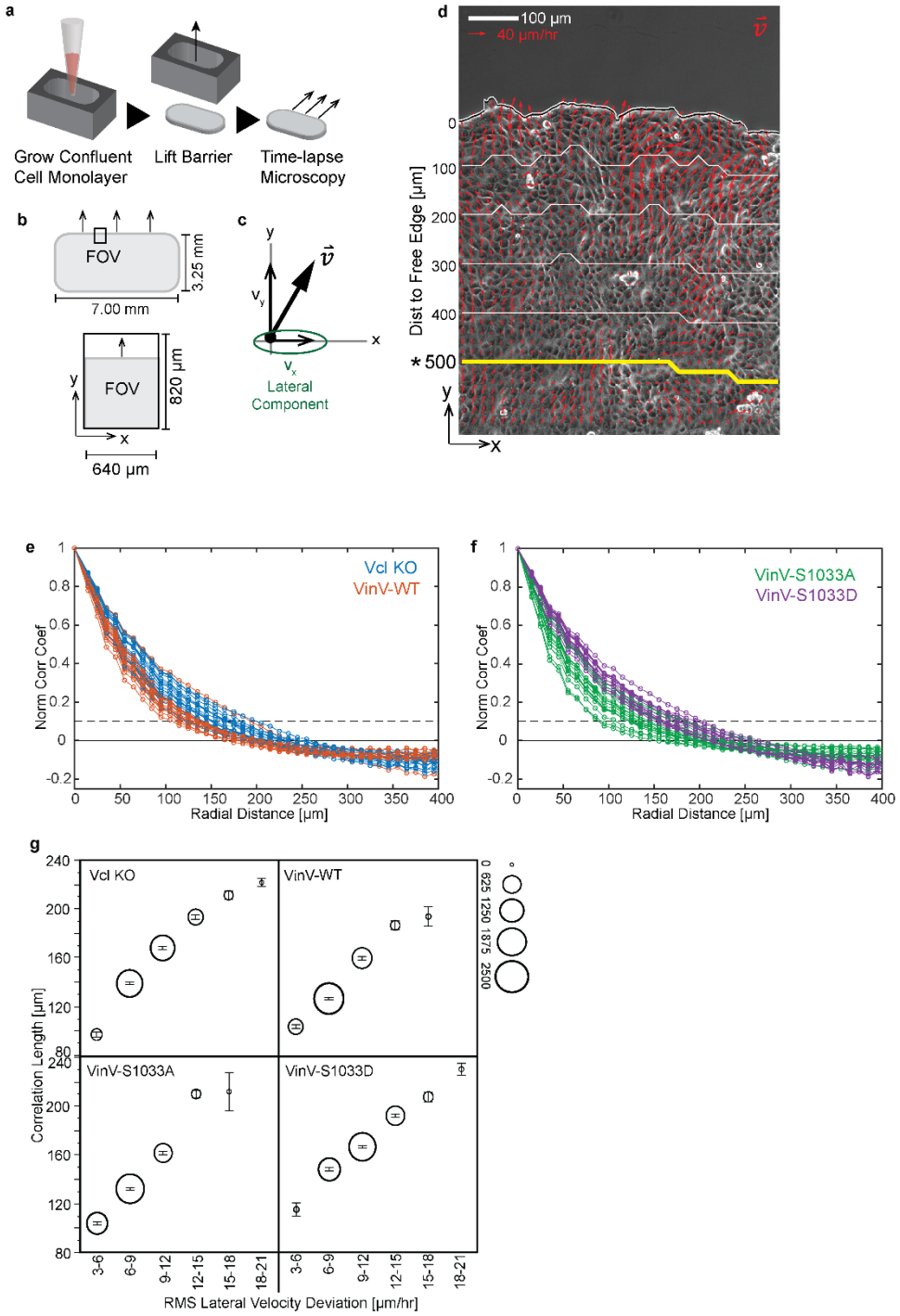

Fig. S12 Quantification of migration in barrier assay. (a) Experimental workflow for barrier assay. (b) Schematics of monolayer and one field of view (FOV) at barrier lift with dimensions and coordinate system. (c) Definition of the velocity vector and its components in the coordinate system, indicating the lateral (x) component used for computing the correlation length in lateral velocity deviations and RMS lateral velocity deviations. (d) Representative phase contrast image of migrating MDCK II Vcl KO cells with velocity field overlaid in red and distances to the free edge indicated in white. Yellow line indicates the region of interest (0 to 500 um from free edge) used for computing all kinematic metrics. (e-f) Plots of time-averaged normalized spatial correlation

coefficient for lateral velocity deviations versus radial distance for MDCK II Vcl KO, VinV, VinV-S1033A, or VinV-S1033D cells (n=16 monolayers for each cell line over 6 independent experiments) with dashed line indicating the threshold value for computing the correlation length. (g) Plots of correlation length for lateral velocity deviations vs binned RMS lateral velocity deviations for individual images and timepoints for MDCK II Vcl KO, VinV, VinV-S1033A, or VinV-S1033D cells (>1,500 timepoints for each cell line). Center of circle indicates mean, error bars indicate SEM, and size of circle indicates number of data points in bin. This figure contains representations of data repeated from Fig 3.

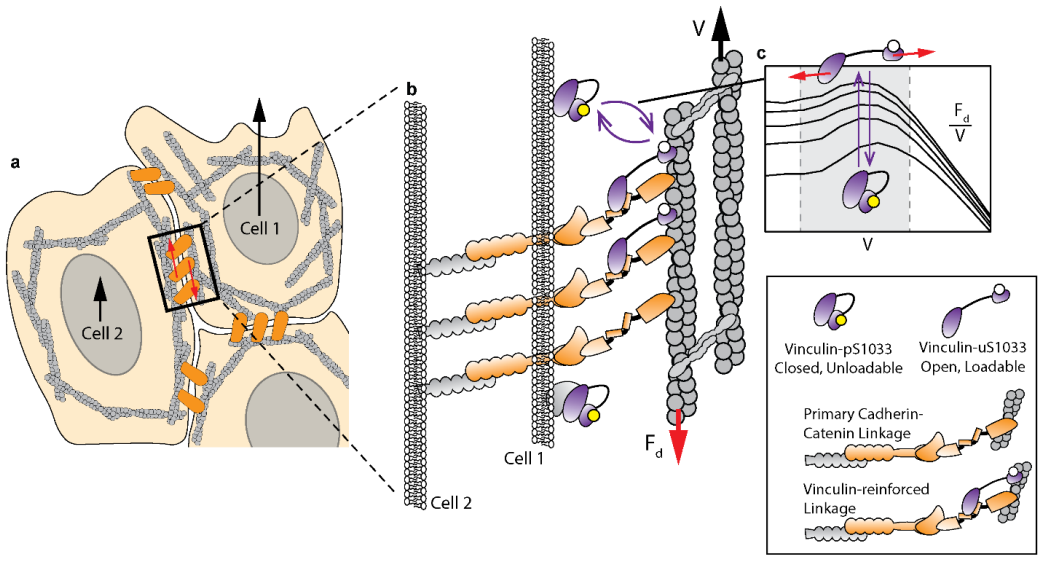

Fig. S13 Working Model for the Role of Vinculin in CCM. A switch for vinculin molecular loading and conformation regulates adhesion-based friction to control cell coupling during CCM. (a) Top view of collectively migrating epithelial cells, indicating the velocities of two adjacent cells whose actin cytoskeletons are linked across an AJ. (b) Enlarged view of some molecular components at the AJ, showing cadherin-catenin complexes connecting the actin cytoskeleton in Cell 1 to cadherins on Cell 2. Cell 1 moves at a speed V relative to Cell 2 in the direction parallel to the cell-cell interface, resulting in a frictional drag force F_d opposing this motion. A localized pool of vinculin in or near the AJ can be toggled between closed, unloadable and open, loadable states, based on the phosphorylation of S1033, to enable rapid reinforcement of the AJ and (c) tuning of the friction coefficient between cells during CCM.

Legends for Supplementary Movies

Movie S1 (separate file). Representative phase contrast timelapse with vector field overlay for migrating MDCK II Vcl KO cells in the barrier migration assay. Length scale bar is 100 μm. Velocity scale arrow is 40 μm/hr. First timepoint is approximately 3 hours post-barrier lift and time between images is 10 min. Total elapsed time from first image is indicated at top right.

Movie S2 (separate file). Representative phase contrast timelapse with vector field overlay for migrating MDCK II Vcl KO cells rescued with VinV in the barrier migration assay. Length scale bar is 100 μm. Velocity scale arrow is 40 μm/hr. First timepoint is approximately 3 hours post-barrier lift and time between images is 10 min. Total elapsed time from first image is indicated at top right.

Movie S3 (separate file). Representative phase contrast timelapse with vector field overlay for migrating MDCK II Vcl KO cells rescued with VinV-S1033A in the barrier migration assay. Length scale bar is 100 μm. Velocity scale arrow is 40 μm/hr. First timepoint is approximately 3 hours post-barrier lift and time between images is 10 min. Total elapsed time from first image is indicated at top right.

Movie S4 (separate file). Representative phase contrast timelapse with vector field overlay for migrating MDCK II Vcl KO cells rescued with VinV-S1033D in the barrier migration assay. Length scale bar is 100 μm. Velocity scale arrow is 40 μm/hr. First timepoint is approximately 3 hours post-barrier lift and time between images is 10 min. Total elapsed time from first image is indicated at top right.

Supplementary Note 1: Models of Adhesion-based Friction at the FA and AJ

I. OVERVIEW

In this supplemental note, we develop molecularly specific, stochastic models of adhesion-based friction at focal adhesions (FAs)/adherens junctions (AJs) based on multi-component integrin-/cadherin-based linkages with force-sensitive bond parameters from single molecule experiments. We use the models to probe the relationship between force-activated binding dynamics and adhesion-based friction existing between adjacent cells and with the extracellular matrix (ECM). The model formulation and implementation are described in Section II. To validate implementation of the friction clutch model and to gain intuition about molecular determinants of friction, we first used a friction clutch model containing generic single-component linkages (Section III-A). As biological linkages in the FAs and AJs are composed of multiple proteins connected through multiple force-sensitive binding interfaces and subject to potential regulation, we developed multi-component integrin-/cadherin-based linkages to use in the friction clutch models (Section III-B). To assess regulators of cell-ECM/cell-cell friction, we incorporated the multi-component integrin-/cadherin-based linkages into the friction clutch model and assessed relationships between molecular properties of linkages and friction at the FA/AJ, including the effect of increasing the fraction of linkages with loadable vinculin (Section III-C/D). We then assessed the robustness of the vinculin-based reinforcement mechanism across a wide range of model parameters (Section III-E). Key assumptions and limitations of the model are discussed in Section IV. Major conclusions are summarized in Section V. Overall, the models indicated that increasing the fraction of loadable vinculin increases the lifetime of cadherin-/integrin-based linkages under load and thereby increases the friction at AJs/FAs across a range of speeds corresponding to cell velocities during collective cell migration (CCM). The effect is larger at AJs than FAs. Increases in friction were associated with increases in ensemble vinculin molecular tension, and the effect of vinculin was robust to other model parameters. In the context of macroscopic physical models of CCM, the effect of vinculin loading on adhesion-based friction is consistent with the observed effects of loaded vinculin on CCM dynamics in our experimental system.

II. MODEL CONCEPTUALIZATION AND FORMULATION

Adherent cell migration requires the transmission of forces to the environment, and in the case of collective cell migration, between cells (1-3). This process occurs at low Reynolds number, where cell-generated forces that propel the cell forward are balanced by drag forces that resist motion. Propulsive forces are generated mainly by active processes in the cytoskeleton and are transmitted to the surrounding via specific adhesions. The predominant source of drag forces in adherent cell migration are the connections between the cell body/cytoskeleton and the external surroundings by specific adhesions. Drag arising from frictional forces at cell-ECM adhesions play a major role in single cell migration (4), and drag forces at both the cell-ECM and cell-cell interfaces play a role in collective cell migration (5, 6). As such, frictional forces at the cell-ECM and cell-cell interfaces are important components of physical models of CCM (1). However, the molecular mechanisms that regulate these physical parameters remain poorly understood.

The transmission of forces between the actin cytoskeleton and the ECM or adjacent cells is mediated by specialized adhesion structures, termed focal adhesions (FAs) or adherens junctions (AJ), respectively (2, 3). FAs mechanically couple the actin cytoskeleton to the ECM through integrin transmembrane proteins and various cytosolic adapter proteins. AJs mechanically couple the actin cytoskeletons of adjacent cells through cadherin transmembrane proteins and a set of adapter proteins.

To understand molecular regulators of friction at the FA (cell-ECM) and AJ (cell-cell), and to investigate the role of vinculin mechanical loading, we used an existing friction clutch framework, which predicts the resistive force due to the sliding of two surfaces relative to each

other at a particular speed as a function of the number and properties of adhesive linkages between these surfaces (7). Similar frameworks based on adhesive bond dynamics have also been applied to the cell-ECM and cell-cell drag coefficients in macroscopic models of collective cell migration (5). In FAs/AJs, integrin-/cadherin-based linkages contain force-sensitive bonds at multiple interfaces, to F-actin internally and the ECM (Integrin:FN) or adjacent cell (E-Cad:E-Cad) externally (8). Additionally, both FAs and AJs undergo adhesion strengthening in response to applied forces, which involves the reinforcement of connections to the actin cytoskeleton via mechanical linker proteins like vinculin (9-15). We hypothesized that vinculin, due to its strong catch bond with F-actin (16), could affect the force-dependent engagement of molecular linkages at FAs and/or AJs and thereby friction. The primary load-bearing linkage at the FA is Integrin:Talin:F-actin and at the AJ is the minimal cadherin-catenin-F-actin complex (Cadherin:β-Catenin:α-Catenin:F-actin), both of which can be reinforced with an additional mechanical connection to F-actin via the adapter protein vinculin (8). Given their importance in force transmission across the FA and AJ, significant work has been conducted to characterize the force-sensitivity of bonds in these multi-protein linkages. In the integrin-based linkage, the force-sensitivities of various integrin heterodimers and ligand pairs, including the Integrin-α5β1:FN (17) and Integrin-αVβ3:FN (18) bonds, as well as the Talin:F-actin (19) and Vinculin:F-actin (16) bonds have been characterized at the single molecule level. In the cadherin-based linkage, the force-sensitive bond kinetics of both the E-cadherin trans-dimer (20) and the α-Catenin:F-actin bond (21) have been elucidated using single molecule techniques. Using force-sensitive bond kinetics from the single molecule literature, we developed models of reinforceable, multi-component integrin-/cadherin-based mechanical linkages connecting the actin cytoskeleton to an external surface at FAs/AJs. The multi-component linkages account for force-sensitive bond dynamics at key interfaces, enabling us to assess what limits force transmission at the molecular scale and how reinforcement via an adapter protein, here vinculin, affects force transmission.

A. Mechanics of Friction Clutch Models

As a starting point, we utilized an existing framework for modeling the sliding friction due to adhesive bonds between an actin filament moving with an imposed velocity over a fixed surface (7). The model considers a 1D interface connected by molecular linkages that behave like Hookean springs and dynamically bind/unbind. The linkages are stretched by the relative motion at the interface and exert a restoring force proportional to their extension. In this work, we extend this framework by incorporating regulatable multi-component linkages. In the FA model, integrin-based molecular linkages connect the actin network inside the cell to ECM ligands on the substrate (Fig. S14a-c). These linkages bind/unbind at two interfaces, the Integrin:FN bond and the Talin:F-actin bond (Section II-B), and can be reinforced with vinculin (Section II-D/E). Similarly, in the AJ model, E-cadherin-based molecular linkages connect the actin network of one cell to cadherins on the surface of the adjacent cell (Fig. S14d-f). These linkages bind/unbind at two interfaces, the E-cadherin trans-dimer and the α-Catenin:F-actin bond (Section II-C), and can be reinforced with vinculin (Section II-D/F). We refer to these models as friction clutch models because we use them to investigate adhesion-based friction at the FA or AJ that resists relative motion at the cell-ECM or cell-cell interfaces, respectively, occurring during cell migration. We note that the friction clutch model is similar to previously described motor clutch models, which have been used to understand the relationship between actomyosin retrograde flow at the leading edge and cell-ECM traction forces as well as the process of ECM stiffness sensing (18, 22-24). The main difference is that in motor clutch models the motion of actin that loads the linkages is driven by an ensemble of myosin motors with a variable, force-dependent speed based on properties of motor stalling, instead of an imposed speed used in the friction clutch models here.

When molecular linkages are bound at both interfaces, they are engaged and transmit forces from the actin cytoskeleton inside the cell to the external substrate (FA) or adjacent cell (AJ). Engaged linkages are represented as a set of parallel springs each with spring constant K_{Link}, and they are together in series with an external spring with spring constant K_{Ext}, which represents the substrate (FA) or the adjacent cell (AJ). Engaged linkages are extended and loaded by a constant velocity, V, corresponding to the motion between the actin cytoskeleton (cell body) with respect to the substrate (FA) or the adjacent cell (AJ). At each time step, the total

extension of the ith engaged linkage (x_i) with respect to the resting position of the clutch system is updated according to the following equation:

$$x_i(t + \Delta t) = x_i(t) + V\Delta t \quad \text{(eq. S1)}$$

The total force transmitted across the linkages, F_{TOT}, is found by imposing a force balance across the ensemble of N_{Eng} engaged linkage springs that are in series with the external spring.

$$F_{TOT} = \sum_{i=1}^{N_{Eng}} F_{Link,i} = F_{Ext} \quad \text{(eq. S2)}$$

The external force is related to the extension of the external spring, x_{Ext}, by the external spring constant:

$$F_{Ext} = x_{Ext}K_{Ext} \quad \text{(eq. S3)}$$

The force across an engaged linkage is given by the product of the linkage spring constant and extension of the linkage, $x_{Link,i}$, which is determined by subtracting the extension of the external spring, x_{Ext}, from the total extension of the engaged linkage with respect to the resting position of the clutch system, x_i ($x_i = x_{Link,i} + x_{Ext}$).

$$F_{Link,i} = K_{Link}x_{Link,i} = K_{Link}(x_i - x_{Ext}) \quad \text{(eq. S4)}$$

From these relationships, the total force can be solved for in terms of the spring constants, number of engaged linkages, and the total extension of each engaged linkage:

$$F_{TOT} = \frac{K_{Ext}K_{Link}\sum_{i=1}^{N_{Eng}} x_i}{K_{Ext} + K_{Link}N_{Eng}} \quad \text{(eq. S5)}$$

Note that this expression for total force is the same relationship used in previous motor-clutch models (22, 24), and that the framework used here is equivalent to that of previous motor-clutch models, except that the velocity is constant (corresponding to relative cell motion) instead of force-dependent (as for myosin motor-driven actin flow). From the above Equations S2-5, the extension of the external spring, x_{Ext}, extension of each linkage, $x_{Link,i}$, and force across each linkage, $F_{Link,i}$, are determined at the current time. Parameters for the FA and AJ friction clutch models are given in Table S1.

Table S1. Parameters for FA and AJ Friction Clutch Models.

Parameter Name	Parameter Symbol	FA Friction Clutch	AJ Friction Clutch	Rationale
Speed	V	Base Value*: 2.778 nm/s (10 μm/hr) Sweep Range: [0.1, 100] nm/s ([0.36,360] μm/hr)	Base Value: 2.778 nm/s (10 μm/hr) Sweep Range: [0.1, 100] nm/s ([0.36,360] μm/hr)	FA and AJ**: Base value inside range of MDCK monolayer velocities observed in this work and elsewhere (25), ~1-30 μm/hr or ~0.28-8.33 nm/s. Sweep range extends below and above this range.
Linkage Spring Constant	K_{Link}	5 pN/nm	5 pN/nm	FA and AJ: On order of the effective stiffness of many mechanical proteins (26). Also, matches value used in previous motor-clutch model of FA (23) and is similar to the experimentally determined value for a cadherin superfamily member, PCDH15 (27).
Number of Linkages	N_{Link}	50	50	FA and AJ: Matches previous motor-clutch models (22, 23). Correspond to number of integrins or cadherins in adhesive clusters of radius ~100 nm at reported densities of integrin (28) and cadherin (29) molecules in clusters.
Binding Rate Constants (bond indicated in superscript and parentheses)	FA: $k_{01}^{Intg:FN}$, $k_{01}^{Tal:Factin}$, $k_{01}^{Vcl:Factin}$, $k_{01}^{Vcl:Tal}$ AJ: $k_{01}^{Cad:Cad}$, $k_{01}^{aCat:Factin}$, $k_{01}^{Vcl:Factin}$, $k_{01}^{Vcl:aCat}$	2/s (Intg:FN) 2/s (Tal:F-actin) 2/s (Vcl:F-actin) 1/s (Vcl:Tal)	2/s (Cad:Cad) 2/s (α-Cat:F-actin) 2/s (Vcl:F-actin) 1/s (Vcl:α-Cat)	FA and AJ: Similar to previous motor-clutch model with multiple binding interfaces (30). Also, resulting engagement rate for combined linkage is similar to the binding rate constant for single-component linkages in previous motor-clutch models (22, 23).
Unbinding Rate Constants	See Tables S2-S3	Force-Dependent Unbinding Rate Models in Table S2	Force-Dependent Unbinding Rate Models in Table S3	See Tables S2-S3
Fraction of linkages with loadable vinculin	ρ_{Vcl}	Base Value: 0 (non-reinforced) or 1 (fully reinforced) Sweep Range: [0, 1]	Base Value: 0 (non-reinforced) or 1 (fully reinforced) Sweep Range: [0, 1]	FA and AJ: Varied across full range to assess effect of vinculin mechanical reinforcement.
External Spring Constant [pN/nm]	K_{Ext}	10^6 pN/nm	3.16 pN/nm	FA: Set arbitrarily high to match experimental condition in this paper (glass). AJ: Corresponds to estimates of the stiffness of cell monolayers (31, 32) (~20-33 kPa). See Section II-J for conversion from elastic modulus to spring constant.

Table Notes: *For parameters that were swept, the base value and sweep value range are given. **Labels indicate whether rationales apply to only FA ("FA"), only AJ ("AJ"), or both FA and AJ ("FA and AJ"). ***Sensitivity analyses were conducted on all major parameters over +/- 1 decade (see Section III-E).

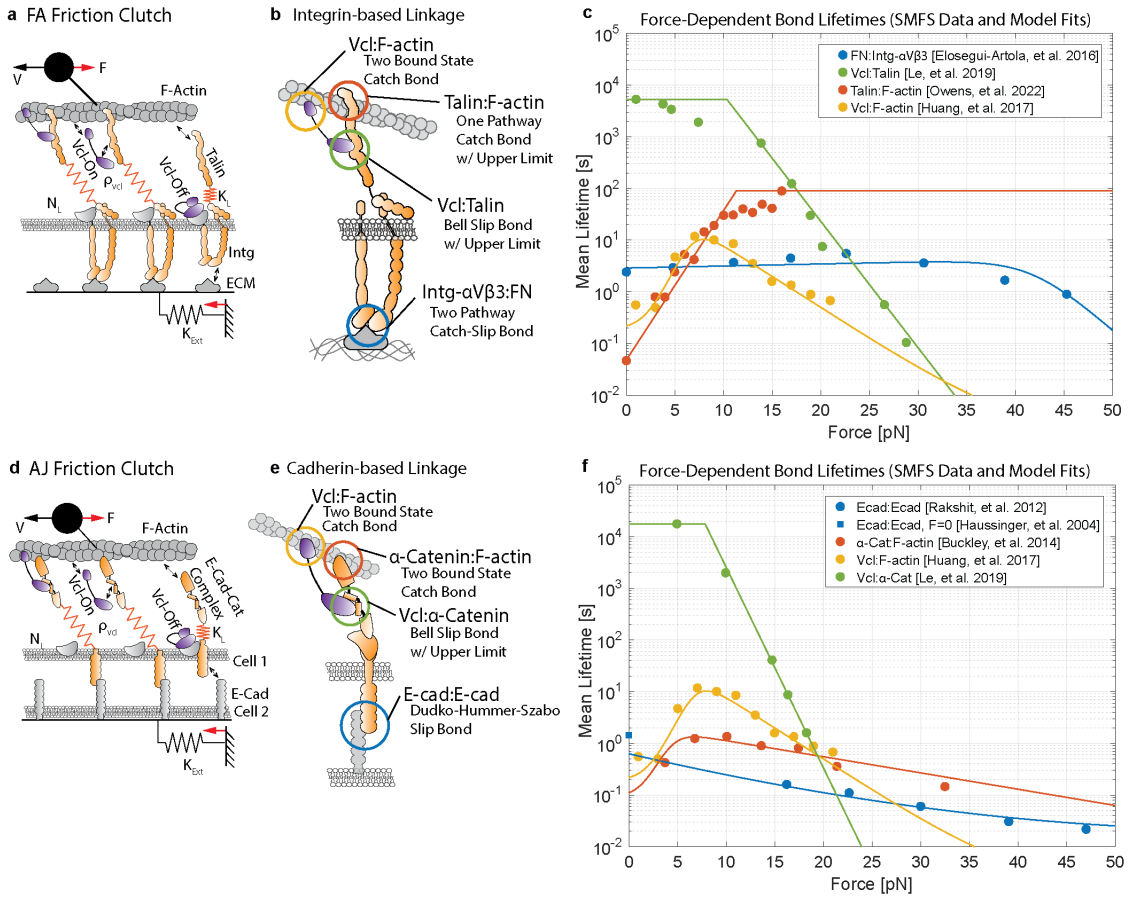

Fig. S14 Model Formulation for FA and AJ Friction Clutch. (a) Schematic of FA friction clutch model. (b) Schematic of multi-component integrin-based linkage in FA model indicating binding/unbinding interfaces with the type of force-dependent bond model used for the unbinding rate constants. (c) Plot of mean bond lifetime versus force for each bond in the integrin-based linkage. Data points are reproduced from the indicated experimental studies (16, 18, 19, 33) and lines represent the respective model fit (see Table S2). (d) Schematic of AJ friction clutch model. (e) Schematic of multi-component cadherin-based linkage in AJ model indicating binding/unbinding interfaces with the type of force-dependent bond model used for the unbinding rate constants. (f) Plot of mean bond lifetime versus force for each bond in the cadherin-based linkage. Data points are reproduced from the indicated experimental studies (16, 20, 21, 33, 34) and lines represent the respective model fit (see Table S3).

B. Binding/Unbinding Dynamics in Integrin-based Linkage without Vinculin Reinforcement

In the FA model, integrin-based molecular linkages dynamically bind/unbind at two interfaces, the Integrin:FN bond (referred to as the integrin interface) and the Talin:F-actin bond (referred to as the F-actin interface) (Fig. S14b). We chose to model binding/unbinding at these two interfaces, but not between talin and integrin, because there are limited measurements of the force-sensitivity of Talin:Integrin bonds and the fact that Talin is known to be proteolyzed by calpain to facilitate FA release suggests that the Talin:Integrin bond is strong (35). Also, the fact that vinculin increases the tension across Talin suggests that the Talin:F-actin bond is weaker than the Talin:Integrin bond (36).

The Integrin:FN bond is modeled as a single state, two-pathway catch-slip bond, as in previous FA motor-clutch models, and is based on experimental measurements of the bond between Integrin-αVβ3 and FN (18). Integrin-αVβ3 was used because Integrin-αV is required for

mechanotransduction in collectively migrating MDCK cells (37). The state variable for the Integrin:FN bond in the jth linkage is given by:

$$\theta_j^{Intg:FN} = \begin{cases} 0 & Unbound\ State \\ 1 & Bound\ State \end{cases} \quad \text{(eq. S6)}$$

In the Integrin:FN bond, binding ($\theta_j^{Intg:FN}: 0 \rightarrow 1$) occurs with the force-independent rate constant $k_{01}^{Intg:FN}$ and unbinding ($\theta_j^{Intg:FN}: 1 \rightarrow 0$) occurs with the force-dependent rate constant function $k_{10}^{Intg:FN}(F)$ defined in Table S2, where F denotes the force across the bond (see Fig. S14c for plot of mean lifetime versus force).

The Talin:F-actin bond is modeled as a as a one state catch bond based on single molecule experiments with Talin ABS3 and F-actin (19), with a maximum lifetime. The state variable for the Talin:F-actin bond in the jth linkage is given by:

$$\theta_j^{Tal:Factin} = \begin{cases} 0 & Unbound\ State \\ 1 & Bound\ State \end{cases} \quad \text{(eq. S7)}$$

In the Talin:F-actin bond, binding ($\theta_j^{Tal:Factin}: 0 \rightarrow 1$) occurs with the force-independent rate constant $k_{01}^{Tal:Factin}$ and unbinding ($\theta_j^{Tal:Factin}: 1 \rightarrow 0$) occurs with the force-dependent rate constant function $k_{10}^{Tal:Factin}(F)$ defined in Table S2, where F denotes the force across the bond.

To be engaged and transmit forces from the actin cytoskeleton to FN ligands on the substrate, a molecular linkage must be bound at both the integrin and the actin interfaces. This is indicated by the engagement state variable for the jth linkage, Θ_j, which equals 1 when engaged and 0 when disengaged:

$$\Theta_j = \begin{cases} 1 & \theta_j^{Intg:FN} > 0 \wedge \theta_j^{Tal:Factin} > 0 \\ 0 & elsewhere \end{cases} \quad \text{(eq. S8)}$$

where $\wedge$ is the logical operator "and". Disengaged linkages ($\Theta_j = 0$) experience no extension ($x_{Link,j} = 0$) and thus no force ($F_{Link,j} = 0$). When a linkage transitions from disengaged to engaged ($\Theta_j: 0 \rightarrow 1$), its total extension with respect to the resting position of the clutch system is set to $x_j = x_{Ext}$ because $x_{Link,j} = 0$ at the onset of engagement. Once engaged, the linkage is loaded and extended by the actin as one of the N_{Eng} engaged linkages described previously (Section II-A). The force across a linkage is thus given by:

$$F_{Link,j} = \begin{cases} K_{Link} x_{Link,j} & \Theta_j = 1 \\ 0 & \Theta_j = 0 \end{cases} \quad \text{(eq. S9)}$$

where the linkage extension $x_{Link,j}$ (defined for engaged linkages) is equal to the total extension of the linkage with respect to the resting position of the clutch system (x_j) minus the extension component of the external spring (x_{Ext}): $x_{Link,j} = x_j - x_{Ext} = x_j - \frac{F_{TOT}}{K_{Ext}}$. Because the actin and integrin interfaces are in series, the Integrin:FN and Talin:F-actin bonds both experience the entire linkage force in the minimal integrin-based linkage:

$$F_{Link,j}^{Intg:FN} = F_{Link,j}^{Tal:Factin} = F_{Link,j} \quad \text{(eq. S10)}$$

These bond forces affect unbinding kinetics according to the force-dependent unbinding rate constants described above with parameters in Table S2. Lastly, when the bond at either interface breaks, the linkage returns to a disengaged state, in which it experiences no extension and bears no force. We note that in simulations the state variables, extension, and force for each linkage is tracked. We do not explicitly model the absolute position of linkages, sites on F-actin, or sites on

the substrate (or adjacent cell surface for AJ). However, a physical interpretation of disengaged linkages is as follows. Linkages that unbind from the actin interface remain at the position of the ECM on the substrate (or the cadherin on the adjacent cell for AJ) to which they are bound and may rebind F-actin. Linkages that unbind from the integrin interface (or cadherin interface for AJ) remain at the position of their bond with F-actin and are free to bind other FN molecules on the substrate (or cadherin molecules on the adjacent cell for AJ).

Table S2. Force-Dependent Unbinding Kinetics for Integrin-based Linkage.

Bond	Model and States	Model Equation(s)	Parameter Values			Literature Reference
Talin: F-actin	Catch Bond with Upper Lifetime Limit 0 = Unbound 1 = Bound	$k_{10}(F) = \max\left\{k_0 \exp\left(Fx/k_BT\right), \frac{1}{\tau_{max}}\right\}$	k_0 x τ_{max}	21.0084 -2.7412 89.3450	1/s nm s	SMFS data and model fit from Owen et al. (19), for Talin-ABS3 in the negative pull direction. Model fit is single exponential from Owen et al. with max lifetime corresponding to lifetime at max force probed.
Vinculin: F-actin	Two Bound State Catch Bond 0 = Unbound 1= Weak Bound 2 = Strong Bound	$k_{10}(F) = k_{10}^0 \exp\left(Fx_{10}/k_BT\right)$ $k_{20}(F) = k_{20}^0 \exp\left(Fx_{20}/k_BT\right)$ $k_{12}(F) = k_{12}^0 \exp\left(Fx_{12}/k_BT\right)$ $k_{21}(F) = k_{21}^0 \exp\left(Fx_{21}/k_BT\right)$	k_{10}^0 x_{10} k_{20}^0 x_{20} k_{12}^0 x_{12} k_{21}^0 x_{21}	5.3 0 5.5E-3 1.2 6.1 0.4 43 -3.4	1/s nm 1/s nm 1/s nm 1/s nm	SMFS data and model fit from Huang et al. (16), for Vcl-T12 in the negative pull direction.
Vinculin: Talin	Bell Slip Bond with Upper Lifetime Limit 0 = Unbound 1 = Bound	$k_{10}(F) = \max\left\{k_0 \exp\left(Fx/k_BT\right), \frac{1}{\tau_{max}}\right\}$	k_0 x τ_{max}	5.57E-7 2.3164 5311.09	1/s nm s	SMFS data from Le et al. (33). Data fit to Bell Model with max lifetime corresponding to lifetime at lowest force probed.
Integrin: FN	Two-Pathway Catch-Slip Bond 0 = Unbound 1 = Bound	$k_{10}(F) = k_1^0 \exp\left(Fx_1/k_BT\right) + k_2^0 \exp\left(Fx_2/k_BT\right)$	k_1^0 x_1 k_2^0 x_2	0.3471 -0.03741 2.87E-8 1.5669	1/s nm 1/s nm	SMFS data for Integrin-αVβ3:FN bond from Elosegui-Artola et al. (18) fit to two-pathway catch-slip model (38).

Table Notes: $k_BT = 4.11$ pN*nm

C. Binding/Unbinding Dynamics in Cadherin-based Linkage without Vinculin Reinforcement

In the AJ model, molecular linkages dynamically bind/unbind at two interfaces, the E-cadherin trans-dimer (referred to as the cadherin interface) and the α-Catenin:F-actin bond (referred to as the F-actin interface) (Fig. S14e). As such, the model framework is similar to that of the integrin-based linkage, but with different kinetic parameters. We chose to model binding/unbinding at these two interfaces, but not within the E-cadherin-catenin complex, because the affinities of interactions within the E-cadherin-catenin complex (39) (K_d ~ 1 nM) are substantially higher than those of the E-cadherin-catenin complex for F-actin (40) (K_d~1 μM) and the E-cadherin trans-dimer (41) (K_d~100 μM). Additionally, when subjected to mechanical loads up to 10 pN the α-Catenin:β-Catenin complex exhibits a lifetime of tens to hundreds of seconds, indicating it has a substantially higher mechanical stability than that of the E-cadherin trans-dimer or α-Catenin:F-actin bond (42).

The E-cadherin:E-cadherin bond is modeled as a single state slip bond based on single molecule experiments with WT and K14E E-cadherin (20). The state variable for the E-cadherin:E-cadherin bond in the jth linkage is given by:

$$\theta_j^{Cad:Cad} = \begin{cases} 0 & Unbound\ State \\ 1 & Bound\ State \end{cases} \quad \text{(eq. S11)}$$

In the E-cadherin:E-cadherin bond, binding ($\theta_j^{Cad:Cad}: 0 \rightarrow 1$) occurs with the with the force-independent rate constant $k_{01}^{Cad:Cad}$ and unbinding ($\theta_j^{Cad:Cad}: 1 \rightarrow 0$) occurs with the force-dependent rate constant function $k_{10}^{Cad:Cad}(F)$ defined in Table S3, where F denotes the force across the bond (see Fig. S14f for plot of mean lifetime versus force).

The α-Catenin:F-actin bond is modeled as a two-bound state catch-slip bond based on single molecule experiments with F-actin and the E-cadherin-catenin complex (21). The state variable for the α-Catenin:F-actin bond in the jth linkage is given by:

$$\theta_j^{aCat:Factin} = \begin{cases} 0 & Unbound\ State \\ 1 & Weak\ Bound\ State \\ 2 & Strong\ Bound\ State \end{cases} \quad \text{(eq. S12)}$$

In the α-Catenin:F-actin bond, binding only occurs from the unbound to weak bound state ($\theta_j^{aCat:Factin}: 0 \rightarrow 1$) with the rate constant $k_{01}^{aCat:Factin}$, as done previously for a two-state catch-slip bond in a model of adhesion-based actin coupling (16). Rate constants for unbinding from the weak state ($\theta_j^{aCat:Factin}: 1 \rightarrow 0$), $k_{10}^{aCat:Factin}(F)$; unbinding from the strong state ($\theta_j^{aCat:Factin}: 2 \rightarrow 0$), $k_{20}^{aCat:Factin}(F)$; and interconversion between the weak and strong states ($\theta_j^{aCat:Factin}: 1 \rightarrow 2$ and $\theta_j^{aCat:Factin}: 2 \rightarrow 1$), $k_{12}^{aCat:Factin}(F)$ and $k_{21}^{aCat:Factin}(F)$, are defined in Table S3.

To be engaged and transmit forces from the actin cytoskeleton to cadherins on the surface of the adjacent cell, a molecular linkage must be bound at both the cadherin and the actin interfaces. This is indicated by the engagement state variable for the jth linkage, Θ_j, which equals 1 when engaged and 0 when disengaged:

$$\Theta_j = \begin{cases} 1 & \theta_j^{Cad:Cad} > 0 \wedge \theta_j^{aCat:Factin} > 0 \\ 0 & elsewhere \end{cases} \quad \text{(eq. S13)}$$

where ∧ is the logical operator “and”. Disengaged linkages ($\Theta_j = 0$) experience no extension ($x_{Link,j} = 0$) and thus no force ($F_{Link,j} = 0$). When a linkage transitions from disengaged to engaged ($\Theta_j: 0 \rightarrow 1$), its total extension with respect to the resting position of the clutch system is set to $x_j = x_{Ext}$ because $x_{Link,j} = 0$ at the onset of engagement. Once engaged, the linkage is loaded and extended by the actin as one of the N_{Eng} engaged linkages described previously (Section II-A). The force across a linkage is thus given by:

$$F_{Link,j} = \begin{cases} K_{Link} x_{Link,j} & \Theta_j = 1 \\ 0 & \Theta_j = 0 \end{cases} \quad \text{(eq. S14)}$$

where the linkage extension $x_{Link,j}$ (defined for engaged linkages) is equal to the total extension of the linkage with respect to the resting position of the clutch system (x_j) minus the extension component of the external spring (x_{Ext}): $x_{Link,j} = x_j - x_{Ext} = x_j - \frac{F_{TOT}}{K_{Ext}}$. Because the actin and cadherin interfaces are in series, the E-cadherin:E-cadherin and α-Catenin:F-actin bonds both experience the entire linkage force in the minimal cadherin-catenin linkage:

$$F_{Link,j}^{Cad:Cad} = F_{Link,j}^{aCat:Factin} = F_{Link,j} \quad \text{(eq. S15)}$$

These bond forces affect unbinding kinetics according to the force-dependent unbinding rate constants described above with parameters in Table S3. As with the integrin-based linkage, when the bond at either interface breaks, the linkage returns to a disengaged state, in which it experiences no extension and bears no force (see Section II-B for more information).

Table S3. Force-Dependent Unbinding Kinetics for Cadherin-based Linkage.

Bond	Model and States	Model Equation(s)	Parameter Values			Literature Reference
α-Catenin: F-actin	Two Bound State Catch Bond 0 = Unbound 1= Weak Bound 2 = Strong Bound	$k_{10}(F) = k_{10}^0 \exp(Fx_{10}/k_BT)$ $k_{20}(F) = k_{20}^0 \exp(Fx_{20}/k_BT)$ $k_{12}(F) = k_{12}^0 \exp(Fx_{12}/k_BT)$ $k_{21}(F) = k_{21}^0 \exp(Fx_{21}/k_BT)$	k_{10}^0 x_{10} k_{20}^0 x_{20} k_{12}^0 x_{12} k_{21}^0 x_{21}	11 0 0.14 0.4 3 0.2 20 -4	1/s nm 1/s nm 1/s nm 1/s nm	SMFS data and model fit from Buckley et al. (21).
Vinculin: F-actin	Two Bound State Catch Bond 0 = Unbound 1= Weak Bound 2 = Strong Bound	$k_{10}(F) = k_{10}^0 \exp(Fx_{10}/k_BT)$ $k_{20}(F) = k_{20}^0 \exp(Fx_{20}/k_BT)$ $k_{12}(F) = k_{12}^0 \exp(Fx_{12}/k_BT)$ $k_{21}(F) = k_{21}^0 \exp(Fx_{21}/k_BT)$	k_{10}^0 x_{10} k_{20}^0 x_{20} k_{12}^0 x_{12} k_{21}^0 x_{21}	5.3 0 5.5E-3 1.2 6.1 0.4 43 -3.4	1/s nm 1/s nm 1/s nm 1/s nm	SMFS data and model fit from Huang et al. (16), for Vcl-T12 in the negative pull direction.
Vinculin: α-Catenin	Bell Slip Bond with Upper Lifetime Limit 0 = Unbound 1 = Bound	$k_{10}(F) = \max\left\{k_0 \exp(Fx/k_BT), \frac{1}{\tau_{max}}\right\}$	k_0 x τ_{max}	5.136E-8 3.6771 1.7691E4	1/s nm s	SMFS data from Le et al. (33). Data fit to Bell Model with max lifetime corresponding to lifetime at lowest force probed.
E-cad trans-dimer	Slip bond for cusp free energy surface 0 = Unbound 1 = Bound	$k_{10}(F) = k_0\left(1 - \frac{vFx^\#}{\Delta G^\#}\right)^{1/v-1} \exp\left(\frac{\Delta G^\#}{k_BT}\left[1 - \left(1 - \frac{vFx^\#}{\Delta G^\#}\right)^{1/v}\right]\right)$	v k_0 $x^\#$ $\Delta G^\#$	0.5 1.5873 0.46 20.6	 1/s nm k_BT	SMFS data and global model fit for K14E and WT E-cadherin from Rakshit et al. (20). Model originates from Dudko et al. (43). Fit for K14E and WT E-cadherin used because strand swap-dimer is dominant form at equilibrium and the transition from X-dimer to SS-dimer occurs very rapidly. Note: Model fit at F=0 also agrees well with off-rate measurements in solution (34).

Table Notes: $k_BT = 4.11$ pN*nm

D. Vinculin Reinforcement of Integrin- and Cadherin-based Linkages

Vinculin is a mechanical linker protein that localizes to both FAs and AJs, where it mediates connections to the actin cytoskeleton involved in transmitting forces across these structures (44). Vinculin is also subject to a head-tail autoinhibitory interaction, existing in at least two states, open and closed (44). Together, key aspects of vinculin function are determined by the mechanical loads its experiences and its conformation (9, 44). At FAs, vinculin is recruited to the membrane-proximal integrin compartment in a closed conformation via interactions with

Paxillin or to the membrane via PIP2, and it moves upward to engage F-actin via a transition to an open conformation and interaction with Talin (45). At AJs, vinculin also bridges a membrane-proximal cadherin-catenin compartment and a membrane distal F-actin compartment, and this depends on its transition to an open conformation and interactions with α-Catenin (46).

Therefore, to investigate the effect of vinculin on the transmission of forces across integrin- and cadherin-based molecular linkages, we modeled vinculin's ability to form a second reinforcing mechanical connection to F-actin. Specifically, we modeled the behavior of vinculin inside mechanical linkages in two states: (1) closed and unable to bear loads in a localized pool at or near FAs/AJs (bound to the membrane or another unloaded component of the FA/AJ), or (2) open and able to bear loads in the FA/AJ (bound to an exposed cryptic binding site in Talin/α-Catenin and F-actin). In these linkages, vinculin is free to bind a VBS on either Talin or α-Catenin with its head domain and F-actin with its tail domain, and thus its ability to bear loads is subject to this binding kinetics. In the context of the S1033-based vinculin regulatory switch, where mutation of S1033 affected vinculin load and conformation but not localization to FAs/AJs, the unloadable and loadable states correspond to the phosphorylated and unphosphorylated states of vinculin, respectively. As we experimentally observed spatial variations in vinculin conformation and loading at both FAs and AJs, we assessed the effect of varying the fraction of loadable vinculin, ρ_{Vcl}. This parameter is used to set the number of linkages in the Reinforced and Non-Reinforced Configurations as follows:

$$N_{Link,Reinforced} = [\rho_{Vcl} N_{Link}] \quad \text{(eq. S16)}$$

$$N_{Link,Non-Reinforced} = N_{Link} - N_{Link,Reinforced} \quad \text{(eq. S17)}$$

where brackets denote rounding to the nearest integer. Lastly, aside from the Reinforced and Non-Reinforced Configurations described above, the role of the Vcl:F-actin bond was assessed in a separate set of simulations with all linkages in a third configuration in which binding to the actin interface occurs exclusively via the Vcl:F-actin bond (called "Vcl Only Configuration").

E. Binding/Unbinding Dynamics of Vinculin in Integrin-based Linkages

Here, we describe the state variables and transition kinetics for vinculin in integrin-based linkages. Vinculin reinforces an integrin linkage by binding at its head to Talin (Vcl:Talin bond) and its tail to F-actin (Vcl:F-actin bond), and it reinforces a cadherin linkage by binding at its head to α-Catenin (Vcl:α-Catenin bond) and its tail to F-actin (Vcl:F-actin bond) (44). As such, vinculin provides an additional connection to the F-actin interface when it is bound at both ends.

In both integrin and cadherin linkages, the Vcl:F-actin bond is modeled as a two-state catch-slip bond based on single molecule experiments with T12 vinculin (constitutively active) and F-actin (16). The state variable for the Vcl:F-actin bond in the jth linkage is given by:

$$\theta_j^{Vcl:Factin} = \begin{cases} 0 & Unbound\ State \\ 1 & Weak\ Bound\ State \\ 2 & Strong\ Bound\ State \end{cases} \quad \text{(eq. S18)}$$

In the Vcl:F-actin bond, binding only occurs from the unbound to weak bound state ($\theta_j^{Vcl:Factin}: 0 \rightarrow 1$) with the rate constant $k_{01}^{Vcl:Factin}$, as in a previous model of vinculin with the two-state catch-slip bond (16). Rate constants for unbinding from the weak state ($\theta_j^{Vcl:Factin}: 1 \rightarrow 0$), $k_{10}^{Vcl:Factin}(F)$; unbinding from the strong state ($\theta_j^{Vcl:Factin}: 2 \rightarrow 0$), $k_{20}^{Vcl:Factin}(F)$; and interconversion between the weak and strong states ($\theta_j^{Vcl:Factin}: 1 \rightarrow 2$ and $\theta_j^{Vcl:Factin}: 2 \rightarrow 1$), $k_{12}^{Vcl:Factin}(F)$ and $k_{21}^{Vcl:Factin}(F)$, are defined in Table S2.

In the integrin linkage, the Vcl:Talin bond is modeled as a one state slip bond based on single molecule experiments with vinculin head domain (Vh) and Talin VBS (33). The state variable for the Vcl:Talin bond in the jth linkage is given by:

$$\theta_j^{Vcl:Tal} = \begin{cases} 0 & Unbound\ State \\ 1 & Bound\ State \end{cases} \quad \text{(eq. S19)}$$

In the Vcl:Talin bond, binding ($\theta_j^{Vcl:Tal}: 0 \rightarrow 1$) occurs with the force-independent rate constant $k_{01}^{Vcl:Tal}$ and unbinding ($\theta_j^{Vcl:Tal}: 1 \rightarrow 0$) occurs with the force-dependent rate constant function $k_{10}^{Vcl:Tal}(F)$ defined in Table S2, where F denotes the force across the bond. When bound at both the Vcl:Tal and Vcl:F-actin bonds, vinculin provides an additional connection to the F-actin that is parallel to the Tal:F-actin bond. As such, the linkage can be engaged via bonds though Talin, Vinculin, or both, and all bonds to the F-actin interface must be broken for the linkage to become disengaged. As such, the general expression for the engagement state of the jth linkage becomes:

$$\Theta_j = \begin{cases} 1 & \theta_j^{Intg:FN} > 0 \wedge \left(\theta_j^{Tal:Factin} > 0 \vee \left(\theta_j^{Vcl:Factin} > 0 \wedge \theta_j^{Vcl:Tal} > 0\right)\right) \\ 0 & elsewhere \end{cases} \quad \text{(eq. S20)}$$

where ∧ is the logical operator “and” and ∨ is the logical operator “or”.

In the vinculin-reinforced linkage, the Talin:F-actin and Vcl:F-actin bonds form parallel connections to the same location on F-actin. As such, when forces are transmitted across both vinculin and Talin, they are shared equally between the Talin:F-actin and Vcl:F-actin bonds. We modeled equal load sharing between Talin and Vcl because it is not known how the forces inside the integrin-based linkages are distributed. Together, general expressions for the force across each bond in a linkage are defined below.

$$F_{Link,j}^{Intg:FN} = F_{Link,j} \quad \text{(eq. S21)}$$

$$F_{Link,j}^{Tal:Factin} = \begin{cases} F_{Link,j} & \theta_j^{Tal:Factin} > 0 \ \wedge \left(\theta_j^{Vcl:Factin} = 0 \vee \theta_j^{Vcl:Tal} = 0\right) \\ \dfrac{F_{Link,j}}{2} & \theta_j^{Tal:Factin} > 0 \ \wedge \left(\theta_j^{Vcl:Factin} > 0 \wedge \theta_j^{Vcl:Tal} > 0\right) \\ 0 & \theta_j^{Tal:Factin} = 0 \end{cases} \quad \text{(eq. S22)}$$

$$F_{Link,j}^{Vcl:Factin} = F_{Link,j}^{Vcl:Tal} = \begin{cases} F_{Link,j} & \left(\theta_j^{Vcl:Factin} > 0 \wedge \theta_j^{Vcl:Tal} > 0\right) \ \wedge \theta_j^{Tal:Factin} = 0 \\ \dfrac{F_{Link,j}}{2} & \left(\theta_j^{Vcl:Factin} > 0 \wedge \theta_j^{Vcl:Tal} > 0\right) \ \wedge \theta_j^{Tal:Factin} > 0 \\ 0 & \theta_j^{Vcl:Factin} = 0 \vee \theta_j^{Vcl:Tal} = 0 \end{cases} \quad \text{(eq. S23)}$$

As with the non-reinforced integrin linkage, when all bonds at either interface break, the linkage returns to a disengaged state, in which it experiences no extension and bears no force. If vinculin head unbinds Talin, the linkage is free to recruit another vinculin molecule.

F. Binding/Unbinding Dynamics of Vinculin in Cadherin-based Linkages

Here, we describe the state variables and transition kinetics for vinculin in cadherin-based linkages. Vinculin reinforces a cadherin linkage by binding at its head to α-Catenin (Vcl:α-Catenin bond) and its tail to F-actin (Vcl:F-actin bond) (44). As such, vinculin provides an additional connection to the F-actin interface when it is bound at both ends. The behavior of vinculin in the cadherin linkage is modeled the same as in the integrin linkage, except with different kinetic parameters for the Vcl:α-Catenin bond.

The Vcl:F-actin bond is modeled identical to how it is modeled in the integrin-based linkage, described in the previous Section II-E.

The Vcl:α-Catenin bond is modeled as a one state slip bond based on single molecule experiments with vinculin head domain (Vh) and α-Catenin VBS (33). The state variable for the Vcl:α-Catenin bond in the jth linkage is given by:

$$\theta_j^{Vcl:aCat} = \begin{cases} 0 & Unbound\ State \\ 1 & Bound\ State \end{cases} \quad \text{(eq. S24)}$$

In the Vcl:α-Catenin bond, binding ($\theta_j^{Vcl:aCat}: 0 \rightarrow 1$) occurs with the force-independent rate constant $k_{01}^{Vcl:aCat}$ and unbinding ($\theta_j^{Vcl:aCat}: 1 \rightarrow 0$) occurs with the force-dependent rate constant function $k_{10}^{Vcl:aCat}(F)$ defined in Table S3, where F denotes the force across the bond. Overall, when bound at both the Vcl:α-Catenin and Vcl:F-actin bonds, vinculin provides an additional connection to the F-actin that is parallel to the α-Catenin:F-actin bond. As such, the linkage can be engaged via bonds though α-Catenin, Vinculin, or both, and all bonds to the F-actin interface must be broken for the linkage to become disengaged. As such, the general expression for the engagement state of the jth linkage becomes:

$$\Theta_j = \begin{cases} 1 & \theta_j^{Cad:Cad} > 0 \wedge \left(\theta_j^{aCat:Factin} > 0 \vee \left(\theta_j^{Vcl:Factin} > 0 \wedge \theta_j^{Vcl:aCat} > 0\right)\right) \\ 0 & elsewhere \end{cases} \quad \text{(eq. S25)}$$

where ∧ is the logical operator “and” and ∨ is the logical operator “or”.

In the vinculin-reinforced linkage, the α-Catenin:F-actin and Vcl:F-actin bonds form parallel connections to the same location on F-actin. As such, when forces are transmitted across both vinculin and α-Catenin, they are shared equally between the α-Catenin:F-actin and Vcl:F-actin bonds. We modeled equal load sharing between α-Catenin and Vcl because it is not known how the forces inside the cadherin-based linkages are distributed. Together, general expressions for the force across each bond in a linkage are defined below.

$$F_{Link,j}^{Cad:Cad} = F_{Link,j} \quad \text{(eq. S26)}$$

$$F_{Link,j}^{aCat:Factin} = \begin{cases} F_{Link,j} & \theta_j^{aCat:Factin} > 0 \ \wedge \left(\theta_j^{Vcl:Factin} = 0 \vee \theta_j^{Vcl:aCat} = 0\right) \\ \dfrac{F_{Link,j}}{2} & \theta_j^{aCat:Factin} > 0 \ \wedge \left(\theta_j^{Vcl:Factin} > 0 \wedge \theta_j^{Vcl:aCat} > 0\right) \\ 0 & \theta_j^{aCat:Factin} = 0 \end{cases} \quad \text{(eq. S27)}$$

$$F_{Link,j}^{Vcl:Factin} = F_{Link,j}^{Vcl:aCat} = \begin{cases} F_{Link,j} & \left(\theta_j^{Vcl:Factin} > 0 \wedge \theta_j^{Vcl:aCat} > 0\right) \wedge \theta_j^{aCat:Factin} = 0 \\ \dfrac{F_{Link,j}}{2} & \left(\theta_j^{Vcl:Factin} > 0 \wedge \theta_j^{Vcl:aCat} > 0\right) \wedge \theta_j^{aCat:Factin} > 0 \\ 0 & \theta_j^{Vcl:Factin} = 0 \vee \theta_j^{Vcl:aCat} = 0 \end{cases} \quad \text{(eq. S28)}$$

As with the non-reinforced cadherin-catenin linkage, when all bonds at either interface break, the linkage returns to a disengaged state, in which it experiences no extension and bears no force. If vinculin head unbinds α-Catenin, the linkage is free to recruit another vinculin molecule. As the effective stiffnesses of multi-component integrin- and cadherin-based linkages are not known, we assumed that integrin- and cadherin-based linkages have a constant spring constant, K_{Link}, independent of linkage state. As such, incorporation of vinculin into integrin- or cadherin-based molecular linkages does not alter the spring constant of the linkage.

G. Ensemble Vinculin Molecular Tension

To facilitate comparisons to experimental measurements with the vinculin molecular tension sensor (VinTS), we measured in simulations the ensemble vinculin molecular tension, $\langle F_{Vcl} \rangle_{Links}$, defined as the average of tension across the vinculin molecules in all linkages:

$$\langle F_{Vcl} \rangle_{Links} = \frac{1}{N_{Link}} \sum_{i=1}^{N_{Link}} F_{Link,i}^{Vcl} \quad \text{(eq. S29)}$$

where the force across the vinculin molecule in the jth linkage is equal to the force across the Vcl:Factin bond, $F_{Link,j}^{Vcl} = F_{Link,j}^{Vcl:Factin}$. Note that this is also the same as the force across the Vcl:Talin ($F_{Link,j}^{Vcl:Factin} = F_{Link,j}^{Vcl:Tal}$) or Vcl: α-Catenin bond ($F_{Link,j}^{Vcl:Factin} = F_{Link,j}^{Vcl:aCat}$) as previously described. As vinculin is able to bind actin and bear loads in reinforced but not non-reinforced

linkages, the ensemble vinculin molecular tension is approximately $\langle F_{Vcl}\rangle_{Links} \approx \rho_{Vcl} \cdot \langle F_{Vcl}\rangle_{Reinforced\ Links} + (1-\rho_{Vcl}) \cdot 0$.

H. Simulation Algorithm

Simulations were run using MATLAB (Mathworks) R2019b. Stochastic simulations of the FA and AJ clutch models were carried out using the Gillespie Stochastic Simulation Algorithm as previously described for motor clutch models (22, 47). It was verified that results with this simulation algorithm matched those obtained using a discrete time-step algorithm with a small time-step (0.0005 s). The simulations were started with all linkage bonds in the unbound state and initial connections were allowed to form subject to the binding rate constants listed in Table S1. Simulations were run for a duration of 1000s. Outputs (such as total force and engaged linkage fraction) were computed as time-averages over a time window after reaching steady-state. To compute mean engagement lifetime and fraction of disengagement events due to unbinding at certain interfaces, all linkage state transitions after reaching steady state were recorded and analyzed. Single linkage simulations were conducted at constant loading rates using a discrete time-step algorithm with a time-step of 0.0001 sec. Similar analyses to those described for the FA and AJ clutch models were conducted on these simulations.

I. Single Component Friction Clutch Configuration for Validation of Model Implementation

Implementation of the friction clutch models was validated by comparing simulations to analytical expressions of the friction force-velocity relationship for simple linkages with ideal or slip bonds derived by Sens (7). To conduct these simulations, linkages were set to bind/unbind at only one interface according to an ideal, $k_{off}(F) = k_{off}$, or Bell slip bond, $k_{off}(F) = k_{off,0}e^{F/F_b}$. Other parameters for the validation simulations were set to match the base parameters for the FA and AJ friction clutch models (N_{link}=50, K_{link}= 5 pN/nm, k_{on}=2/s) and the same range of velocities was also used (v =[0.1,100] nm/s). Simulations were conducted in the limit of an infinitely rigid external spring ($K_{Ext} \gg N_{link}K_{link}$), where the following analytical expressions apply. The force-velocity relationship for the case of an ideal bond, $k_{off}(F) = k_{off}$, from Sens (7) is:

$$\langle F\rangle = \left[\frac{N_{link}K_{link}k_{on}}{(k_{on}+k_{off})k_{off}}\right]v \qquad \text{(eq. S30)}$$

The force-velocity relation for the case of a Bell slip bond, $k_{off}(F) = k_{off,0}e^{F/F_b}$, from Sens (7) is:

$$\langle F\rangle = \frac{N_{link}F_b\left(\frac{k_{on}}{k_{off,0}}\right)e^{\frac{v_\beta}{v}}\int_0^\infty fe^{-e^{\frac{fv_\beta}{v}}}df}{\frac{v}{v_\beta}+\left(\frac{k_{on}}{k_{off,0}}\right)e^{\frac{v_\beta}{v}}\int_{\frac{v_\beta}{v}}^\infty \frac{e^{-f}}{f}df}, \qquad v_\beta = \frac{k_{off,0}F_b}{K_{link}} \qquad \text{(eq. S31)}$$

Lastly, as integrin- and cadherin-based adhesions are known to contain multiple proteins with catch-slip bonds (16, 18, 19, 21), we also considered a two-pathway catch-slip bond, $k_{off}(F) = k_{off,0}\left(0.9e^{-2F/F_b} + 0.1e^{F/F_b}\right)$, in the single component friction clutch as a tool to build intuition.

J. Determination of External Spring Constant for given Effective Young's Modulus

In clutch models, an external spring is used to represent the stiffness of the external material to which the molecular linkages are connected (18, 22-24). For the FA model, this corresponds to the substrate stiffness. For the AJ model, this corresponds to the stiffness of the adjacent cell in the monolayer (or alternatively, in the context of experiments measuring traction forces on cadherin-coated elastic substrates, this would correspond to the substrate stiffness). To relate the external spring constant, K_{ext} [pN/nm], to an equivalent Young's modulus, E_{eff} [kPa], we used a relationship from previous motor-clutch models, $E_{eff} = \frac{9K_{Ext}}{4\pi a}$, where a is the radius of an equivalent circular adhesion (24, 48). For the AJ model, the adhesion radius was estimated using the circular adhesion area corresponding to the base number of linkages ($N_{Link} = 50$) at the

reported density of cadherin molecules in cadherin clusters (29) (2666/μm^2), corresponding to adhesion radius of 77 nm. This yielded a conversion factor E_{eff}/K_{ext} of 9.27 kPa/(pN/nm). For the AJ model, we used this conversion factor to approximate the external spring constant from experimental estimates of the elastic modulus of cell monolayers (31, 32) (~20-33 kPa is equivalent to ~2.16-3.56 pN/nm). For the FA model, the external spring constant was set arbitrarily high to represent experimental conditions from this paper (stiffness of glass), and therefore no conversion factor was needed for the FA model.

K. Plots of Mean Bond Lifetime versus Force

To overlay unbinding rate constant models on mean bond lifetime versus force plots (Fig. S14c,f), mean lifetimes were obtained from the force-dependent rate constant models as follows. For single bound state models, where there is a single unbinding transition, the lifetime at force F was taken to be the inverse of the rate constant at force F. For two bound state catch bond models, where there are unbinding transitions from weak and strong states, as well as interconversion between them, the mean lifetime was obtained by assuming an initial distribution of bound states based on equilibrium under no force, as previously done for this type of bond (21). Then, the mean lifetime was solved for using a continuous time Markov chain to calculate the mean exit times from each bound state and then weighting them according to the starting distribution for the two bound states.

L. Two-sided AJ Friction Clutch

The one-sided AJ friction clutch implemented in this work considers the frictional force resisting the relative cell-cell motion resulting from the extension of elastic molecular linkages that link the actin cytoskeleton of one cell to the cadherins on the surface of the adjacent cell. This simple model incorporates the loading source (relative cell-cell motion) and the major components and binding interfaces of cadherin-based linkages (cadherin and actin interfaces). Because at AJs there are linkages to the actin cytoskeleton inside both cells, we assessed the validity of the simplified one-sided AJ friction clutch by implementing a two-sided AJ friction clutch that explicitly models the full linkage between the actin cytoskeleton of one cell through the cadherin:cadherin bond to the actin cytoskeleton of the adjacent cell. For reference, the one-sided AJ friction clutch treats the transmission of forces across molecular linkages between the cadherins on the surface of cell 2 and the actin cytoskeleton in cell 1, i.e. the non-reinforced linkage is cadherin:cadherin-catenin:Factin. We implemented a two-sided AJ friction clutch that explicitly models the transmission of forces across complete molecular linkages between the actin cytoskeleton in Cell 2 through the cadherin:cadherin interface and to the actin cytoskeleton in Cell 1, i.e. the non-reinforced linkage is now Factin:catenin-cadherin:cadherin-catenin: Factin. In this case, the linkage must be bound at both F-actin interfaces and the Cadherin interface to be engaged and transmit forces. In both models the linkages are loaded by the relative motion between the cells, defined as a speed V in the reference frame of Cell 2, which is also equivalent to velocities of $V/2$ for Cell 1 and $-V/2$ for Cell 2 in the lab reference frame. Additionally, as the two external springs representing the stiffness of the cells outside the linkages (K_{ext}) are in series, they were implemented as a single spring with an effective spring constant of $K_{ext}/2$. Likewise, the stiffness of the two-sided linkage was modeled with an effective spring constant of $K_{link}/2$.

III. RESULTS

A. Friction Clutch with Single-Component Linkage: Technical validation of model implementation and comparison of individual linkage dynamics to total friction.

To validate implementation of the friction clutch model and to gain intuition about molecular determinants of friction, we used the previously developed friction clutch model that contained simple linkages with a single bond (7) (Fig. S15a and Section II-I). The single bond was modeled as an ideal bond, Bell model slip bond, or two pathway catch-slip bond (Fig. S15b-c).

To validate our implementation of the friction clutch model, we simulated clutches comprised of linkages with ideal or slip bonds and compared them to previously determined

analytical expressions relating average total friction force to speed (from Sens (7) and given in Equations S30 and S31). For the ideal bond, the friction force increased linearly with speed, and the simulation results for two different values of the unbinding rate constant both showed good agreement with the previously obtained analytical relationship from Sens (7) (Fig. S15d). For the slip bond, the friction force first increased then decreased with speed, and the simulation results for three different combinations of unbinding rate parameters all showed good agreement with the analytical relationship from Sens (7) (Fig. S15g). Taken together, these simulations validated our implementation of the friction clutch model.

We next sought to gain intuition about molecular determinants of friction. To do so, we compared individual linkage dynamics in the clutch, using mean engagement lifetime, to the effective friction coefficient (F/V), a standard parameter describing the frictional resistance between sliding surfaces (cell-ECM or cell-cell) in models of CCM (1). For the ideal bond, the engagement lifetime (Fig. S15e) and effective friction coefficient (Fig. S15f) were both independent of speed. For the slip bond, both the engagement lifetime (Fig. S15h) and effective friction coefficient (Fig. S15i) were speed-dependent, decreasing monotonically with speed. As integrin- and cadherin-based adhesions are known to contain multiple proteins with catch-slip bonds, we also investigated a catch-slip bond. For the catch-slip bond, both the engagement lifetime (Fig. S15k) and effective friction coefficient (Fig. S15l) were again speed-dependent, but this time increasing up to an intermediate speed then decreasing at higher speeds. Therefore, for each bond type, the qualitative shape of the effective friction coefficient-speed curve relates to the dynamics of individual linkages, meaning the underlying force-sensitive dynamics are indicative of the larger-scale mechanics of the friction clutch.

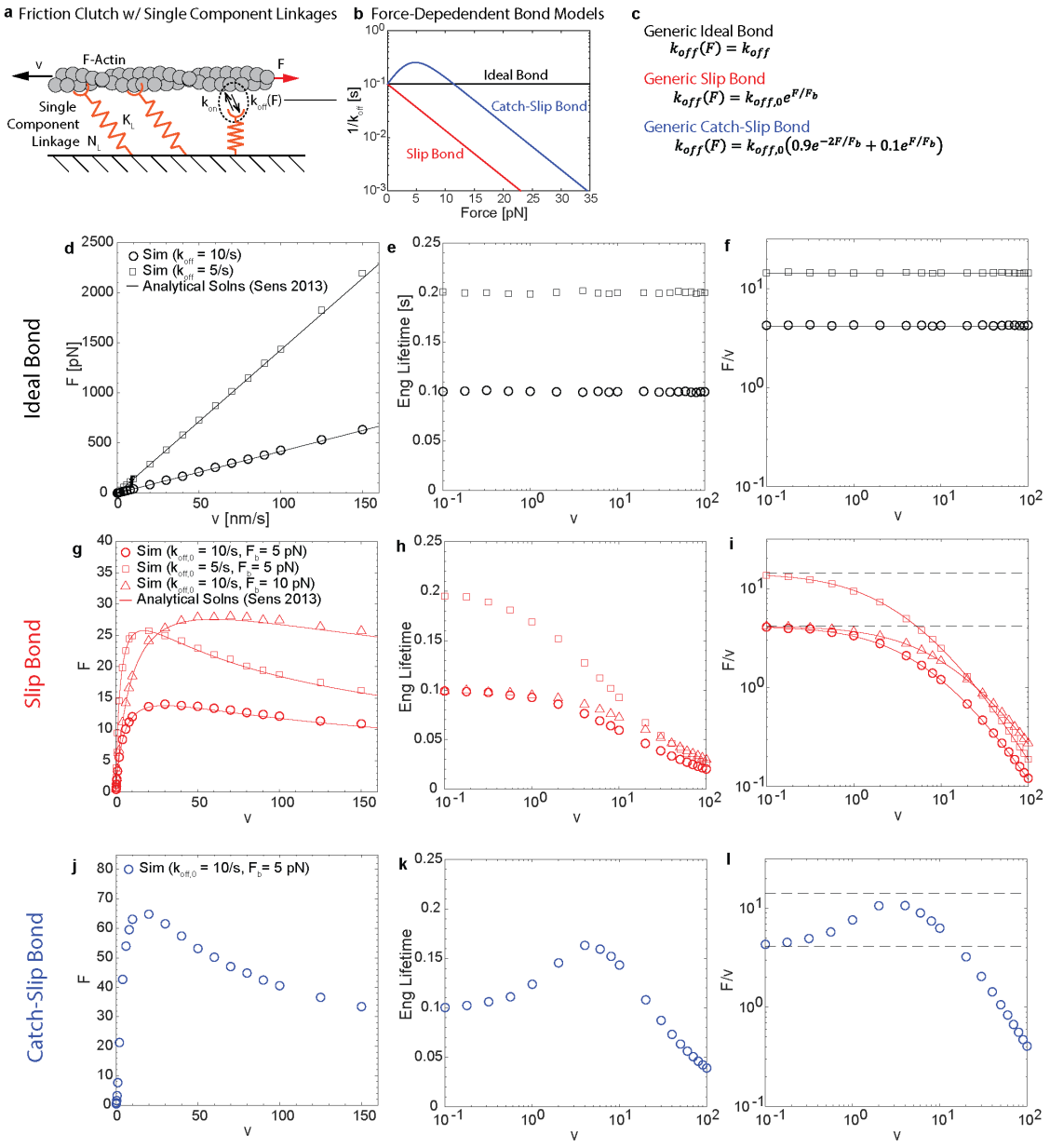

Fig. S15. Validation of Friction Clutch Model with Single Component Linkages. (a) Schematic of friction clutch model with single component linkages containing a single binding/unbinding interface. (b) Plot of mean bond lifetime versus force for three generic bond models used for the unbinding rate constant for single component linkages. (c) Unbinding rate constant functions for the three generic bond models used for single component linkages. (d-f) Plots of mean friction force, mean linkage engagement lifetime, and mean effective friction coefficient (F/V) for friction clutches containing single component linkages with ideal bonds, for the two different unbinding rate constants indicated. (g-i) Same for friction clutches containing single component linkages with a slip bond, for the three different unbinding rate constant parameter combinations indicated. (j-l) Same for friction clutch containing single component linkages with a catch-slip bond, for indicated unbinding rate constant parameters. For (d-l), data points are time averages from simulations and solid lines are analytical solutions (Equation S30 for ideal bond case and Equation S31 for slip bond case) from Sens 2013. Dashed lines in (i) and (l) are guides for the eye from (f).

B. Force sensitivity of multi-component integrin- and cadherin-based linkages.

The molecular linkages that mediate mechanical connections in the FA/AJ between the actin cytoskeleton and the ECM/adjacent cell are composed of multiple proteins and therefore multiple dynamic interfaces (8). As the single bond linkages used in the previous friction clutch model (Section III-A) do not capture the complex connectivity and potential regulation of these biological linkages, we developed multi-component linkages to use in the friction clutch models. These multi-component linkages consisted of integrin:talin:F-actin in FAs (Fig. S14b) or E-cadherin:β-catenin:α-catenin:F-actin in AJs (Fig. S14e), which could be reinforced through the incorporation of vinculin, and whose ability to bear force depended on the force-dependent lifetimes of bonds in the integrin-based (Fig. S14c, Section II-B/E, and Table S2) or cadherin-based (Fig. S14f, Section II-C/F, and Table S3) linkages.

To transmit forces, molecular linkages must be bound at both sides (F-actin and external interfaces in our model). We note that the lifetimes of the Intg:FN (18) and Talin:F-actin (19) bonds (Fig. S14c), as well as those of the E-cad:E-cad (20) and α-catenin:F-actin (21) bonds (Fig. S14f), are within an order of magnitude of each other over a wide range of physiological molecular loads. This suggests that the force-sensitive dynamics of these linkages are not dominated by a single bond but rather determined by the combined behavior of multiple interfaces. Also, there are force regimes in both linkages over which the primary bond to the actin interface (Talin:F-actin or α-catenin:F-actin) has a shorter lifetime than bonds to the external interface, suggesting that reinforcement of the actin interface with a parallel bond, such as the Vcl:F-actin bond (16), could modulate the combined dynamics of the linkage.

As parameters for force-sensitive bond dynamics were obtained from single molecule experiments characterizing the interfaces separately, we first assessed their suitability for use in combination to model multi-component linkages at the FA and AJ. To do so, we subjected single linkages to a range of fixed loading rates (Fig. S16a). This range corresponded to estimated protein loading rates inside cells, using typical protein stiffnesses (26) (~1-10 pN/nm) and speeds of either actin flow (26) (~2-600 nm/s) or cell migration in monolayers (25) (~1-30 μm/hr or ~0.28-8.33 nm/s). We quantified the linkage engagement lifetime, which is defined as the mean duration of time over which linkages remain engaged and support force transmission. In the integrin-based linkage, the engagement lifetime was strongly biphasic, first increasing then decreasing with loading rate, regardless of vinculin reinforcement (Fig. S16b-c). This is consistent with the combined linkage having a strong catch-slip behavior. Vinculin reinforcement did not alter the functional form of the lifetime-load rate curve, but substantially increased the engagement lifetime across a wide range of low and intermediate loading rates (up to ~56 pN/s). This is consistent with the established role of vinculin as a mechanical reinforcement element at the FA (9, 49). In the cadherin-based linkage, the engagement lifetime remained constant or increased slightly with loading rate, before decreasing strongly at higher loading rates (Fig. S16d-e). This is consistent with the combined linkage having an ideal-slip or weak catch-slip behavior. Vinculin reinforcement did not alter the functional form of the lifetime-load rate curve, but substantially increased the engagement lifetime across a wide range of low and intermediate loading rates (up to ~100 pN/s). This is consistent with the established role of vinculin as a mechanical reinforcement element at the AJ (12, 14). We also note that, as suspected, the behavior of the multi-component linkages is not readily predictable from the force-sensitive dynamics of single bonds in the linkages, indicating that their force-sensitivity and regulation depend on the combined behavior of multiple dynamic interfaces.

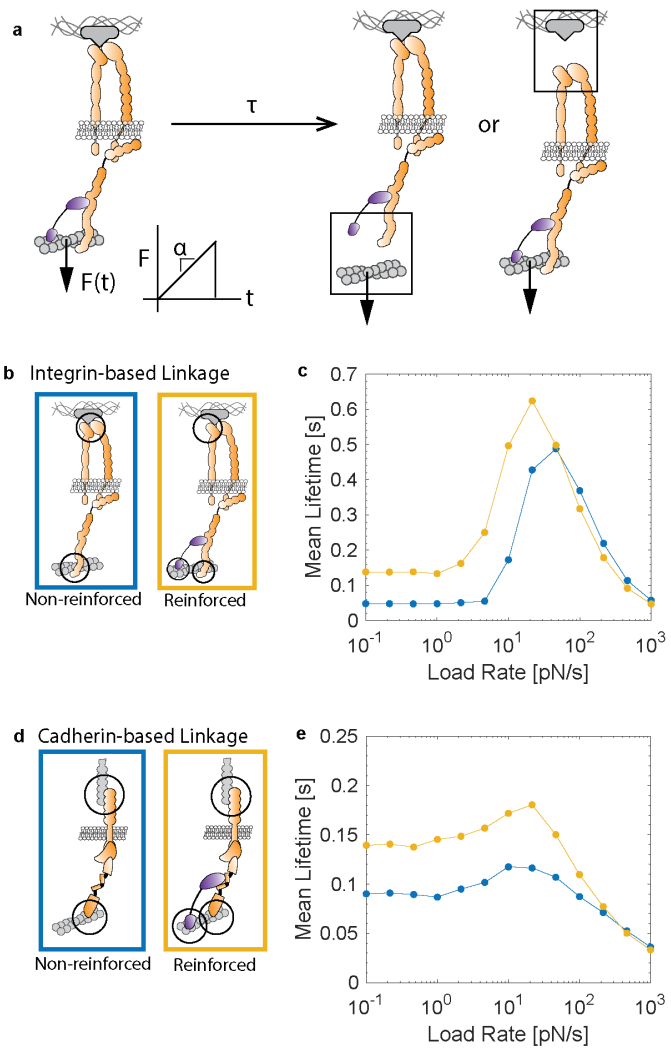

Fig. S16 Characterization of multi-component Integrin- and Cadherin Linkages. (a) Schematic of single integrin-based linkage subjected to fixed rate loading leading to its disengagement once all bonds at either the external or actin interface are broken. (b-c) Plot of mean engagement lifetime versus load rate for integrin-based linkage without and with vinculin reinforcement. (d-e) Same for cadherin-based linkage without and with vinculin reinforcement.

C. FA Friction Clutch and Effect of Vinculin Reinforcement.

We next sought to assess regulators of cell-ECM friction mediated by the FA. To do so, we incorporated multi-component integrin-based linkages into the friction clutch model and assessed the effect of increasing the fraction of linkages with loadable vinculin (Fig. S17). Time-traces for the number of engaged linkages and total force exhibit fluctuations (Fig. S17c-f), consistent with the behavior of previous friction clutch models (7). In the absence of vinculin reinforcement ($\rho_{Vcl} = 0$), the mean linkage engagement lifetime (Fig. S17g; repeated from main text for convenience) and mean linkage engagement fraction (Fig. S17h) had strongly biphasic relationships with speed, first increasing then decreasing. This was consistent with the strong catch-slip behavior of single integrin-based linkages (Section III-B). Furthermore, the effective friction coefficient (F/V) (Fig. S17j; repeated from main text for convenience) exhibited a similar biphasic relationship with speed. Therefore, as observed for friction clutch models with a single bond (Section III-A), the force-sensitive dynamics of the multi-component integrin-based linkage was predictive of the shape of the friction coefficient-speed relationship.

We next assessed the effect of vinculin mechanical reinforcement on the FA friction clutch by increasing the fraction of linkages with loadable vinculin (ρ_{Vcl}). Increasing the fraction of loadable vinculin substantially increased the mean linkage engagement lifetime (Fig. S17g; repeated from main text for convenience) and mean linkage engagement fraction (Fig. S17h) over the range of speeds corresponding to monolayer velocities observed in this work and elsewhere (25) (~1-30 μm/hr or ~0.28-8.33 nm/s). This was consistent with vinculin's effect on the dynamics of single integrin-based linkages being more pronounced at low and intermediate loading rates (Section III-B). As a result, vinculin reinforcement also significantly increased the friction force (Fig. S17i) and effective friction coefficient (Fig. S17j; repeated from main text for convenience) across the range speeds corresponding to CCM in our system. At higher speeds, the friction coefficient strongly decreased with speed regardless of vinculin reinforcement, and vinculin reinforcement did not alter the functional forms of the engagement lifetime-speed or friction coefficient-speed relationships. Time-traces contain a significant number of Vcl:F-actin bonds in the strong bound state (Fig. S17e-f), indicating engagement of vinculin's catch bond in the FA model.

To further assess the ability of the vinculin regulatory switch to tune friction, we assessed the effect of finer variations in the fraction of loadable vinculin at an intermediate speed (10 μm/hr) in the CCM range (Fig. S17k; repeated from main text for convenience). The friction coefficient varied approximately linearly with the fraction of loadable vinculin and had a maximum effect of ~2-fold increase in the effective friction coefficient. To facilitate comparisons to experimental measurements with FRET-based vinculin MTS (VinTS), we also assessed ensemble vinculin molecular tension, $\langle F_{Vcl} \rangle_{Links}$. Ensemble vinculin molecular tension increased approximately linearly with the amount of loadable vinculin, meaning ensemble vinculin tension co-varied with the friction coefficient.

Overall, analysis of the FA friction clutch model demonstrates the relationship between dynamics of multi-component integrin linkages and subcellular friction at the FA and suggests that vinculin reinforcement increases cell-substrate friction in a tunable manner across a range of speeds corresponding to CCM.

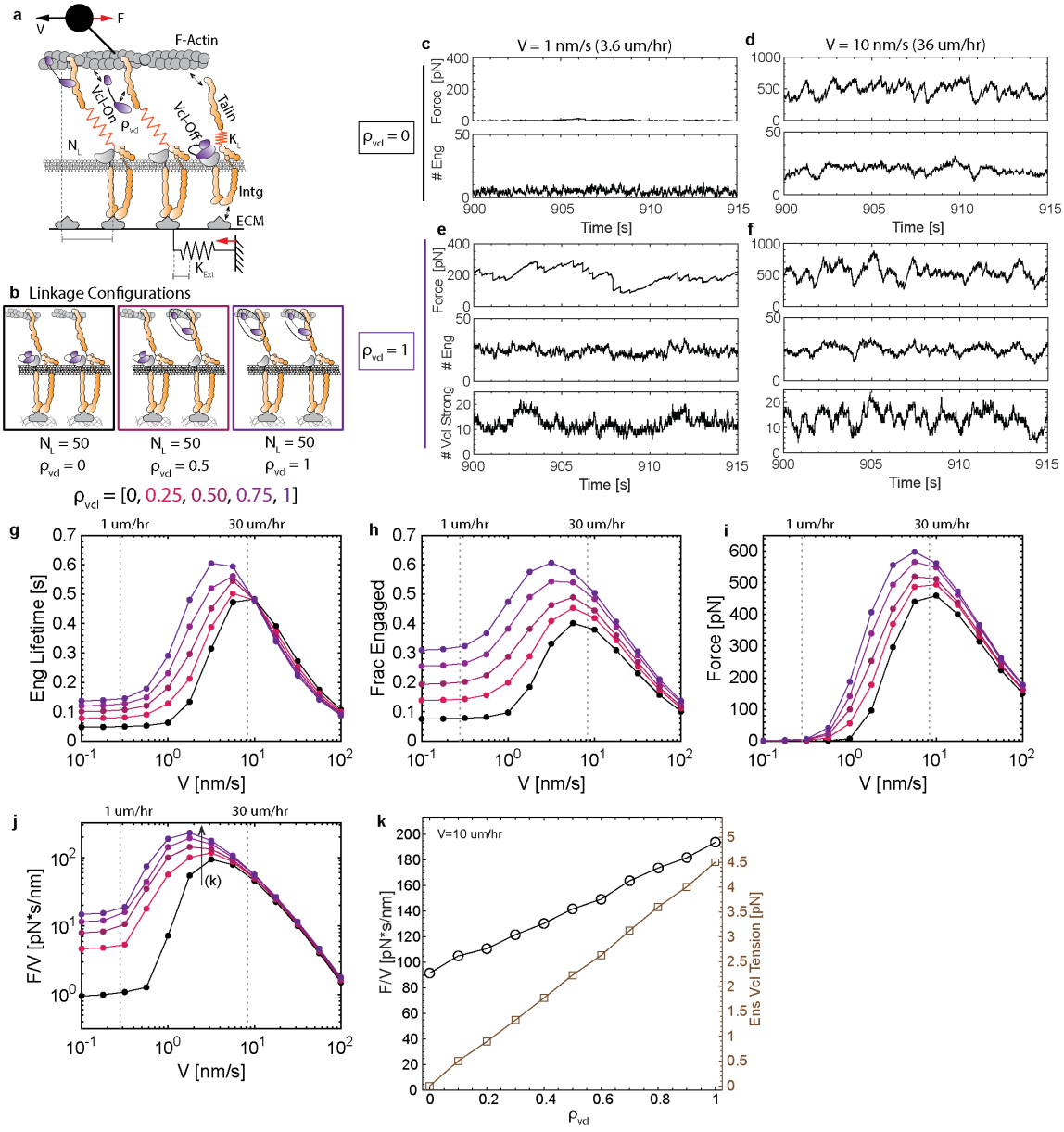

Fig. S17 FA Friction Clutch Model. (a) Schematic of FA friction clutch model. (b) Schematic of linkage configurations for different values of $\boldsymbol{\rho_{Vcl}}$, the fraction of linkages with loadable vinculin. (c-d) Time-traces of total friction force and number of engaged linkages for simulations with $\boldsymbol{\rho_{Vcl} = 0}$ and speed (V) 1 nm/s or 10 nm/s. (e-f) Time-traces of total friction force, number of engaged linkages, and number of linkages with the Vcl:F-actin bond in the strong bound state for simulations with $\boldsymbol{\rho_{Vcl} = 1}$ and speed (V) 1 nm/s or 10 nm/s. (g-j) Plots of mean linkage engagement lifetime, mean fraction of linkages engaged, mean total friction force, and mean effective friction coefficient (F/V) for 5 values of $\boldsymbol{\rho_{Vcl}}$. (k) Plot of effective friction coefficient (left y axis) and ensemble vinculin molecular tension (right y axis) versus $\boldsymbol{\rho_{Vcl}}$ for speed (V) 10 μm/hr. (g), (j), and (k) appear in the main text and are repeated here for convenience.

D. AJ Friction Clutch and Effect of Vinculin Reinforcement

We next sought to assess regulators of cell-cell friction mediated by the AJ. To do so, we incorporated multi-component cadherin-based linkages into the friction clutch model and assessed the effect of increasing the fraction of linkages with loadable vinculin (Fig. S18). Time-traces for the number of engaged linkages and total force exhibit fluctuations (Fig. S18c-f), consistent with the behavior of previous friction clutch models (7). In the absence of vinculin reinforcement ($\rho_{Vcl} = 0$), the mean linkage engagement lifetime (Fig. S18g; repeated from main text for convenience) and mean linkage engagement fraction (Fig. S18h) had weak biphasic relationships with speed, increasing slightly or remaining constant at lower speeds and then decreasing at higher speeds. This was consistent with the weak catch-slip or ideal-slip behavior of single cadherin-based linkages (Section III-B). Furthermore, the effective friction coefficient (F/V) (Fig. S18j; repeated from main text for convenience) exhibited a similar relationship with speed. Therefore, as observed for friction clutch models with a single bond (Section III-A), the force-sensitive dynamics of the multi-component cadherin-based linkage was predictive of the shape of the friction coefficient-speed relationship.

We next assessed the effect of vinculin mechanical reinforcement on the AJ friction clutch by increasing the fraction of linkages with loadable vinculin (ρ_{Vcl}). Increasing the fraction of loadable vinculin substantially increased the mean linkage engagement lifetime (Fig. S18g; repeated from main text for convenience) and mean linkage engagement fraction (Fig. S18h) over the range of relative cell-cell speeds corresponding to monolayer velocities observed in this work and elsewhere (25) (~1-30 μm/hr or ~0.28-8.33 nm/s). This was consistent with vinculin's effect on the dynamics of single cadherin-based linkages being more pronounced at low and intermediate loading rates (Section III-B). As a result, vinculin reinforcement also significantly increased the friction force (Fig. S18i) and effective friction coefficient (Fig. S18j; repeated from main text for convenience) across the range speeds corresponding to CCM in our system. At higher speeds, the friction coefficient strongly decreased with speed regardless of vinculin reinforcement, and vinculin reinforcement did not alter the functional forms of the engagement lifetime-speed or friction coefficient-speed relationships. Time-traces contain significant numbers of α-catenin:F-actin bonds and Vcl:F-actin bonds in the strong bound state (Fig. S18e-f), indicating engagement of both the α-catenin and vinculin catch bonds in the AJ model.

To further assess the ability of the vinculin regulatory switch to tune friction, we assessed the effect of finer variations in the fraction of loadable vinculin at an intermediate speed (10 μm/hr) in the CCM range (Fig. S18k; repeated from main text for convenience). The friction coefficient varied approximately linearly with the fraction of loadable vinculin and had a maximum effect of ~4-fold increase in the effective friction coefficient. To facilitate comparisons to experimental measurements with FRET-based vinculin MTS (VinTS), we also assessed ensemble vinculin molecular tension, $\langle F_{Vcl} \rangle_{Links}$. Ensemble vinculin molecular tension increased approximately linearly with the amount of loadable vinculin, meaning ensemble vinculin tension co-varied with the friction coefficient.

Together, analysis of the AJ friction clutch model demonstrates the relationship between dynamics of multi-component cadherin linkages and subcellular friction at the AJ and suggests that vinculin reinforcement increases cell-cell friction in a tunable manner across a range of speeds corresponding to CCM. Compared to the FA model, the effect of vinculin reinforcement on the friction coefficient was overall higher in AJs (~4-fold increase) than in FAs (~2-fold increase).

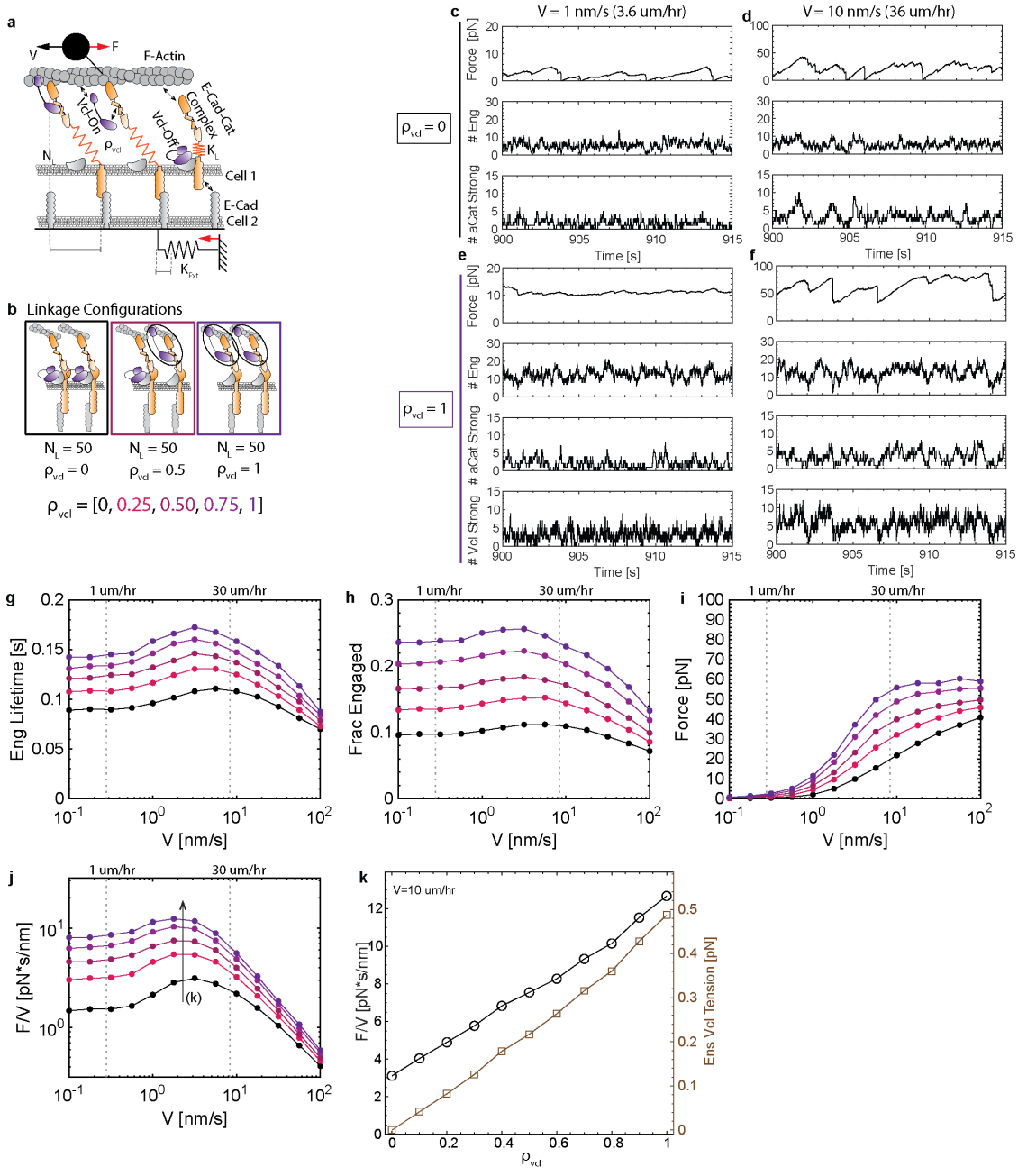

Fig. S18 AJ Friction Clutch Model. (a) Schematic of AJ friction clutch model. (b) Schematic of linkage configurations for different values of $\boldsymbol{\rho_{Vcl}}$, the fraction of linkages with loadable vinculin. (c-d) Time-traces of total friction force, number of engaged linkages, and number of linkages with the α-catenin:F-actin bond in the strong bound state for simulations with $\boldsymbol{\rho_{Vcl} = 0}$ and speed (V) 1 nm/s or 10 nm/s. (e-f) Time-traces of total friction force, number of engaged linkages, and number of linkages with the α-catenin:F-actin and Vcl:F-actin bonds in the strong bound state for simulations with $\boldsymbol{\rho_{Vcl} = 1}$ and speed (V) 1 nm/s or 10 nm/s. (g-j) Plots of mean linkage engagement lifetime, mean fraction of linkages engaged, mean total friction force, and mean effective friction coefficient (F/V) for 5 values of $\boldsymbol{\rho_{Vcl}}$. (k) Plot of effective friction coefficient (left y axis) and ensemble vinculin molecular tension (right y axis) versus $\boldsymbol{\rho_{Vcl}}$ for speed (V) 10 μm/hr. (g), (j), and (k) appear in the main text and are repeated here for convenience.

E. Robustness of vinculin-based reinforcement as a mechanism to tune friction at FA and AJ.

We next assessed the effectiveness of the vinculin-based reinforcement mechanism across a wide parameter space in the FA and AJ friction clutch models. To do so, we varied parameters separately across a range of two orders of magnitude centered on the base value and analyzed the total friction force with no ($\rho_{vcl} = 0$) or full ($\rho_{vcl} = 1$) vinculin reinforcement (Fig. S19). To make this comparison, we computed the relative change in mean total friction force between no vinculin reinforcement ($F_{\rho_{vcl}=0}$) and full vinculin reinforcement ($F_{\rho_{vcl}=1}$), given by $R = \left(F_{\rho_{vcl}=1} - F_{\rho_{vcl}=0}\right)/F_{\rho_{vcl}=0}$. A value of $R = 0$ means that vinculin reinforcement has no effect on total friction, $R = 1$ means that vinculin reinforcement results in a 100% increase in total friction, and $R = -1$ means that vinculin reinforcement results in a 100% reduction in total friction. While the magnitude of vinculin's effect increased or decreased in response to changes in some of the parameters, across the 40 parameter combinations tested we found that the vinculin reinforcement resulted in at least a 20% increase ($R > 0.2$) in friction force for 36/40 parameter combinations at the FA (Fig. S19a) and 40/40 parameter combinations at the AJ(Fig. S19b), with ~100% ($R \sim 1$) or greater increases for many parameter combinations in the FA model and ~300% ($R \sim 3$) or greater increases for many parameter combinations in the AJ model. We also note that a reduction in friction due to vinculin reinforcement was never observed. Overall, this indicated the general robustness of vinculin-based reinforcement as a mechanism for turning friction at the FA and AJ.

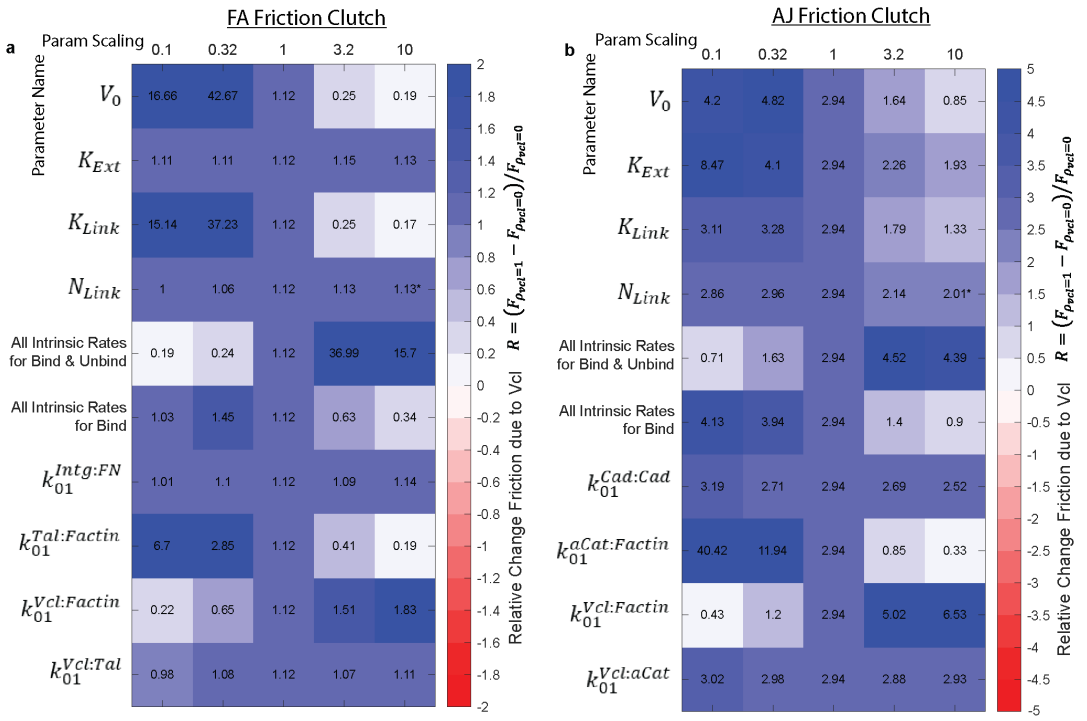

Fig. S19 Robustness of Vinculin-based Reinforcement Mechanism. Parameters in the (a) FA or (b) AJ clutch models were varied separately over two orders of magnitude centered on the base value (0.1x, 0.32x, 1x, 3.2x, and 10x the base values reported in Table S1) to assess the effect of loaded vinculin on friction. For each parameter value, the text and color indicate the relative change in mean total friction force between no vinculin reinforcement ($\boldsymbol{F_{\rho_{vcl}=0}}$) and full vinculin reinforcement ($\boldsymbol{F_{\rho_{vcl}=1}}$), given by $\boldsymbol{R = \left(F_{\rho_{vcl}=1} - F_{\rho_{vcl}=0}\right)/F_{\rho_{vcl}=0}}$. $\boldsymbol{R = 0}$ means vinculin reinforcement has no effect on total friction, $\boldsymbol{R = 1}$ means vinculin reinforcement increases total friction by 100%, and $\boldsymbol{R = -1}$ means vinculin reinforcement decreases total friction by 100%. Note that the parameter labels “All intrinsic rates for bind “ or “All intrinsic rates for bind and unbind” indicate that all intrinsic rate constants for binding, or binding and unbinding, respectively, were scaled for all bonds at the same time. All other labels correspond directly to single parameters in Table S1. The (*) indicates that for linkage number only, the highest parameter value was set to 5x instead of 10x the base value.

F. Effect of Vcl-based Reinforcement is Driven by the Force-Sensitivity of Vinculin's F-actin Bond.

The ability of vinculin to increase friction across a range of speeds relevant to CCM was related to increases in the engagement lifetime of linkages. This indicated the role of the Vcl:F-actin bond in stabilizing the actin interface and implicated the force-sensitive unbinding of vinculin from F-actin as an important model parameter. However, as vinculin is an adapter protein that binds F-actin in parallel to the α-catenin:F-actin or Talin:F-actin bonds, stabilization could also arise simply by changes in the effective on- and off-rates for two bonds in parallel or synergistic effects due to load sharing between bonds in parallel.

We therefore sought to specifically test the role of the force-sensitive Vcl:F-actin bond. To do so, we implemented a third linkage configuration, in which binding to the actin interface occurs exclusively via the Vcl:F-actin bond (called "Vcl Only Configuration" Fig. S20 red lines). We compared simulations with this linkage configuration to those in which linkages bind to the actin interface via both Vcl:F-actin and α-catenin:F-actin or Talin:F-actin ("Reinforced Configuration", Fig. S20 purple lines) or only α-catenin:F-actin or Talin:F-actin ("Non-Reinforced Configuration, Fig. S20 black lines) (Fig. S20a-b for AJ, Fig. S20e-f for FA). In the AJ model, simulations with the Vcl Only Configuration had similar engagement lifetimes (Fig. S20c) and effective friction coefficients (Fig. S20d) across CCM speeds compared to the Reinforced Configuration, indicating that vinculin's F-actin bond is the main driver of its effect in the model. In fact, the Vcl Only Configuration exhibited a slightly higher engagement lifetime compared to the Reinforced Configuration, indicating enhanced lifetime of the Vcl:Factin catch bond in the absence of partial load distribution to the α-catenin:F-actin bond. The effective friction coefficient, on the other hand, is slightly higher for the Reinforced Linkage, indicating a small secondary contribution due to an increase in the effective on-rate for two parallel bonds. Overall, as the binding rate constants for α-catenin:F-actin and Vcl:F-actin were set to identical values (see Table S1), the similar performance of the Vcl Only Configuration and Reinforced Configuration indicates that the effect of vinculin reinforcement on the AJ friction clutch was mainly driven by the force-dependent unbinding rate constant of the Vcl:F-actin bond.

Likewise, in the FA model, the performance of the Vcl Only Configuration was comparable to the Reinforced Configuration, however only across the lower part of the CCM speed range (Fig. S20h), indicating the importance of the Vcl:F-actin bond across some but not all speeds. In both the FA and AJ models, the Vcl Only Configuration showed the weakest performance compared to the Reinforced Configuration at the highest speeds. As higher speeds generally correspond to higher loading rates, this observation is consistent with vinculin's stabilization of individual linkages preferentially at lower and intermediate loading rates (Fig. S16), as well as the Vcl:F-actin bond having an optimum lifetime at forces of ~7 pN (Fig. S14).

Furthermore, we also sought to assess the relative magnitude of vinculin's effect in the context of another mechanism of adhesion reinforcement, namely increasing the abundance of integrin- or cadherin-based linkages (18, 50). To establish a comparison, we also performed simulations doubling the number of non-reinforced linkages (Fig S20 blue lines). Increasing the total number of non-reinforced linkages had little or no impact on the engagement lifetime of individual linkages (Fig. S20c,g), consistent with main effects on the total number of engaged linkages, not the behavior of individual linkages. In the AJ model, both the Reinforced and Vcl Only Configurations exhibited higher friction coefficients across all or most of the CCM speed range compared to doubling the number of non-reinforced linkages (Fig. S20d). In contrast, in the FA model, the effect of vinculin reinforcement was only higher across the lower part of the CCM speed range (Fig. S20h), consistent with its weaker effect in the FA model. Interestingly, in both the AJ and FA models increasing the number of non-reinforced linkages was most effective at increasing the friction coefficient at higher speeds, above those corresponding to CCM in our system.

Taken together, this data indicates that the ability of the vinculin switch to tune adhesion-based friction in the range of speeds relevant to CCM in our system, especially at the AJ, was driven mainly by the force-dependent unbinding of vinculin from F-actin, highlighting the force-sensitivity of vinculin's F-actin bond as a key model parameter. In this regime, the effect of vinculin reinforcement at the AJ was larger than that associated with doubling the number of non-reinforced linkages.

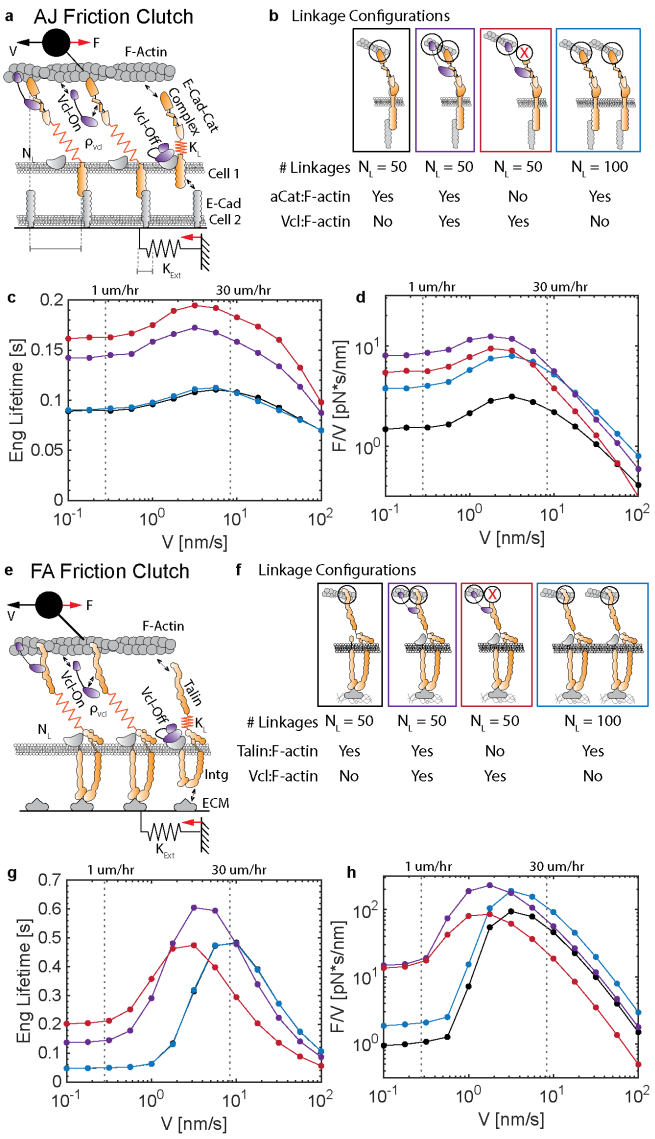

Fig. S20 Effect of Vcl-based Reinforcement is Driven by the Force-Sensitivity of Vinculin's F-actin Bond. (a) Schematic of AJ friction clutch. (b) Schematic of linkage configurations: (from left to right) all non-reinforced linkage with only α-catenin:F-actin able to bind the actin interface (black), all reinforced linkage with both α-catenin:F-actin and Vcl:F-actin able to bind the actin interface (purple), all "Vcl only linkage" with only Vcl:F-actin able to bind the actin interface (red), and twice the number of all non-reinforced linkage (blue). (c-d) Plots of mean engagement lifetime and effective friction coefficient (F/V) versus speed (V) for AJ friction clutch model. (e) Schematic of FA friction clutch. (f) Schematic of linkage configurations: (from left to right) all non-reinforced linkage with only Talin:F-actin able to bind the actin interface (black), all reinforced linkage with both Talin:F-actin and Vcl:F-actin able to bind the actin interface (purple), all "Vcl only linkage" with only Vcl:F-actin able to bind the actin interface (red), and twice the number of all non-reinforced linkage (blue). (g-h) Plots of mean engagement lifetime and effective friction coefficient (F/V) versus speed (V) for FA friction clutch model. The black and blue lines are nearly identical in (c) and (g).

G. Effect of Explicitly Modeling Both Sides of the AJ

The one-sided AJ friction clutch implemented in this work considers the frictional force resisting the relative cell-cell motion resulting from the extension of elastic molecular linkages that link the actin cytoskeleton of one cell to the cadherins on the surface of the adjacent cell. This simple model incorporates the loading source (relative cell-cell motion) and the major components and binding interfaces of cadherin-based linkages (cadherin and actin interfaces). However, because in AJs there are linkages to the actin cytoskeleton inside both cells, we also implemented a two-sided AJ friction clutch to assess the effect of this second F-actin interface. The two-sided AJ friction clutch explicitly models the transmission of forces across complete molecular linkages between the actin cytoskeleton in Cell 2 through the cadherin:cadherin interface and to the actin cytoskeleton in Cell 1 (see model formulation in Section II-L). In this case, the linkage must be bound at both F-actin interfaces and the Cadherin interface to be engaged and transmit forces.

To assess the effects of explicitly modeling both actin interfaces, we compared key features of the one- and two-sided AJ friction clutch models. There are differences in the absolute values of engagement lifetime (Fig S21c-d) and effective friction coefficient (Fig S21e-f), which can be explained by a decrease in the effective on rate and increase in the effective off rate for linkages that require an additional bond in series. However, despite differences in absolute values, the one- and two-sided models exhibit the same functional forms for engagement lifetime versus speed (Fig S21c-d) and effective friction coefficient (F/V) versus speed (Fig S21e-f) for both non-reinforced ($\rho_{Vcl} = 0$) and vinculin-reinforced ($\rho_{Vcl} = 1$) configurations. Also, in both the one- and two-sided models vinculin reinforcement significantly increases the engagement lifetime and effective friction coefficient over the range of relative cell-cell speeds corresponding to monolayer velocities (Fig S21e-f). In fact, as the actin interface drives linkage disengagement and there are now two of these interfaces which vinculin can reinforce, the magnitude of vinculin's effect on the friction coefficient is higher in the two-sided model.

Taken together, explicitly modeling the full linkage in a two-sided AJ affects the absolute value of model outputs but does not affect the functional forms of engagement lifetime and friction coefficient versus speed or the relative effect of vinculin reinforcement on engagement lifetime and friction coefficient. Therefore, the one- and two-sided models are equivalent for the purposes of assessing and predicting the relative effects of perturbing properties of the linkages on the friction between cells in the context of the experiments performed here.

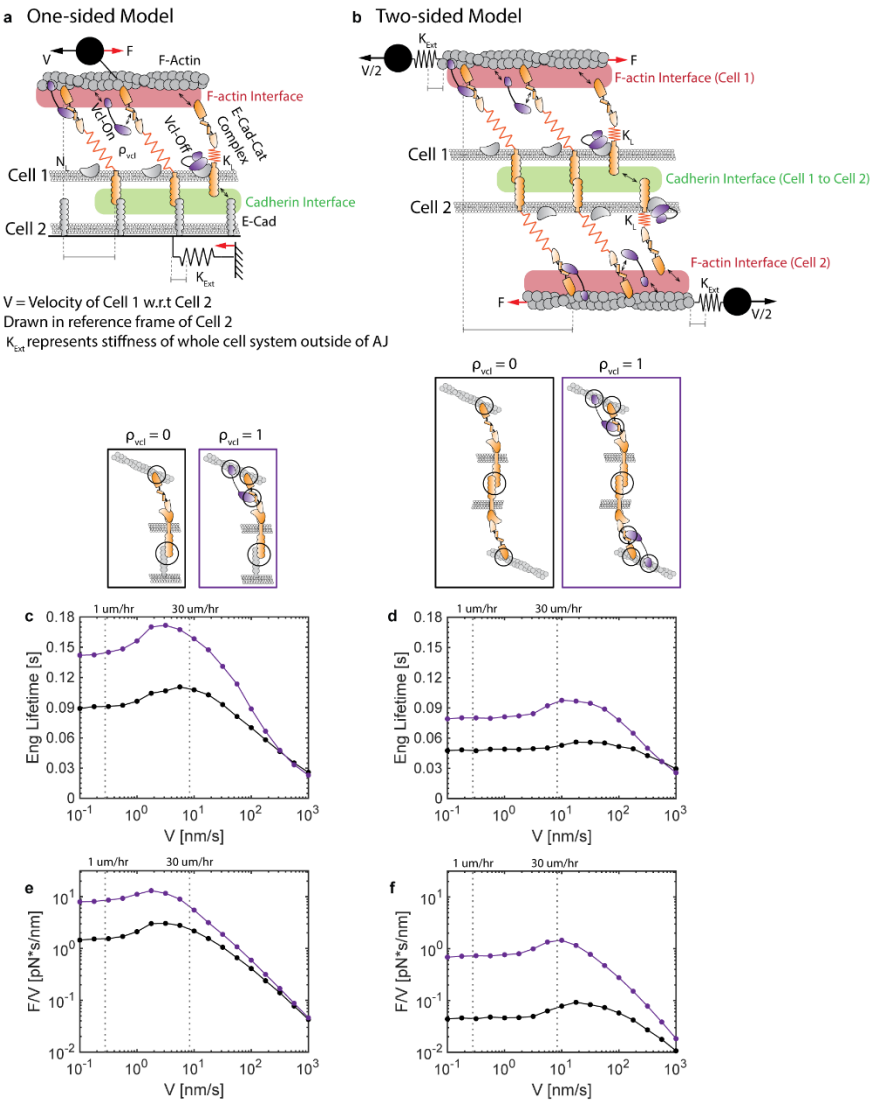

Fig. S21 Effect of explicitly modeling the actin interface on both sides of the AJ. (a) Schematic of one-sided AJ friction clutch (for comparison), which models the transmission of forces across molecular linkages between the cadherins on the surface of cell 2 and the actin cytoskeleton in cell 1. (b) Schematic of two-sided AJ friction clutch, which explicitly models the transmission of forces across complete molecular linkages between the actin cytoskeleton in Cell 2, through the cadherin interface, to the actin cytoskeleton in Cell 1. (c-d) Plot of mean linkage engagement lifetime versus speed (V) in the absence ($\boldsymbol{\rho_{Vcl} = 0}$) and presence ($\boldsymbol{\rho_{Vcl} = 1}$) of vinculin reinforcement, for (c) one- and (d) two-sided AJ friction clutch. (e-f) Plots of mean effective friction coefficient (F/V) versus speed (V) in the absence ($\boldsymbol{\rho_{Vcl} = 0}$) and presence ($\boldsymbol{\rho_{Vcl} = 1}$) of vinculin reinforcement, for (e) one- and (f) two-sided AJ friction clutch. Note: Plots for one-sided model (c,e) correspond to newly run simulations that match prior simulations under the base parameters.

IV. MODEL ASSUMPTIONS, LIMITATIONS, AND POSSIBLE EXTENSIONS

The FA and AJ friction clutch models share the basic assumptions previously detailed for motor clutch models (22, 24), except that no assumption on the force-velocity relationship for actomyosin-driven retrograde flow is required. Instead, a fixed velocity is imposed corresponding to relative motion at the cell-ECM or cell-cell interface occurring during CCM. Speeds based on MDCK monolayer velocities observed in this work and by others (25) are used. In the rest of this section, we cover assumptions that are specific to the modeling of multi-bond linkages and vinculin mechanical reinforcement.

The following assumptions are made regarding the mechanical connectivity of vinculin in integrin- and cadherin-based linkages. First, we consider only 1 vinculin binding site (VBS) per linkage. However, Talin contains multiple VBS, and vinculin is also known to bind proteins other than Talin that associate with integrins, such as paxillin, or proteins other than α-Catenin that associate with E-cadherin, such as β-catenin (45, 51). These could result in additional vinculin-mediated connections to the actin interface in parallel to the existing actin bonds, resulting in further stabilization of the linkages and potentially even higher increases in force transmission. As such, the assumption of one VBS per linkage likely underestimates the effect of loadable vinculin on adhesion-based friction. Second, we assumed that the addition of vinculin to linkages does not appreciably alter the effective spring constant of the linkage. This assumption was made because the effective stiffness of full multi-protein linkages at the FA and AJ are not known. It is motivated by the likelihood that large portions of the integrin-/cadherin-based linkages located between the external surface and the VBS (mainly the integrin and cadherin molecules themselves) set the effective spring constant for the full linkage. However, if adapter proteins could alter the effective spring constant of the linkage, it could provide another means to alter friction at adhesions, which could be explored further in future models. Third, when both vinculin and Talin or α-catenin are bound at the actin interface, we assumed that loads are shared equally between the two parallel bonds, as it is not known how the forces inside integrin-/cadherin-based linkages at FAs/AJs inside cells are distributed. Deviations from this assumption would affect the interplay between the force-sensitive unbinding kinetics of actin bonds in parallel, which could also be explored in future models.

Furthermore, the following assumptions are made regarding the mechanochemical properties and regulation of vinculin. We modeled vinculin in mechanical linkages existing in one of two states, capable or incapable of bearing loads, and treated the relative fraction of vinculin in each of these states to be tunable (via the parameter ρ_{Vcl}). The number of states vinculin exists in at FAs and AJs is likely higher, and the regulation of the distribution of vinculin in these states is likely more complex (44-46, 52). As the biological mechanisms are just being elucidated, this is an important point for future work. However, as the two-state formulation represents the extremes of vinculin mechanical function, our approach likely captures key aspects of the system.

Lastly, we consider the effect of vinculin due to the addition of a direct load-bearing linkage to F-actin. This is supported by the fact that vinculin molecular tension regulates FA dynamics (9) and AJ remodeling (14), and that vinculin's effects on traction forces and adhesion strength require the physical coupling between the head and tail domain of full-length vinculin (49). However, we note that vinculin could additionally affect force transmission at FAs and AJs through indirect effects, including promoting the opening of Talin and α-catenin, as well as the mechanosensitive recruitment of other adhesion or actin-binding proteins (13, 30, 46, 53, 54). Furthermore, recent work has demonstrated that vinculin plays a role in the inside-out regulation of cadherin conformation (55). This suggests that vinculin reinforcement could also alter friction at the AJ through regulating the type of force-sensitive bond kinetics at the cadherin interface. Therefore, determining relationships between vinculin state or molecular loading and this cadherin-based mechanism is an important point for future work. As more mechanisms become elucidated, future versions of the model could be updated to include vinculin-mediated regulation of the state of other bonds in the linkage as well as the recruitment of additional proteins to adhesion structures.

V. CONCLUSIONS

CCM requires the transmission of forces between cells and to the environment (1-3). Physical models of CCM based on mechanical forces exerted between cells and at the cell-ECM interface have advanced our understanding of this process, including recent work showing that cell-cell and cell-ECM friction are major determinants of CCM dynamics (1, 5, 6). However, these models lack insight into the molecular players that regulate key biophysical parameters. Therefore, to probe the relationship between force-activated binding dynamics and adhesion-based friction, we developed stochastic models of friction at AJs/FAs based on multi-component cadherin-/integrin-based linkages with force-sensitive bond parameters from single molecule experiments. Specifically, we investigated the effect of vinculin loading on molecular friction at the FA and AJ. We found that vinculin reinforcement enhances the lifetime of cadherin-/integrin-mediated linkages under load and thereby increases the effective friction coefficient at AJs/FAs across a range of speeds corresponding to cell speeds during CCM. At higher speeds, the effective friction coefficient sharply decreases regardless of vinculin reinforcement, consistent with a distinct weak adhesion regime previously reported (5). The effect of loaded vinculin on friction was larger at AJs (~4-fold increase in friction) than at FAs (~2-fold increase in friction). Increases in friction were associated with increases in ensemble vinculin molecular tension. Vinculin reinforcement was effective at tuning adhesion-based friction across a wide parameter space. In the context of macroscopic physical models of CCM, the effect of vinculin loading on adhesion-based friction is consistent with the observed effects of loaded vinculin on CCM dynamics in our experiments. Overall, these modeling efforts provide a framework to bridge molecular scale dynamics and regulation to macroscopic physical parameters, which could inform the future development of physical models of CCM and facilitate connections between biological and mechanical descriptions of CCM.

Supplementary Note 2: Supporting Tables for Statistical Tests

In this supplemental note, we provide supporting tables containing the p-values for statistical tests performed on experiments with VinTS or VinCS that were plotted separately over more than one figure, as well as the p-values for the statistical tests performed on the CCM kinematics data.

The following information is contained in this supplemental note:

- Table S4 and Fig. S22 contain MDCK II VinTS and VinTS-I997A data from Fig. 1 and Fig. S5.
- Table S5 and Fig. S23 contain MDCK II and MDCK Parental VinCS data from Fig. 1, Fig. S2, and Fig. S3.
- Table S6 and Fig. S24 contain MDCK Parental VinTS, VinTS-I997A, and VinTS-Y822F data from Fig. S3, Fig. S5, Fig. S6, and Fig. S7.
- Table S7 contains MDCK Parental VinTS, VinTS-S1033A, and VinTS-S1033D data from Fig. 2 and Fig. S8.
- Table S8 contains MDCK Parental VinCS, VinCS-S1033A, and VinCS-S1033D data from Fig. 2 and Fig. S8 and MDCK Parental VinCS data in Fig. S6.
- Table S9 contains speed (velocity magnitude) data for MDCK II Vcl KO and rescue with VinV-WT, VinV-S1033A, or VinV-S1033D from Fig. 3e.
- Table S10 contains correlation length data for MDCK II Vcl KO and rescue with VinV-WT, VinV-S1033A, or VinV-S1033D from Fig. 3f.

See the methods section of the manuscript for a description of all statistical methods.

Table S4. P-values from Steel-Dwass Test for MDCK II VinTS and VinTS-I997A Mean Eff in Fig. 1 and Fig. S5. Levels are labeled as [Cell Type]_[Construct]_[Condition]_[Structure].

Level	- Level	p-Value
MDCKII_VinTSI997A_Live_ApicalCyto	MDCKII_VinTSI997A_Live_AJ	0.9831
MDCKII_VinTS_Live_ApicalCyto	MDCKII_VinTS_Live_AJ	1
MDCKII_VinTSI997A_Live_FA	MDCKII_VinTSI997A_Live_AJ	0.9961
MDCKII_VinTSI997A_Live_FA	MDCKII_VinTSI997A_Live_ApicalCyto	0.8415
MDCKII_VinTS_Live_ApicalCyto	MDCKII_VinTSI997A_Live_AJ	<.0001
MDCKII_VinTS_Live_AJ	MDCKII_VinTSI997A_Live_AJ	<.0001
MDCKII_VinTS_Live_ApicalCyto	MDCKII_VinTSI997A_Live_ApicalCyto	<.0001
MDCKII_VinTS_Live_AJ	MDCKII_VinTSI997A_Live_ApicalCyto	<.0001
MDCKII_VinTS_Live_ApicalCyto	MDCKII_VinTSI997A_Live_FA	<.0001
MDCKII_VinTS_Live_AJ	MDCKII_VinTSI997A_Live_FA	<.0001
MDCKII_VinTS_Live_FA	MDCKII_VinTS_Live_ApicalCyto	<.0001
MDCKII_VinTS_Live_FA	MDCKII_VinTS_Live_AJ	<.0001
MDCKII_VinTS_Live_FA	MDCKII_VinTSI997A_Live_AJ	<.0001
MDCKII_VinTS_Live_FA	MDCKII_VinTSI997A_Live_ApicalCyto	<.0001
MDCKII_VinTS_Live_FA	MDCKII_VinTSI997A_Live_FA	<.0001

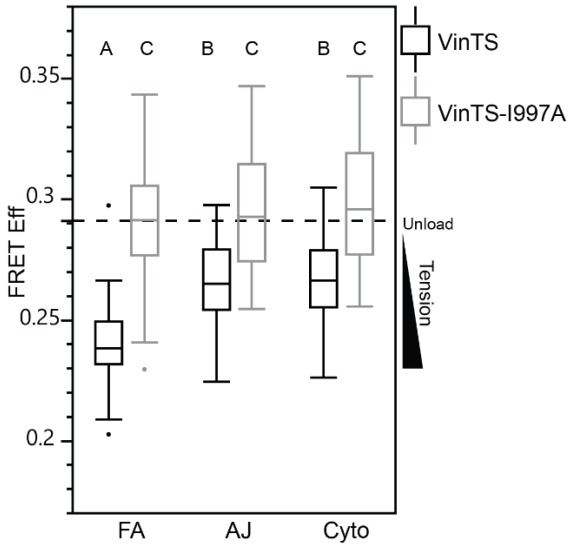

Fig. S22. Combined box plot of MDCK II VinTS and VinTS-I997A data from Fig. 1 and Fig. S5 corresponding to Table S4. Differences between groups were detected using the Steel-Dwass test. Levels not connected by the same letter are significantly different at $p<0.05$.

Table S5. P-values from Steel-Dwass Test for VinCS Mean Eff in Fig. 1, Fig. S2, and Fig. S3. Levels are labeled as [Cell Type]_[Construct]_[Condition]_[Structure]. For Structure, “FA”, “AJ”, and “Cyto” indicate subcell structures in cell monolayers and “pL” indicates the cytosol of single cells adhered to poly-L-lysine surface.

Level	- Level	p-Value
pMDCK_VinCS_Live_pL	pMDCK_VinCS_Live_FA	<.0001
pMDCK_VinCS_Live_pL	MDCKII_VinCS_Live_FA	<.0001
pMDCK_VinCS_Live_pL	pMDCK_VinCS_Live_AJ	<.0001
pMDCK_VinCS_Live_pL	MDCKII_VinCS_Live_AJ	<.0001
pMDCK_VinCS_Live_pL	pMDCK_VinCS_Live_ApicalCyto	<.0001
pMDCK_VinCS_Live_pL	MDCKII_VinCS_Live_ApicalCyto	<.0001
pMDCK_VinCS_Live_ApicalCyto	pMDCK_VinCS_Live_FA	<.0001
pMDCK_VinCS_Live_AJ	pMDCK_VinCS_Live_FA	<.0001
MDCKII_VinCS_Live_ApicalCyto	MDCKII_VinCS_Live_FA	<.0001
pMDCK_VinCS_Live_ApicalCyto	MDCKII_VinCS_Live_FA	<.0001
MDCKII_VinCS_Live_AJ	MDCKII_VinCS_Live_FA	<.0001
pMDCK_VinCS_Live_ApicalCyto	pMDCK_VinCS_Live_AJ	<.0001
pMDCK_VinCS_Live_AJ	MDCKII_VinCS_Live_FA	<.0001
MDCKII_VinCS_Live_ApicalCyto	MDCKII_VinCS_Live_AJ	0.0716
pMDCK_VinCS_Live_ApicalCyto	MDCKII_VinCS_Live_AJ	0.9951
pMDCK_VinCS_Live_ApicalCyto	MDCKII_VinCS_Live_ApicalCyto	0.5277
pMDCK_VinCS_Live_AJ	MDCKII_VinCS_Live_AJ	0.0008
pMDCK_VinCS_Live_AJ	MDCKII_VinCS_Live_ApicalCyto	<.0001
pMDCK_VinCS_Live_FA	MDCKII_VinCS_Live_FA	<.0001
pMDCK_VinCS_Live_FA	MDCKII_VinCS_Live_AJ	<.0001
pMDCK_VinCS_Live_FA	MDCKII_VinCS_Live_ApicalCyto	<.0001

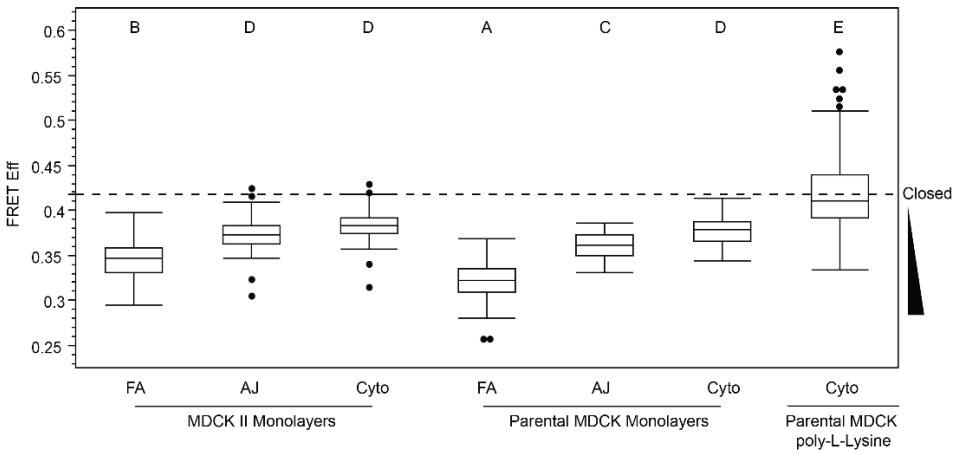

Fig. S23. Combined box plot of MDCK II and Parental MDCK VinCS data from Fig. 1, Fig. S2, and Fig. S3 corresponding to Table S5. Differences between groups were detected using the Steel-Dwass test. Levels not connected by the same letter are significantly different at $p<0.05$.

Table S6. P-values from Steel-Dwass Test for MDCK Parental VinTS, VinTS-I997A, and VinTS-Y822F Mean Eff in Fig. S3, Fig. S5, Fig. S6, and Fig. S7. Levels are labeled as [Cell Type]_[Construct]_[Condition]_[Structure].

Level	- Level	p-Value
pMDCK_VinTSY822F_Fix_ApicalCyto	pMDCK_VinTS_Fix_FA	<.0001
pMDCK_VinTSY822F_Fix_ApicalCyto	pMDCK_VinTS_Fix_AJ	0.0005
pMDCK_VinTSY822F_Fix_AJ	pMDCK_VinTS_Fix_FA	0.0039
pMDCK_VinTS_Live_ApicalCyto	pMDCK_VinTS_Fix_FA	0.0178
pMDCK_VinTSY822F_Fix_ApicalCyto	pMDCK_VinTS_Live_FA	<.0001
pMDCK_VinTS_Fix_ApicalCyto	pMDCK_VinTS_Fix_AJ	0.3947
pMDCK_VinTSI997A_Live_ApicalCyto	pMDCK_VinTSI997A_Fix_FA	0.003
pMDCK_VinTSY822F_Fix_ApicalCyto	pMDCK_VinTS_Fix_ApicalCyto	0.5326
pMDCK_VinTSY822F_Fix_AJ	pMDCK_VinTS_Fix_AJ	0.6251
pMDCK_VinTSY822F_Fix_AJ	pMDCK_VinTS_Live_FA	0.0517
pMDCK_VinTS_Live_AJ	pMDCK_VinTS_Fix_FA	0.6909
pMDCK_VinTSI997A_Fix_ApicalCyto	pMDCK_VinTSI997A_Fix_AJ	0.2442
pMDCK_VinTSI997A_Live_AJ	pMDCK_VinTSI997A_Fix_FA	0.0779
pMDCK_VinTSY822F_Fix_ApicalCyto	pMDCK_VinTS_Live_AJ	0.0958
pMDCK_VinTS_Live_ApicalCyto	pMDCK_VinTS_Fix_AJ	0.9164
pMDCK_VinTSY822F_Fix_ApicalCyto	pMDCK_VinTSY822F_Fix_AJ	0.3827
pMDCK_VinTSI997A_Live_FA	pMDCK_VinTSI997A_Fix_FA	0.703
pMDCK_VinTSY822F_Fix_ApicalCyto	pMDCK_VinTS_Live_ApicalCyto	0.7831
pMDCK_VinTSI997A_Live_ApicalCyto	pMDCK_VinTSI997A_Fix_AJ	0.9967
pMDCK_VinTSY822F_Fix_AJ	pMDCK_VinTS_Live_AJ	0.9898
pMDCK_VinTS_Live_ApicalCyto	pMDCK_VinTS_Live_AJ	0.9924
pMDCK_VinTSI997A_Live_ApicalCyto	pMDCK_VinTSI997A_Live_AJ	0.9991
pMDCK_VinTS_Live_AJ	pMDCK_VinTS_Fix_AJ	1
pMDCK_VinTS_Live_FA	pMDCK_VinTS_Fix_FA	1
pMDCK_VinTSY822F_Fix_AJ	pMDCK_VinTS_Fix_ApicalCyto	1
pMDCK_VinTSI997A_Live_AJ	pMDCK_VinTSI997A_Fix_AJ	1
pMDCK_VinTSY822F_Fix_AJ	pMDCK_VinTS_Live_ApicalCyto	1
pMDCK_VinTS_Live_ApicalCyto	pMDCK_VinTS_Fix_ApicalCyto	1
pMDCK_VinTSY822F_Fix_FA	pMDCK_VinTS_Live_FA	1
pMDCK_VinTSY822F_Fix_FA	pMDCK_VinTS_Fix_FA	1
pMDCK_VinTSI997A_Live_ApicalCyto	pMDCK_VinTSI997A_Fix_ApicalCyto	1
pMDCK_VinTSI997A_Live_FA	pMDCK_VinTSI997A_Live_AJ	0.9961
pMDCK_VinTSI997A_Live_FA	pMDCK_VinTSI997A_Live_ApicalCyto	0.5553
pMDCK_VinTSI997A_Live_FA	pMDCK_VinTSI997A_Fix_AJ	0.9361
pMDCK_VinTSY822F_Fix_ApicalCyto	pMDCK_VinTSI997A_Fix_FA	0.835
pMDCK_VinTS_Live_FA	pMDCK_VinTS_Live_AJ	0.8027
pMDCK_VinTSI997A_Live_AJ	pMDCK_VinTSI997A_Fix_ApicalCyto	0.8574

pMDCK_VinTSY822F_Fix_FA	pMDCK_VinTS_Live_AJ	0.5832
pMDCK_VinTS_Live_AJ	pMDCK_VinTS_Fix_ApicalCyto	0.9653
pMDCK_VinTSY822F_Fix_ApicalCyto	pMDCK_VinTSI997A_Live_FA	0.0514
pMDCK_VinTS_Live_FA	pMDCK_VinTS_Fix_AJ	0.8181
pMDCK_VinTSY822F_Fix_FA	pMDCK_VinTS_Live_ApicalCyto	0.0231
pMDCK_VinTS_Live_FA	pMDCK_VinTS_Live_ApicalCyto	0.0764
pMDCK_VinTSY822F_Fix_ApicalCyto	pMDCK_VinTSI997A_Live_AJ	0.0014
pMDCK_VinTS_Live_ApicalCyto	pMDCK_VinTSI997A_Fix_FA	0.028
pMDCK_VinTS_Live_ApicalCyto	pMDCK_VinTSI997A_Live_FA	0.002
pMDCK_VinTSY822F_Fix_ApicalCyto	pMDCK_VinTSI997A_Live_ApicalCyto	0.0001
pMDCK_VinTSY822F_Fix_AJ	pMDCK_VinTSI997A_Live_FA	0.0003
pMDCK_VinTSY822F_Fix_FA	pMDCK_VinTSY822F_Fix_AJ	0.0008
pMDCK_VinTS_Live_ApicalCyto	pMDCK_VinTSI997A_Live_AJ	0.0002
pMDCK_VinTSY822F_Fix_AJ	pMDCK_VinTSI997A_Live_AJ	<.0001
pMDCK_VinTSI997A_Live_FA	pMDCK_VinTSI997A_Fix_ApicalCyto	0.0084
pMDCK_VinTSY822F_Fix_FA	pMDCK_VinTS_Fix_AJ	0.291
pMDCK_VinTSY822F_Fix_AJ	pMDCK_VinTSI997A_Fix_FA	0.001
pMDCK_VinTS_Live_AJ	pMDCK_VinTSI997A_Live_FA	<.0001
pMDCK_VinTSY822F_Fix_AJ	pMDCK_VinTSI997A_Live_ApicalCyto	<.0001
pMDCK_VinTS_Live_AJ	pMDCK_VinTSI997A_Live_AJ	<.0001
pMDCK_VinTS_Live_ApicalCyto	pMDCK_VinTSI997A_Live_ApicalCyto	<.0001
pMDCK_VinTS_Fix_FA	pMDCK_VinTS_Fix_AJ	0.2437
pMDCK_VinTS_Live_AJ	pMDCK_VinTSI997A_Fix_FA	0.0002
pMDCK_VinTS_Live_AJ	pMDCK_VinTSI997A_Live_ApicalCyto	<.0001
pMDCK_VinTSY822F_Fix_FA	pMDCK_VinTSI997A_Live_AJ	<.0001
pMDCK_VinTSI997A_Fix_FA	pMDCK_VinTSI997A_Fix_AJ	0.0005
pMDCK_VinTSY822F_Fix_FA	pMDCK_VinTSY822F_Fix_ApicalCyto	<.0001
pMDCK_VinTSY822F_Fix_FA	pMDCK_VinTSI997A_Live_ApicalCyto	<.0001
pMDCK_VinTSY822F_Fix_FA	pMDCK_VinTSI997A_Live_FA	<.0001
pMDCK_VinTS_Live_FA	pMDCK_VinTS_Fix_ApicalCyto	0.0096
pMDCK_VinTSY822F_Fix_ApicalCyto	pMDCK_VinTSI997A_Fix_AJ	<.0001
pMDCK_VinTS_Live_FA	pMDCK_VinTSI997A_Live_FA	<.0001
pMDCK_VinTS_Live_FA	pMDCK_VinTSI997A_Live_AJ	<.0001
pMDCK_VinTS_Fix_ApicalCyto	pMDCK_VinTSI997A_Fix_FA	0.0012
pMDCK_VinTS_Live_FA	pMDCK_VinTSI997A_Live_ApicalCyto	<.0001
pMDCK_VinTSY822F_Fix_FA	pMDCK_VinTS_Fix_ApicalCyto	0.0011
pMDCK_VinTSY822F_Fix_FA	pMDCK_VinTSI997A_Fix_FA	<.0001
pMDCK_VinTS_Live_ApicalCyto	pMDCK_VinTSI997A_Fix_AJ	<.0001
pMDCK_VinTS_Live_FA	pMDCK_VinTSI997A_Fix_FA	<.0001
pMDCK_VinTSI997A_Fix_FA	pMDCK_VinTSI997A_Fix_ApicalCyto	<.0001
pMDCK_VinTS_Fix_ApicalCyto	pMDCK_VinTSI997A_Live_FA	0.0002

pMDCK_VinTSY822F_Fix_AJ	pMDCK_VinTSI997A_Fix_AJ	<.0001
pMDCK_VinTS_Live_AJ	pMDCK_VinTSI997A_Fix_AJ	<.0001
pMDCK_VinTSY822F_Fix_ApicalCyto	pMDCK_VinTSI997A_Fix_ApicalCyto	<.0001
pMDCK_VinTS_Live_ApicalCyto	pMDCK_VinTSI997A_Fix_ApicalCyto	<.0001
pMDCK_VinTS_Fix_FA	pMDCK_VinTS_Fix_ApicalCyto	<.0001
pMDCK_VinTS_Live_AJ	pMDCK_VinTSI997A_Fix_ApicalCyto	<.0001
pMDCK_VinTSY822F_Fix_AJ	pMDCK_VinTSI997A_Fix_ApicalCyto	<.0001
pMDCK_VinTS_Fix_ApicalCyto	pMDCK_VinTSI997A_Live_AJ	<.0001
pMDCK_VinTSY822F_Fix_FA	pMDCK_VinTSI997A_Fix_AJ	<.0001
pMDCK_VinTSY822F_Fix_FA	pMDCK_VinTSI997A_Fix_ApicalCyto	<.0001
pMDCK_VinTS_Fix_AJ	pMDCK_VinTSI997A_Live_FA	<.0001
pMDCK_VinTS_Fix_AJ	pMDCK_VinTSI997A_Fix_FA	<.0001
pMDCK_VinTS_Fix_ApicalCyto	pMDCK_VinTSI997A_Live_ApicalCyto	<.0001
pMDCK_VinTS_Live_FA	pMDCK_VinTSI997A_Fix_AJ	<.0001
pMDCK_VinTS_Fix_AJ	pMDCK_VinTSI997A_Live_AJ	<.0001
pMDCK_VinTS_Live_FA	pMDCK_VinTSI997A_Fix_ApicalCyto	<.0001
pMDCK_VinTS_Fix_AJ	pMDCK_VinTSI997A_Live_ApicalCyto	<.0001
pMDCK_VinTS_Fix_FA	pMDCK_VinTSI997A_Live_FA	<.0001
pMDCK_VinTS_Fix_FA	pMDCK_VinTSI997A_Fix_FA	<.0001
pMDCK_VinTS_Fix_FA	pMDCK_VinTSI997A_Live_AJ	<.0001
pMDCK_VinTS_Fix_ApicalCyto	pMDCK_VinTSI997A_Fix_AJ	<.0001
pMDCK_VinTS_Fix_FA	pMDCK_VinTSI997A_Live_ApicalCyto	<.0001
pMDCK_VinTS_Fix_ApicalCyto	pMDCK_VinTSI997A_Fix_ApicalCyto	<.0001
pMDCK_VinTS_Fix_AJ	pMDCK_VinTSI997A_Fix_AJ	<.0001
pMDCK_VinTS_Fix_FA	pMDCK_VinTSI997A_Fix_AJ	<.0001
pMDCK_VinTS_Fix_AJ	pMDCK_VinTSI997A_Fix_ApicalCyto	<.0001
pMDCK_VinTS_Fix_FA	pMDCK_VinTSI997A_Fix_ApicalCyto	<.0001

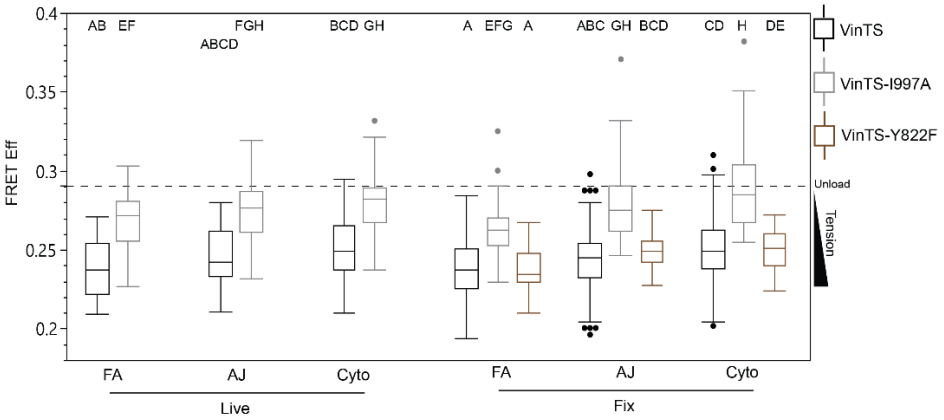

Fig. S24. Combined box plot of MDCK Parental VinTS, VinTS-I997A, and VinTS-Y822F data from Fig. S3, Fig. S5, Fig. S6, and Fig. S7 corresponding to Table S6. Differences between groups were detected using the Steel-Dwass test. Levels not connected by the same letter are significantly different at $p<0.05$.

Table S7. P-values from Steel-Dwass Test for MDCK Parental VinTS S1033 Mutant FRET Eff in Fig. 2 and Fig. S8. Levels are labeled as [Cell Type]_[Construct]_[Condition]_[Structure].

Level	- Level	p-Value
pMDCK_VinTSS1033D_Fix_ApicalCyto	pMDCK_VinTS_Fix_FA	<.0001
pMDCK_VinTSS1033D_Fix_AJ	pMDCK_VinTS_Fix_FA	<.0001
pMDCK_VinTSS1033D_Fix_FA	pMDCK_VinTS_Fix_FA	<.0001
pMDCK_VinTSS1033D_Fix_ApicalCyto	pMDCK_VinTS_Fix_AJ	<.0001
pMDCK_VinTSS1033D_Fix_AJ	pMDCK_VinTS_Fix_AJ	<.0001
pMDCK_VinTSS1033D_Fix_ApicalCyto	pMDCK_VinTS_Fix_ApicalCyto	<.0001
pMDCK_VinTSS1033D_Fix_AJ	pMDCK_VinTS_Fix_ApicalCyto	<.0001
pMDCK_VinTSS1033D_Fix_ApicalCyto	pMDCK_VinTSS1033A_Fix_AJ	<.0001
pMDCK_VinTSS1033D_Fix_AJ	pMDCK_VinTSS1033A_Fix_AJ	<.0001
pMDCK_VinTSS1033D_Fix_ApicalCyto	pMDCK_VinTSS1033A_Fix_ApicalCyto	<.0001
pMDCK_VinTSS1033D_Fix_AJ	pMDCK_VinTSS1033A_Fix_ApicalCyto	<.0001
pMDCK_VinTSS1033D_Fix_ApicalCyto	pMDCK_VinTSS1033A_Fix_FA	<.0001
pMDCK_VinTSS1033D_Fix_AJ	pMDCK_VinTSS1033A_Fix_FA	<.0001
pMDCK_VinTSS1033D_Fix_FA	pMDCK_VinTS_Fix_AJ	<.0001
pMDCK_VinTSS1033D_Fix_FA	pMDCK_VinTSS1033A_Fix_AJ	<.0001
pMDCK_VinTSS1033D_Fix_FA	pMDCK_VinTSS1033A_Fix_FA	<.0001
pMDCK_VinTSS1033A_Fix_ApicalCyto	pMDCK_VinTS_Fix_FA	<.0001
pMDCK_VinTSS1033D_Fix_FA	pMDCK_VinTS_Fix_ApicalCyto	<.0001
pMDCK_VinTSS1033D_Fix_FA	pMDCK_VinTSS1033A_Fix_ApicalCyto	<.0001
pMDCK_VinTSS1033A_Fix_AJ	pMDCK_VinTS_Fix_FA	0.0029
pMDCK_VinTSS1033A_Fix_ApicalCyto	pMDCK_VinTSS1033A_Fix_AJ	0.4952
pMDCK_VinTS_Fix_ApicalCyto	pMDCK_VinTS_Fix_AJ	0.8893
pMDCK_VinTSS1033D_Fix_ApicalCyto	pMDCK_VinTSS1033D_Fix_AJ	0.8634
pMDCK_VinTSS1033A_Fix_FA	pMDCK_VinTS_Fix_FA	0.9974
pMDCK_VinTSS1033A_Fix_ApicalCyto	pMDCK_VinTS_Fix_AJ	0.9992
pMDCK_VinTSS1033A_Fix_ApicalCyto	pMDCK_VinTS_Fix_ApicalCyto	0.9994
pMDCK_VinTSS1033A_Fix_AJ	pMDCK_VinTS_Fix_AJ	0.7585
pMDCK_VinTSS1033A_Fix_FA	pMDCK_VinTSS1033A_Fix_AJ	0.2722
pMDCK_VinTSS1033A_Fix_AJ	pMDCK_VinTS_Fix_ApicalCyto	0.0879
pMDCK_VinTSS1033A_Fix_FA	pMDCK_VinTS_Fix_AJ	0.0062
pMDCK_VinTSS1033A_Fix_FA	pMDCK_VinTSS1033A_Fix_ApicalCyto	0.004
pMDCK_VinTSS1033A_Fix_FA	pMDCK_VinTS_Fix_ApicalCyto	0.0002
pMDCK_VinTSS1033D_Fix_FA	pMDCK_VinTSS1033D_Fix_AJ	<.0001
pMDCK_VinTSS1033D_Fix_FA	pMDCK_VinTSS1033D_Fix_ApicalCyto	<.0001
pMDCK_VinTS_Fix_FA	pMDCK_VinTS_Fix_AJ	<.0001
pMDCK_VinTS_Fix_FA	pMDCK_VinTS_Fix_ApicalCyto	<.0001

Table S8. P-values from Steel-Dwass Test for MDCK Parental VinCS S1033 Mutant Norm FRET Eff Data in Fig. 2 and Fig. S8 and MDCK Parental VinCS Live Norm FRET Eff Data in Fig. S6. Levels are labeled as [Cell Type]_[Construct]_[Condition]_[Structure].

Level	- Level	p-Value
pMDCK_VinCSS1033D_Fix_ApicalCyto	pMDCK_VinCS_Fix_FA	<.0001
pMDCK_VinCSS1033D_Fix_AJ	pMDCK_VinCS_Fix_FA	<.0001
pMDCK_VinCSS1033D_Fix_FA	pMDCK_VinCS_Fix_FA	<.0001
pMDCK_VinCSS1033A_Fix_ApicalCyto	pMDCK_VinCS_Fix_FA	<.0001
pMDCK_VinCSS1033A_Fix_AJ	pMDCK_VinCS_Fix_FA	<.0001
pMDCK_VinCS_Live_ApicalCyto	pMDCK_VinCS_Fix_FA	<.0001
pMDCK_VinCS_Live_AJ	pMDCK_VinCS_Fix_FA	<.0001
pMDCK_VinCSS1033D_Fix_ApicalCyto	pMDCK_VinCS_Fix_AJ	<.0001
pMDCK_VinCSS1033D_Fix_AJ	pMDCK_VinCS_Live_FA	<.0001
pMDCK_VinCSS1033D_Fix_ApicalCyto	pMDCK_VinCS_Live_FA	<.0001
pMDCK_VinCSS1033D_Fix_AJ	pMDCK_VinCS_Fix_AJ	<.0001
pMDCK_VinCSS1033D_Fix_AJ	pMDCK_VinCSS1033A_Fix_FA	<.0001
pMDCK_VinCSS1033D_Fix_ApicalCyto	pMDCK_VinCSS1033A_Fix_FA	<.0001
pMDCK_VinCSS1033D_Fix_ApicalCyto	pMDCK_VinCS_Fix_ApicalCyto	<.0001
pMDCK_VinCSS1033D_Fix_FA	pMDCK_VinCS_Live_FA	<.0001
pMDCK_VinCSS1033D_Fix_AJ	pMDCK_VinCS_Fix_ApicalCyto	<.0001
pMDCK_VinCSS1033A_Fix_ApicalCyto	pMDCK_VinCS_Live_FA	<.0001
pMDCK_VinCSS1033D_Fix_FA	pMDCK_VinCSS1033A_Fix_FA	<.0001
pMDCK_VinCSS1033A_Fix_AJ	pMDCK_VinCS_Live_FA	<.0001
pMDCK_VinCSS1033A_Fix_ApicalCyto	pMDCK_VinCS_Fix_AJ	0.0019
pMDCK_VinCSS1033D_Fix_ApicalCyto	pMDCK_VinCS_Live_AJ	<.0001
pMDCK_VinCSS1033D_Fix_ApicalCyto	pMDCK_VinCSS1033A_Fix_AJ	0.0001
pMDCK_VinCSS1033D_Fix_AJ	pMDCK_VinCS_Live_AJ	<.0001
pMDCK_VinCSS1033D_Fix_AJ	pMDCK_VinCSS1033A_Fix_AJ	0.0004
pMDCK_VinCSS1033D_Fix_ApicalCyto	pMDCK_VinCS_Live_ApicalCyto	0.0029
pMDCK_VinCSS1033D_Fix_ApicalCyto	pMDCK_VinCSS1033A_Fix_ApicalCyto	0.0037
pMDCK_VinCS_Live_ApicalCyto	pMDCK_VinCS_Fix_AJ	0.056
pMDCK_VinCSS1033D_Fix_AJ	pMDCK_VinCSS1033A_Fix_ApicalCyto	0.0154
pMDCK_VinCSS1033D_Fix_AJ	pMDCK_VinCS_Live_ApicalCyto	0.0132
pMDCK_VinCS_Fix_ApicalCyto	pMDCK_VinCS_Fix_AJ	0.2385
pMDCK_VinCSS1033A_Fix_AJ	pMDCK_VinCS_Fix_AJ	0.2643
pMDCK_VinCSS1033A_Fix_ApicalCyto	pMDCK_VinCS_Fix_ApicalCyto	0.2975
pMDCK_VinCSS1033A_Fix_ApicalCyto	pMDCK_VinCS_Live_AJ	0.1499
pMDCK_VinCSS1033D_Fix_FA	pMDCK_VinCS_Fix_AJ	0.8036
pMDCK_VinCS_Live_ApicalCyto	pMDCK_VinCS_Fix_ApicalCyto	0.8678
pMDCK_VinCS_Live_ApicalCyto	pMDCK_VinCS_Live_AJ	0.5196
pMDCK_VinCSS1033A_Fix_ApicalCyto	pMDCK_VinCSS1033A_Fix_AJ	0.8365
pMDCK_VinCSS1033A_Fix_AJ	pMDCK_VinCS_Live_AJ	0.9721

pMDCK_VinCSS1033D_Fix_ApicalCyto	pMDCK_VinCSS1033D_Fix_AJ	0.9994
pMDCK_VinCS_Live_AJ	pMDCK_VinCS_Fix_AJ	0.9999
pMDCK_VinCSS1033A_Fix_AJ	pMDCK_VinCS_Fix_ApicalCyto	1
pMDCK_VinCSS1033A_Fix_ApicalCyto	pMDCK_VinCS_Live_ApicalCyto	1
pMDCK_VinCSS1033D_Fix_FA	pMDCK_VinCS_Live_AJ	1
pMDCK_VinCS_Live_FA	pMDCK_VinCS_Fix_FA	1
pMDCK_VinCSS1033A_Fix_FA	pMDCK_VinCS_Live_FA	0.9999
pMDCK_VinCSS1033A_Fix_AJ	pMDCK_VinCS_Live_ApicalCyto	0.9992
pMDCK_VinCSS1033D_Fix_FA	pMDCK_VinCS_Fix_ApicalCyto	0.9956
pMDCK_VinCSS1033A_Fix_FA	pMDCK_VinCS_Fix_FA	0.9935
pMDCK_VinCS_Live_AJ	pMDCK_VinCS_Fix_ApicalCyto	0.9836
pMDCK_VinCSS1033D_Fix_FA	pMDCK_VinCSS1033A_Fix_AJ	0.819
pMDCK_VinCSS1033D_Fix_FA	pMDCK_VinCS_Live_ApicalCyto	0.3375
pMDCK_VinCSS1033D_Fix_FA	pMDCK_VinCSS1033A_Fix_ApicalCyto	0.0145
pMDCK_VinCSS1033A_Fix_FA	pMDCK_VinCS_Live_AJ	<.0001
pMDCK_VinCS_Live_FA	pMDCK_VinCS_Live_AJ	<.0001
pMDCK_VinCSS1033A_Fix_FA	pMDCK_VinCS_Live_ApicalCyto	<.0001
pMDCK_VinCSS1033D_Fix_FA	pMDCK_VinCSS1033D_Fix_AJ	<.0001
pMDCK_VinCSS1033D_Fix_FA	pMDCK_VinCSS1033D_Fix_ApicalCyto	<.0001
pMDCK_VinCSS1033A_Fix_FA	pMDCK_VinCSS1033A_Fix_AJ	<.0001
pMDCK_VinCSS1033A_Fix_FA	pMDCK_VinCSS1033A_Fix_ApicalCyto	<.0001
pMDCK_VinCS_Live_FA	pMDCK_VinCS_Live_ApicalCyto	<.0001
pMDCK_VinCSS1033A_Fix_FA	pMDCK_VinCS_Fix_AJ	<.0001
pMDCK_VinCS_Live_FA	pMDCK_VinCS_Fix_AJ	<.0001
pMDCK_VinCSS1033A_Fix_FA	pMDCK_VinCS_Fix_ApicalCyto	<.0001
pMDCK_VinCS_Live_FA	pMDCK_VinCS_Fix_ApicalCyto	<.0001
pMDCK_VinCS_Fix_FA	pMDCK_VinCS_Fix_AJ	<.0001
pMDCK_VinCS_Fix_FA	pMDCK_VinCS_Fix_ApicalCyto	<.0001

Table S9. P-values from Tukey's Honest Significant Difference Test for Speed (Velocity Magnitude) in Fig. 3e

Level	- Level	p-Value
MDCK_VinVen_S1033D	MDCK_VinVen_S1033A	<.0001
MDCK_VinVen_S1033D	MDCK_VinVen_WT	<.0001
MDCK_VclKO	MDCK_VinVen_S1033A	0.0034
MDCK_VclKO	MDCK_VinVen_WT	0.0123
MDCK_VinVen_S1033D	MDCK_VclKO	0.1756
MDCK_VinVen_WT	MDCK_VinVen_S1033A	0.9719

Table S10. P-values from Tukey's Honest Significant Difference Test for Correlation Length in Fig. 3f

Level	- Level	p-Value
MDCK_VinVen_S1033D	MDCK_VinVen_S1033A	<.0001
MDCK_VinVen_S1033D	MDCK_VinVen_WT	<.0001
MDCK_VclKO	MDCK_VinVen_S1033A	0.0039
MDCK_VclKO	MDCK_VinVen_WT	0.0055
MDCK_VinVen_S1033D	MDCK_VclKO	0.2336
MDCK_VinVen_WT	MDCK_VinVen_S1033A	0.9995

Extended Methods

Generation of DNA constructs

Construction of pcDNA3.1-TSMod, pcDNA3.1-VinTS, pcDNA3.1-VinV, pcDNA3.1-VinCS, and pcDNA3.1-VinTS-I997A have been described previously (9, 52). PCR mutagenesis was used to generate DNA constructs for the mutant of VinTS that is deficient in Y822 phosphorylation (pcDNA3.1-VinTS-Y822F), mutants of VinV, VinTS, and VinCS that are deficient in S1033 phosphorylation (pcDNA3.1-VinV-S1033A, pcDNA3.1-VinTS-S1033A, and pcDNA3.1-VinCS-S1033A), and mutants of VinV, VinTS, and VinCS that mimic phosphorylated S1033 (pcDNA3.1-VinV-S1033D, pcDNA3.1-VinTS-S1033D, and pcDNA3.1-VinCS-S1033D). For the Y822F mutant, forward primer 5'-TTGGATTCTGGATTCAGGATTCTGGG-3', reverse primer 5'-CCCAGAATCCTGAATCCAGAATCCAA-3', and template DNA pcDNA3.1-VinTS were used. For the S1033A mutants, forward primer 5'- AACCTCATGCAGGCTGTGAAGGAAACT-3', reverse primer 5'- CTGGGCGTTATGAACCAACATCTCAG-3', and template DNA pcDNA3.1-VinV, pcDNA3.1-VinTS, or pcDNA3.1-VinCS were used. For the S1033D mutants, forward primer 5'-AACCTCATGCAGGATGTGAAGGAAACT-3', reverse primer 5'-CTGGGCGTTATGAACCAACATCTCAG-3', and template pcDNA3.1-VinV, DNA pcDNA3.1-VinTS, or pcDNA3.1-VinCS were used. All PCR mutagenesis was conducted using the Q5® Site-Directed Mutagenesis Kit (E0554; New England Biolabs, Ipswich, MA). To create plasmids for lentiviral expression of these constructs, pcDNA3.1 plasmids were digested with NruI/XbaI and ligated into pRRL vector that had been digested with EcoRV/XbaI. All newly generated constructs were verified by DNA sequencing (GENEWIZ from Azenta Life Sciences, Morrisville, NC).

Expression of DNA constructs

HEK293-T cells, used for viral production, were maintained in DMEM-HG (D5796; Sigma Aldrich) supplemented with 10% fetal bovine serum (HyClone) and 1% antibiotic/antimycotic (Gibco). For viral transduction, the second generation viral packaging plasmids psPax2 (Plasmid #12260) and pMD2.G (Plasmid #12259) were purchased from Addgene. To generate viral particles containing the DNA for a desired construct, the corresponding pRRL-based construct, psPax2, and pMD2G plasmids were transfected into HEK293-T cells using Lipofectamine 2000 (Invitrogen) according to the manufacturer's protocol. After 4 hours, the transfection mixture was exchanged for complete growth media. After an additional 72 hours, media containing viral particles was harvested and stored at -80°C. One day prior to viral transduction, MDCK cells were plated in 6-well dishes at a density of approximately 100,000 cells per dish. Cells were transduced with 500 µL of viral particle containing growth media supplemented with 2 µg/mL Polybrene (Sigma Aldrich) to enhance viral uptake. After three passages, transduced cells were sorted via fluorescence activated cell sorting (FACS) based on the intensity of the fluorescent signal of the construct. For expression of FRET sensors in MDCK Parental and MDCK II cells, expression levels were selected that yielded sufficient signal-to-noise in FRET measurements and did not affect cell migration or FA morphology. For rescue of MDCK II Vcl KO cells with VinV constructs, expression levels were selected that localized to FAs, AJs, and cytoplasm as expected.

Droplet-based Migration Assay

To create cell adherent surfaces appropriate for imaging, glass bottom dishes (World Precision Instruments) or no. 1.5 glass coverslips mounted in reusable metal dishes (Bioptechs, Butler, PA) were incubated with 10 µg/ml fibronectin (Fisher Scientific) in PBS at room temperature for 1 hour, rinsed once with PBS, and allowed to dry prior to cell seeding. Following a previously published protocol to create collectively migrating cell islands (56), approximately $5x10^3$ cells suspended in 5 µL growth medium were plated as a droplet on the fibronectin-coated glass bottom cell culture dishes. Cells adhered for 30 minutes at 37°C and 5% CO_2, and then the dish was filled with 2 mL growth medium. Cells were incubated for 72 hours at 37°C and 5% CO_2 to enable formation of a mechanically integrated and collectively migrating cell monolayer. In the droplet assay, all experiments were conducted at 72 hr post-seeding, except for area expansion, which was quantified between 48 and 72 hr post-seeding.

To quantify migration in the droplet assay, cell islands were imaged at 48 and 72hrs using phase microscopy with a 10x objective (UPlan FLN/NA0.3 10x Objective, Olympus) on an Olympus inverted fluorescent microscope (Olympus IX83, Tokyo, Japan) equipped with a sCMOS ORCA-Flash4.0 V2 camera (Hamamatsu Photonics, Hamamatsu, Japan). After establishing Köhler illumination, a fixed grid of images was acquired using MetaMorph Advanced software (Olympus). For each sample, images were stitched together using the ImageJ Grid/Collection stitching plugin. Island size was then manually measured in ImageJ. Briefly, background was subtracted using the Subtract Background tool. The rolling ball radius was set to 75 pixels, and the resultant image was converted to a binary mask using the associated built-in function. To determine the island's expansion over 24hrs, the change in area from 48 to 72hrs was normalized by the initial island size at 48 hrs.

To assess the effect of proliferation in the droplet assay, monolayer expansion was compared in the absence or presence of the proliferation inhibitor Actinomycin D. Immediately following the imaging at 48 hrs post-seeding, cells were treated with Actinomycin D (Sigma, Product SBR00013) at a concentration of 2 ng/mL for a duration of 8 hr. To assess levels of cell proliferation, Click-iT™ Plus EdU Alexa Fluor™ 647 Imaging Kit (Fisher Scientific) was used. At 64 hrs post-seeding, cells were treated with 10μM EdU for 8 hours before fixation. Detection of EdU was performed per the manufacturer's protocol.

Barrier-based Migration Assay

To prepare the surface, 12-well glass bottom plates (Cellvis) were incubated with 10 μg/ml fibronectin (Fisher Scientific) in PBS at room temperature for 1 hour, rinsed once with PBS, and allowed to dry prior to cell seeding. Barrier molds (iBidi) were positioned and adhered to the 12-well glass bottom plate using a custom tool to ensure consistent alignment with respect to the well plate. A 70uL suspension of cells was seeded at a density of 500 cells/μL into one chamber in a barrier mold. Cells grew for approximately 14.5 hours, forming a confluent monolayer inside the barrier. Then, the barrier was lifted, at which point the cells were able to migrate into free space. After barrier removal, cells were washed once and then provided media.

To quantify migration in the barrier assay, timelapse multifield imaging of migration in the barrier assay was performed using phase contrast microscopy on a Zeiss Axio Observer Z1 microscope outfitted with a Pecon XL S1 incubator regulating temperature (37°C), CO_2 concentration (5%), and humidity. The following objective was used: 10x/0.30 Plan-NeoFluar Ph1, (440331-9902) WD: 5.2mm. Movement of the sample (motorized XY stage), image acquisition (Photometrics CoolSNAP HQ2 CCD camera), and software-based autofocus were computer-controlled using MetaMorph Advanced software (Olympus). Imaging was started approximately 3 hours post-barrier lift and conducted for a duration of approximately 6 hours. The delay between two successive images of the same field was 10 minutes. For each monolayer, a minimum of 4 fields of view located along the long free edge of the rectangular monolayer were imaged.

MATLAB (Mathworks) was used for all image analysis. Velocity fields were computed from the timelapse images using a previous implementation of the Optical Flow Constraint method from Vig et al. (57). Velocities were computed on a square grid 32 px (approximately 20.8 μm) apart at all positions inside the monolayer in the field of view. To verify velocity field computation, we simulated the motion of artificial particles subjected to the computed velocity field and overlaid the positions onto the original timelapse movie, as previously described (57). To quantify migration kinematics, speed and spatial correlation length were computed from the velocity fields for each field of view and then averaged to obtain a single value for each monolayer. Speed, s, was defined as the magnitude of the velocity vector averaged over grid points located less than or equal to 500 μm from the leading edge, as given below:

$$s(t) = \frac{1}{N}\sum_{i=1}^{N}\sqrt{\left(v_{x,i}(t)\right)^2 + \left(v_{y,i}(t)\right)^2}, \qquad \forall i: dist\left(\vec{r_i}, L(t,x,y)\right) \in [0{,}500]\ \mu\text{m}$$

where $\vec{r_i} = \langle x_i, y_i \rangle$ is the position of grid point i, $\vec{v_i}(t) = \langle v_{x,i}(t), v_{y,i}(t) \rangle$ is the velocity of grid point i at timepoint t, $L(t,x,y)$ is the curve representing the leading edge at timepoint t, and

$dist\left(\vec{r_i}, L(t,x,y)\right)$ is the minimum distance between the grid position $\vec{r_i}$ and the leading edge curve $L(t,x,y)$. The fixed coordinate system is defined such that the y-direction is normal to the free edge created by the barrier mold, and the x-direction is parallel to it. For each field of view, a time-averaged speed was then obtained, and the fields of view were averaged to obtain a single value for each monolayer. Furthermore, as a measure of spatial correlation in the velocity field, we used the correlation length for lateral velocity deviations, as previously described (25). The lateral velocity deviation for grid point i at timepoint t, $u_i(t)$, is defined as the x component of the velocity at the grid location minus the average of x velocity components over all grid locations in the monolayer in the field of view, given by: $u_i(t) = v_{x,i}(t) - \langle v_x(t) \rangle$. The normalized spatial correlation coefficient as a function of radial distance r at time t, $C(r,t)$, was then computed using the following equation:

$$C(r,t) = \frac{\langle u_i(t) \cdot u_j(t) \rangle}{\sqrt{\langle u_i(t)^2 \rangle \cdot \langle u_j(t)^2 \rangle}},$$
$$\forall i,j : r - \frac{\Delta r}{2} \leq \left\| \vec{r_i} - \vec{r_j} \right\| < r + \frac{\Delta r}{2} \;\; and \; dist\left(\vec{r_i}, L_t(x,y)\right) \in [0{,}500] \text{ μm}$$

Computation was performed over all grid points i located less than or equal to 500 μm from the leading edge, which includes most of the monolayer but keeps a constant computation window for all fields of view. Grid points were binned on radial distance using a bin size Δr of 10 μm. For each field of view, a single correlation length was determined by plotting the time-averaged normalized correlation coefficient, $C(r) = \langle C(r,t) \rangle$, versus radial distance r and determining the smallest value for r such that the correlation function decays below a threshold of 0.1. To assess relationships between speed and correlation length, the root-mean-square lateral velocity deviation and correlation length in lateral velocity deviation from individual timepoints were used.

Western Blot Analysis

Cells were washed once in ice-cold PBS buffer and lysed in ice-cold lysis buffer [10% Glycerol, 2 mM EDTA, 250 mM NaCl, 50mM HEPES, 0.5% NP-40, protease inhibitor cocktail (Sigma)]. Cell lysates were centrifuged for 10 minutes at 13000 RPM and 4°C. Supernatants were separated and pellets of cell debris were discarded. Afterwards, 2x Laemmli sample buffer (Bio-Rad Laboratories) was added to the lysate for a 1:1 dilution and the sample was boiled at 100 °C for 5 minutes. Samples were then loaded into Mini-PROTEAN® TGX™ Precast Gels (4-20%, Biorad) and ran at 100 V for 70 minutes before being transferred to a PVDF membrane (Bio-Rad Laboratories) via wet-transfer. Membranes were blocked with 5% dry milk in TBST [10 mM Tris-HCl, 100 mM NaCl, 0.1% Tween 20] for 1 hour at room temperature and then incubated with primary antibodies per the dilution listed in Table S11 overnight at 4 °C. Afterwards, the membrane was rinsed 3 times in TBST and incubated with the appropriate enzyme conjugated secondary antibody (Life Technologies), depending on the animal species, for 1 hour at room temperature. Membranes were then rinsed again 3 times in TBST and then developed using Supersignal West Pico Chemiluminescent Substrate (Thermo Fisher Scientific). The signal was detected either on X-ray film (Kodak) or by imaging (ChemiDoc Imaging System, Bio-Rad Laboratories). Primary and secondary antibodies used for Western Blots are provided in Table S11.

Table S11. Primary and Secondary Antibodies for Western Blot Analysis.

Type	Antibody	Species	Clonality	Manufacturer	Product	Dilution
Primary	Vinculin	Mouse	monoclonal	Sigma	V91314	1:8000
Primary	GAPDH	Rabbit	polyclonal	Santa Cruz	sc25778	1:4000
Primary	GFP	Rabbit	polyclonal	Abcam	ab6556	1:5000
Secondary	Anti-mouse IgG (H+L), Cross-Adsorbed Secondary Antibody, HRP	Goat	polyclonal	Thermo Fisher	G21040	1:3000 to 1:5000
Secondary	Anti-rabbit IgG (H+L) , Cross-Adsorbed Secondary Antibody, HRP	Goat	polyclonal	Thermo Fisher	G21234	1:3000 to 1:5000

Fixation & Immunofluorescent Staining

For fixation or immunofluorescent labeling, cells were washed once with PBS (containing Ca^{2+} and Mg^{2+}), fixed with 4% methanol-free (EM grade) paraformaldehyde (Electron Microscopy Sciences, Hatfield, PA) for 10 minutes and then rinsed with PBS. For immunofluorescent labeling, cells were treated with 0.1% Triton-X for 15 min and then rinsed with PBS. Fresh 2% bovine serum albumin (BSA, Sigma Aldrich) in PBS was used as blocking buffer for 30 min. Primary antibody was applied for 60 min and then rinsed three times with PBS. Cells were again blocked for 30 min. Secondary antibody was applied for 60 min. Cells were then rinsed three times with PBS and imaged in PBS. Primary antibodies and the dilutions used for immunofluorescent labeling are provided in Table S12. Secondary antibodies raised against the appropriate primary species and conjugated with dyes, including Alexa Fluor 488, 594, and 647, were purchased from Thermo Fisher and used at a dilution of 1:500. To label actin, cells were treated with Alexa Fluor 488-, 594-, or 647-conjugated phalloidin (Invitrogen) at a 1:100 dilution during the secondary antibody step.

Table S12. Primary Antibodies for Immunofluorescent Staining.

Antibody	Species	Clonality	Manufacturer	Product	Dilution
vinculin	Mouse	monoclonal	Sigma	V91314	1:500
E-cadherin	Rat	monoclonal	Sigma	U3254	1:500
α -catenin	Rabbit	polyclonal	Cell Signaling	3236	1:200
α-catenin extended conformation-sensitive antibody (α18)	Rat	monoclonal	Nagafuchi Lab*	N/A	1:1000

Table Notes: *Generous gift of Dr. Akira Nagafuchi (Nara Medical University)

Imaging of FRET-based Sensors and Immunofluorescence

An Olympus inverted fluorescent microscope (Olympus IX83, Tokyo, Japan) was used to image samples. Images were acquired at 60x magnification (UPlanSApo 60X/NA1.35 Objective, Olympus) and illuminated by a Lambda LS equipped with a 300W ozone-free xenon bulb (Sutter Instrument, Novato, CA). The images were captured using a sCMOS ORCA-Flash4.0 V2 camera (Hamamatsu Photonics, Hamamatsu, Japan). The FRET images were acquired using a custom filter set comprised of an mTFP1 excitation filter (ET450/30x; Chroma Technology Corp, Bellows Falls, VT), mTFP1 emission filter (FF02-485/20-25, Semrock, Rochester, NY), Venus excitation filter (ET514/10x; Chroma Technology Corp), Venus emission filter (FF01-571/72; Semrock) and

dichroic mirror (T450/514rpc; Chroma Technology Corp). For sensitized emission FRET microscopy, three images were acquired to calculate FRET efficiency (58). These include imaging the acceptor (Venus excitation, Venus emission), FRET (mTFP1 excitation, Venus emission), and donor (mTFP1 excitation, mTFP1 emission). Exposure times for imaging of Venus, Teal-Venus FRET, and Teal were 1000ms, 1500ms, and 1500ms, respectively. To avoid photobleaching, only one image was taken per cellular region, either at the basal (for FAs) or apical (for AJs) focal plane. For immunofluorescent imaging, we utilized the DA/FI/TR/Cy5-4X4 M-C Brightline Sedat filter set (Semrock) and the associated dichroic mirror (FF410/504/582/669-Di01). The motorized filter wheels (Lambda 10-3; Sutter Instrument), automated stage (H117EIX3; Prior Scientific, Rockland, MA), and image acquisition were controlled through MetaMorph Advanced software (Olympus). For live cell imaging, growth media was replaced with live cell visualization media (Sapphire North America, Ann Arbor, MI, MC102), supplemented with 10% FBS and 1 g/L sodium bicarbonate, 30 minutes before imaging. A constant temperature was maintained across the sample using an objective heater (Bioptechs, Butler, PA 150819-13) in conjunction with a stage and lid heater (Bioptechs Stable Z System 403-1926). A humidified CO_2 perfusion system (Bioptechs 130708) was used to maintain a stable pH. All components were brought to equilibrium prior to imaging.

Calculation of FRET Efficiency from Sensitized Emission

FRET was detected through measurement of sensitized emission (59) and calculated using custom written code in MATLAB (Mathworks) (58). All analyses were conducted on a pixel-by-pixel basis. Prior to FRET calculations, all images were first corrected for dark current, uneven illumination, background intensity, and three-dimensional offsets caused by chromatic aberrations and minute hardware misalignments (registration) as previously described (60). Spectral bleed-through coefficients were determined through FRET-imaging of cells expressing only donor fluorescent protein (FP) or only acceptor FP. The donor bleed-through coefficient (dbt) was calculated for mTFP1 as:

$$dbt = \langle \frac{I_{DA}}{I_{DD}} \rangle$$

where I_{DA} is the intensity in the FRET-channel, I_{DD} is the intensity in the donor-channel, and data were binned by donor-channel intensity. Similarly, the acceptor bleed-through coefficient (abt) was calculated for Venus(A206K) as:

$$abt = \langle \frac{I_{DA}}{I_{AA}} \rangle$$

where I_{AA} is the intensity in the acceptor-channel, and data were binned by acceptor-channel intensity. For the mTFP1-Venus(A206K) FP pair on our microscope setup, the cross-talk between donor and acceptor channels (signal from donor in acceptor channel and vice-versa) was determined to be negligeable. To correct for spectral bleed-through, pixel-by-pixel FRET corrections were performed according to the equation:

$$F_c = I_{DA} - dbt \cdot I_{DD} - abt \cdot I_{AA}$$

where F_c is the corrected FRET intensity, I_{DA} is the intensity in the FRET-channel, I_{DD} is the intensity in the donor-channel, and I_{AA} is the intensity in the acceptor-channel. After bleed-through correction, FRET efficiency was calculated. Through imaging donor-acceptor fusion constructs of differing, but constant, FRET efficiencies, it is possible to calculate two proportionality constants that enable the calculation of FRET efficiencies for any single-chain biosensor (59). These proportionality constants are G:

$$G = -\frac{\Delta\left(\frac{F_c}{I_{AA}}\right)}{\Delta\left(\frac{I_{DD}}{I_{AA}}\right)}$$

where Δ indicates the change between two donor-acceptor fusion proteins, and k:

$$k = \frac{I_{DD} + \frac{F_c}{G}}{I_{AA}}$$

Using published methods (60), these calibration factors were experimentally determined for mTFP1 and Venus(A206K). With these two proportionality constants, it is possible to calculate both FRET efficiency (E):

$$E = \frac{\frac{F_c}{G}}{I_{DD} + \frac{F_c}{G}}$$

and the relative concentration of donor and acceptor fluorescent proteins $[D]/[A]$ (or DPA) in a sample:

$$\frac{[D]}{[A]} = \frac{I_{DD} + \frac{F_c}{G}}{k \cdot I_{AA}}$$

The calibration constants G and k were monitored over the course of this work to control for changes in lamp and filter performance.

Segmentation and masking routines were used to quantitate FRET efficiencies within FAs (for images of the basal focal plane) or AJs and cytoplasm (for images of the apical focal plane). All operations were conducted on the acceptor channel, which is independent of FRET and proportional to the concentration of VinTS, or VinCS. Segmentation of FAs was done as previously reported using a water-based algorithm (61). For AJ segmentation, edge detection on the acceptor image was conducted using a dispersive phase stretch transform (62). The resultant edge detection was then high-pass filtered and a user-defined intensity threshold was used to eliminate background signal and isolate the AJs. For basal and apical images, binary masks containing all FAs or all AJs, respectively, were applied to FRET efficiency images. Cytoplasmic signal was examined in all apical images by inverting the AJ mask and removing nuclear regions from the cytoplasmic mask via local normalization followed by morphological processing. After automated masking of sub-cellular compartments, closed boundaries were manually drawn by the user based on the unmasked acceptor channel image to include regions in the monolayer with appropriate and uniform expression of the sensor. Information outside manual boundaries was discarded. For each image, mean acceptor intensity, FRET efficiency, and donor-per-acceptor ratio were characterized.

To ensure the quality of FRET data, a multi-scale filtering approach was used. In comparing samples, the same filtering approach was applied to each population of data points. First, at the pixel level, regions detected as having DPA outside of the 0.5-2.0 range, were discarded. Then, at the image level, images with less than 2000 px in the analysis region were discarded. Additionally, images were discarded if >33% of the pixels were removed for out-of-bounds DPA. Overall, the pixel-level filtering process removed less than 5% of pixels on average, and the image-level filtering process removed less than 5% of images.

Quantification of Actin Organization at the Edge of Migrating Monolayers

Actin organization was assessed using phalloidin labeling of actin (see Fixation & Immunofluorescent Staining) in the droplet assay 72 hr post-seeding. Lamellipodia and actin belts (of continuous contour length greater than 75μm) were identified manually.

Quantification of Abundance of Proteins at AJs in Migrating Monolayers

The abundance of proteins at the AJ were assessed using immunofluorescent labeling (see Fixation & Immunofluorescent Staining) in the droplet assay 72 hr post-seeding. As with FRET imaging, all images were corrected for dark current, uneven illumination, background intensity, and three-dimensional offsets caused by chromatic aberrations and minute hardware misalignments (registration). Then, binary masks of the AJs were generated via high-pass filtering of the immunofluorescent channel using custom MATLAB code and applied to images to obtain average intensities for each image. To account for day-to-day variability in immunofluorescent staining, the immunofluorescent signals were each normalized by day.

Quantitation of Vinculin FA Morphology

To quantify vinculin focal adhesion (FA) morphology, images of immunofluorescent-labeled vinculin or the accepter channel of VinV, VinTS, or VinCS were used. Focal adhesion segmentation was performed as described above using the signal of immunofluorescent-labeled vinculin or the acceptor channel of VinV, VinTS, or VinCS. For each FA, the distance from its center to the nearest point on a manually drawn leading edge was determined. The orientation of the FA was defined as the angle between the major axis of the ellipse fit to the FA and the normal direction of the leading edge at the nearest point to the FA. Therefore, 0° indicates the FA is parallel to the migration direction, and 90° indicates the FA is perpendicular to the migration direction. FAs were binned on distance from leading edge, and FA area and orientation were plotted as functions of distance from leading edge.

Estimation of VinCS Closed FRET Efficiency and Normalization of VinCS FRET Data

To obtain a reference value for the fully closed FRET Eff of VinCS, VinCS-expressing MDCK Parental cells were sparsely seeded on poly-L-Lysine coated surfaces, where they non-specifically adhered, as done previously (9). In detail, glass bottom dishes were coated with Poly-L-Lysine (Sigma P4832-50ML) using the Millipore Sigma Poly-L-Lysine Cell Attachment Protocol. MDCK Parental cells expressing VinCS were sparsely seeded on the poly-L-Lysine coated dishes with media, allowed to adhere for 30 minutes, and then immediately imaged live or fixed and imaged. FRET efficiency was analyzed on a cell basis, using a manual cell mask and minimum acceptor intensity threshold, identical to the analysis approach for VinCS in the cytoplasm of MDCK monolayers. Cells that were highly spread, as determined by bright field images, or possessed cell-substrate adhesions, as determined by VinCS localization, were excluded. The mean FRET efficiency for VinCS on poly-L-Lysine in the live and fixed conditions were used to normalize the FRET efficiency values for VinCS in cell monolayers in the live and fixed conditions, respectively.

Confocal Imaging and FRET Analysis

For confocal imaging, samples were imaged with an Andor XD Revolution Spinning Disk Confocal, which consists of an Olympus IX81 inverted microscope equipped with a Yokogawa CsuX-1 spinning disk (5000rpm) controlled with MetaMorph Advanced software (Olympus). This microscope is maintained by the Duke Light Microscope Core Facility. Images were acquired at 100x magnification (UPlanSApo 100X/NA1.4 Objective, Olympus) using an Andor EMCCD Camera (Ixon3 897 512 EMCCD). The FRET images were acquired using a filter set comprised of a mTFP1 emission filter (483/32), Venus emission filter (542/27) and dichroic mirror (CYR; 445/515/561). For FRET microscopy, three images were acquired. These images included the acceptor (515nm 50mW diode excitation, Venus emission), FRET (445nm 40mW diode excitation, Venus emission), and donor (445nm 40mW diode excitation, mTFP1 emission). Images were acquired without gain and a 75% laser power. Exposure times for Venus, FRET, and Teal were 1000ms, 1500ms, and 1500ms, respectively. Images were post-processed to correct for dark current and aligned using a custom MATLAB script. Ratiometric FRET images were determined by dividing the FRET image by its respective mTFP1 image. Segmentation of cells and adhesions was conducted on the acceptor channel using a custom MATLAB script and user-defined masking.

Stimulated Emission Depletion Microscopy (STED) Imaging of Actin

Cells were fixed, permeabilized and blocked as described previously. For STED imaging, cells were labeled with Alexa Fluor 488 phalloidin (Invitrogen) at a concentration of 1:25. Following immunofluorescent staining, PBS was removed from the sample, and ProLong™ Diamond Antifade Mountant (Invitrogen, P36965) was applied per manufacturer's instructions. Mountant set for 24 hrs before imaging. Samples were imaged using a Leica STED Confocal, which consists of an inverted Leica DMi8 Platform with motorized scanning stage and controlled by LAS X. Images were acquired at 93x (HC PL APO 93X/1.30 GLYC motCORR, Leica). Alexa Fluor 488 was excited with a tunable white light laser and simultaneously depleted with a 660nm laser. Sample emission was collected using a high-sensitivity, gated GaAsP HyD detector. Hyugens deconvolution, linked to Leica's LAS X software, was implemented to deconvolve image stacks.

SI References

1. R. Alert, X. Trepat, Physical Models of Collective Cell Migration. *Annual Review of Condensed Matter Physics* **11**, 77-101 (2020).
2. C. De Pascalis, S. Etienne-Manneville, Single and collective cell migration: the mechanics of adhesions. *Mol Biol Cell* **28**, 1833-1846 (2017).
3. B. Ladoux, R. M. Mege, Mechanobiology of collective cell behaviours. *Nat Rev Mol Cell Biol* **18**, 743-757 (2017).
4. C. Schreiber, B. Amiri, J. C. J. Heyn, J. O. Radler, M. Falcke, On the adhesion-velocity relation and length adaptation of motile cells on stepped fibronectin lanes. *Proc Natl Acad Sci U S A* **118** (2021).
5. S. Garcia *et al.*, Physics of active jamming during collective cellular motion in a monolayer. *Proc Natl Acad Sci U S A* **112**, 15314-15319 (2015).
6. K. Vazquez, A. Saraswathibhatla, J. Notbohm, Effect of substrate stiffness on friction in collective cell migration. *Sci Rep* **12**, 2474 (2022).
7. P. Sens, Rigidity sensing by stochastic sliding friction. *Europhysics Letters* **104**, 38003 (2013).
8. M. K. L. Han, J. de Rooij, Converging and Unique Mechanisms of Mechanotransduction at Adhesion Sites. *Trends Cell Biol* **26**, 612-623 (2016).
9. C. Grashoff *et al.*, Measuring mechanical tension across vinculin reveals regulation of focal adhesion dynamics. *Nature* **466**, 263-266 (2010).
10. B. D. Hoffman, C. Grashoff, M. A. Schwartz, Dynamic molecular processes mediate cellular mechanotransduction. *Nature* **475**, 316-323 (2011).
11. B. D. Hoffman, A. S. Yap, Towards a Dynamic Understanding of Cadherin-Based Mechanobiology. *Trends Cell Biol* **25**, 803-814 (2015).
12. Q. le Duc *et al.*, Vinculin potentiates E-cadherin mechanosensing and is recruited to actin-anchored sites within adherens junctions in a myosin II-dependent manner. *J Cell Biol* **189**, 1107-1115 (2010).
13. D. E. Leckband, J. d. Rooij, Cadherin Adhesion and Mechanotransduction. *Annual Review of Cell and Developmental Biology* **30**, 291-315 (2014).
14. J. M. Leerberg *et al.*, Tension-sensitive actin assembly supports contractility at the epithelial zonula adherens. *Curr Biol* **24**, 1689-1699 (2014).
15. G. F. Weber, M. A. Bjerke, D. W. DeSimone, A mechanoresponsive cadherin-keratin complex directs polarized protrusive behavior and collective cell migration. *Dev Cell* **22**, 104-115 (2012).
16. D. L. Huang, N. A. Bax, C. D. Buckley, W. I. Weis, A. R. Dunn, Vinculin forms a directionally asymmetric catch bond with F-actin. *Science* **357**, 703-706 (2017).
17. F. Kong, A. J. Garcia, A. P. Mould, M. J. Humphries, C. Zhu, Demonstration of catch bonds between an integrin and its ligand. *J Cell Biol* **185**, 1275-1284 (2009).
18. A. Elosegui-Artola *et al.*, Mechanical regulation of a molecular clutch defines force transmission and transduction in response to matrix rigidity. *Nat Cell Biol* **18**, 540-548 (2016).
19. L. M. Owen, N. A. Bax, W. I. Weis, A. R. Dunn, The C-terminal actin-binding domain of talin forms an asymmetric catch bond with F-actin. *Proc Natl Acad Sci U S A* **119**, e2109329119 (2022).
20. S. Rakshit, Y. Zhang, K. Manibog, O. Shafraz, S. Sivasankar, Ideal, catch, and slip bonds in cadherin adhesion. *Proc Natl Acad Sci U S A* **109**, 18815-18820 (2012).
21. C. D. Buckley *et al.*, Cell adhesion. The minimal cadherin-catenin complex binds to actin filaments under force. *Science* **346**, 1254211 (2014).
22. B. L. Bangasser, S. S. Rosenfeld, D. J. Odde, Determinants of maximal force transmission in a motor-clutch model of cell traction in a compliant microenvironment. *Biophys J* **105**, 581-592 (2013).
23. C. E. Chan, D. J. Odde, Traction dynamics of filopodia on compliant substrates. *Science* **322**, 1687-1691 (2008).
24. A. Elosegui-Artola *et al.*, Rigidity sensing and adaptation through regulation of integrin types. *Nat Mater* **13**, 631-637 (2014).

25. L. Petitjean *et al.*, Velocity fields in a collectively migrating epithelium. *Biophys J* **98**, 1790-1800 (2010).
26. P. Roca-Cusachs, T. Iskratsch, M. P. Sheetz, Finding the weakest link: exploring integrin-mediated mechanical molecular pathways. *J Cell Sci* **125**, 3025-3038 (2012).
27. T. F. Bartsch *et al.*, Elasticity of individual protocadherin 15 molecules implicates tip links as the gating springs for hearing. *Proc Natl Acad Sci U S A* **116**, 11048-11056 (2019).
28. R. Changede, M. Sheetz, Integrin and cadherin clusters: A robust way to organize adhesions for cell mechanics. *Bioessays* **39**, 1-12 (2017).
29. Y. Wu, P. Kanchanawong, R. Zaidel-Bar, Actin-delimited adhesion-independent clustering of E-cadherin forms the nanoscale building blocks of adherens junctions. *Dev Cell* **32**, 139-154 (2015).
30. B. Cheng *et al.*, An Integrated Stochastic Model of Matrix-Stiffness-Dependent Filopodial Dynamics. *Biophys J* **111**, 2051-2061 (2016).
31. A. R. Harris *et al.*, Characterizing the mechanics of cultured cell monolayers. *Proc Natl Acad Sci U S A* **109**, 16449-16454 (2012).
32. K. D. Schulze *et al.*, Elastic modulus and hydraulic permeability of MDCK monolayers. *J Biomech* **53**, 210-213 (2017).
33. S. Le, M. Yu, J. Yan, Direct single-molecule quantification reveals unexpectedly high mechanical stability of vinculin-talin/alpha-catenin linkages. *Sci Adv* **5**, eaav2720 (2019).
34. D. Haussinger *et al.*, Proteolytic E-cadherin activation followed by solution NMR and X-ray crystallography. *EMBO J* **23**, 1699-1708 (2004).
35. S. J. Franco *et al.*, Calpain-mediated proteolysis of talin regulates adhesion dynamics. *Nat Cell Biol* **6**, 977-983 (2004).
36. P. Ringer *et al.*, Multiplexing molecular tension sensors reveals piconewton force gradient across talin-1. *Nat Methods* **14**, 1090-1096 (2017).
37. T. P. Teravainen *et al.*, alphaV-integrins are required for mechanotransduction in MDCK epithelial cells. *PLoS One* **8**, e71485 (2013).
38. Y. V. Pereverzev, O. V. Prezhdo, M. Forero, E. V. Sokurenko, W. E. Thomas, The two-pathway model for the catch-slip transition in biological adhesion. *Biophys J* **89**, 1446-1454 (2005).
39. S. Pokutta, H. J. Choi, G. Ahlsen, S. D. Hansen, W. I. Weis, Structural and thermodynamic characterization of cadherin.beta-catenin.alpha-catenin complex formation. *J Biol Chem* **289**, 13589-13601 (2014).
40. S. D. Hansen *et al.*, alphaE-catenin actin-binding domain alters actin filament conformation and regulates binding of nucleation and disassembly factors. *Mol Biol Cell* **24**, 3710-3720 (2013).
41. O. J. Harrison *et al.*, Two-step adhesive binding by classical cadherins. *Nat Struct Mol Biol* **17**, 348-357 (2010).
42. S. Le, M. Yu, J. Yan, Phosphorylation Reduces the Mechanical Stability of the alpha-Catenin/ beta-Catenin Complex. *Angew Chem Int Ed Engl* **58**, 18663-18669 (2019).
43. O. K. Dudko, G. Hummer, A. Szabo, Intrinsic rates and activation free energies from single-molecule pulling experiments. *Phys Rev Lett* **96**, 108101 (2006).
44. J. L. Bays, K. A. DeMali, Vinculin in cell-cell and cell-matrix adhesions. *Cell Mol Life Sci* **74**, 2999-3009 (2017).
45. L. B. Case *et al.*, Molecular mechanism of vinculin activation and nanoscale spatial organization in focal adhesions. *Nat Cell Biol* **17**, 880-892 (2015).
46. C. Bertocchi *et al.*, Nanoscale architecture of cadherin-based cell adhesions. *Nat Cell Biol* **19**, 28-37 (2017).
47. D. T. Gillespie, Exact stochastic simulation of coupled chemical reactions. *The Journal of Physical Chemistry* **81**, 2340-2361 (1977).
48. M. Ghibaudo *et al.*, Traction forces and rigidity sensing regulate cell functions. *Soft Matter* **4**, 1836-1843 (2008).
49. D. W. Dumbauld *et al.*, How vinculin regulates force transmission. *Proc Natl Acad Sci U S A* **110**, 9788-9793 (2013).
50. C. Malinverno *et al.*, Endocytic reawakening of motility in jammed epithelia. *Nat Mater* **16**, 587-596 (2017).

51. X. Peng, L. E. Cuff, C. D. Lawton, K. A. DeMali, Vinculin regulates cell-surface E-cadherin expression by binding to beta-catenin. *J Cell Sci* **123**, 567-577 (2010).
52. K. E. Rothenberg, D. W. Scott, N. Christoforou, B. D. Hoffman, Vinculin Force-Sensitive Dynamics at Focal Adhesions Enable Effective Directed Cell Migration. *Biophys J* **114**, 1680-1694 (2018).
53. A. Braeutigam, A. N. Simsek, G. Gompper, B. Sabass, Generic self-stabilization mechanism for biomolecular adhesions under load. *Nat Commun* **13**, 2197 (2022).
54. A. Carisey *et al.*, Vinculin regulates the recruitment and release of core focal adhesion proteins in a force-dependent manner. *Curr Biol* **23**, 271-281 (2013).
55. R. Koirala *et al.*, Inside-out regulation of E-cadherin conformation and adhesion. *Proc Natl Acad Sci U S A* **118** (2021).
56. X. Trepat *et al.*, Physical forces during collective cell migration. *Nat Phys* **5**, 426-430 (2009).
57. D. K. Vig, A. E. Hamby, C. W. Wolgemuth, On the Quantification of Cellular Velocity Fields. *Biophys J* **110**, 1469-1475 (2016).
58. A. S. LaCroix, K. E. Rothenberg, M. E. Berginski, A. N. Urs, B. D. Hoffman, Construction, imaging, and analysis of FRET-based tension sensors in living cells. *Methods Cell Biol* **125**, 161-186 (2015).
59. H. Chen, H. L. Puhl, S. V. Koushik, S. S. Vogel, S. R. Ikeda, Measurement of FRET efficiency and ratio of donor to acceptor concentration in living cells. *Biophysical Journal* **91**, L39-L41 (2006).
60. E. M. Gates, A. S. LaCroix, K. E. Rothenberg, B. D. Hoffman, Improving Quality, Reproducibility, and Usability of FRET-Based Tension Sensors. *Cytometry A* **95**, 201-213 (2019).
61. K. E. Rothenberg, S. S. Neibart, A. S. LaCroix, B. D. Hoffman, Controlling Cell Geometry Affects the Spatial Distribution of Load Across Vinculin. *Cell Mol Bioeng* **8**, 364-382 (2015).
62. M. H. Asghari, B. Jalali, Edge detection in digital images using dispersive phase stretch transform. *Int J Biomed Imaging* **2015**, 687819 (2015).